Table of Contents

List of Tables

List of Figures

1 Introduction

1.1 Historical Background

The existence of neutrinos was postulated in 1931 by W. Pauli to preserve the law of energy conservation in nuclear β-decays[1]. Its name literally means "little neutral one" in Italian and was first introduced by E. Fermi.

Neutrinos are the most elusive of all known elementary particles. This is due to their lack of an electric charge and the fact that neutrinos interact with matter only through the weak interactions. This latter fact prompted Pauli himself to consider the neutrino a "particle whose existence cannot be proven".

However, the introduction of uranium fission reactors provided experimentalists with an abundant source of neutrinos, and in 1956 Reines and Cowan demonstrated the existence of neutrinos by observing inverse beta decays[2].

Only 6 years later Danby et al. confirmed the existence of a second type of neutrino[3], associated with muons rather than electrons. After a brief period in which the newly found particle was known as "neutretto"[4], the two types of neutrinos were named electron and muon neutrino (ν_e and ν_μ).

In 1975 a third lepton – the τ - was discovered at the Stanford Linear Accelerator Center[5]. Analogous to the electron and the muon it too was expected to have a neutral partner, the tau neutrino (ν_τ). Subsequent experiments found the multibody decay topology of the tau lepton to be consistent with the emission of a neutrino[6]. The direct observation of the inverse reaction with an incoming neutrino producing a tau lepton in a charged-current reaction proved to be a lengthy process. In the following years limits were set on the ν_τ production and interaction rate in beam dump experiments[7] and the coupling of tau leptons to ν_e and ν_μ[8].

The first direct observation of tau neutrino charged-current interactions was announced by the Fermilab E872 collaboration in July 2000[9]. The experiment used an 800 GeV proton beam from the Tevatron accelerator at Fermi National Accelerator laboratory (Fermilab) impinging on a tungsten block to produce a beam containing a

significant fraction of tau neutrinos. An emulsion detector recorded charged particles produced in neutrino-nucleon interactions. In the analysis, event topologies were reconstructed to identify likely ν_τ CC events.

1.2 The Purpose of this Thesis

The purpose of this thesis is to provide a normalization for the four tau neutrino interactions observed in experiment E872 at Fermilab. There are two ways to calculate the expected ν_τ interaction yield, a first-principle calculation and normalization against other types of neutrino events.

In using the first approach, one encounters a variety of unknown parameters, including production cross sections and branching ratios for charmed particles as well as event location efficiencies. It is therefore generally preferable to use the second method, because many uncertainties will cancel out. The downside to this is that only a limited number of events are available, leading to the introduction of a sizable statistical error. Also, careful consideration must be given to any background effects appearing in one component of the neutrino beam, but not in the others.

In E872, tau neutrinos originate almost exclusively in decays of charmed mesons D_s and subsequent decays of tau leptons. The total number of events from charm therefore provides a basis from which the expected number of observable tau charged-current interactions can be calculated.

In this thesis, electron and muon neutrino charged-current events are analyzed to obtain an estimate for the total number of events from charm decays. Particular attention is given to the calculation of the fraction of muon neutrinos from light meson decay, by far the dominant background (non-charm) component in the beam. The result, corrected for efficiencies, is used to set constraints on the standard nature of tau neutrinos.

1.3 Analysis Steps

The analysis procedure can be broken down into several individual steps. These are:

- Reduction of the raw data acquired during the run. This was accomplished by using a combination of computerized stripping and eye-scanning of electronic data.

- Emulsion analysis, done at Nagoya University. The event sample was subjected to background cuts and scanned with an automated system. Primary vertices and daughter tracks were identified for a limited number of events.

- For the purpose of this thesis, muon events were identified in the electronic sample. Using downstream drift chamber, muon-ID system and vertex position information, tracks were reconstructed and their momenta were calculated.

- The identified muon sample momenta were fit to theoretically calculated distributions in order to directly identify the amount of non-charm background.

- Another fit was done to the energy spectrum in the electromagnetic calorimeter. In this case, only events with vertices located in the emulsion were used. The result from the muon momentum fit was used as a constraint.

- Knowing the amount of neutrino interactions from charm, the expected event yield for tau neutrino charged-current interactions was calculated and compared to the experimental result.

1.4 Overview of Subsequent Chapters

The following gives an overview of chapters of this thesis.

- Chapter 2 gives a brief introduction of the theory of particle physics, in particular of neutrino physics. Possible extensions to the Standard Model, as far as they are relevant to the issue at hand, are briefly discussed.

- Chapter 3 describes the experimental setup in Fermilab E872. The systems used for work contained in this thesis, most notably the spectrometer and the calorimeter, are described in more detail.

- Chapter 4 deals with the event selection process. The general analysis process, leading to the identification of the actual tau event candidates, is described first. The last subsection shows in greater detail the procedure for the muon charged current event selection, done specifically for this thesis.

- Chapter 5 details the phenomenology particular to this experiment and the numerical simulations that were used in the analysis.

- Chapter 6 contains the calculation of the beam composition and the final result for the tau neutrino charged current cross section. Also described is the relevance of the result for non-standard physics effects.

- Chapter 7 is a brief summary of the work done and the results obtained in this thesis.

- The appendices contain a more detailed treatment of issues that would otherwise have been beyond the framework of this thesis. These are:
  - The measurement error on the muon momentum.
  - A discussion of background sources for muons other than light meson decays.
  - Theory and experimental results for neutrino oscillations in greater detail.
  - An overview of the four tau event candidates.

2 Theory and Phenomenology

2.1 Introduction

The following is an overview of the physics relevant to the observation of tau neutrino interactions. Section 2.2 contains the conventional physics that has a well-established experimental foundation. This model also predicts a definite cross-section for interactions of tau neutrinos with matter. In section 2.3 several possible extensions of the generally accepted "Standard Model" are discussed, and the effect they could have on the result of the experiment. Those extensions include neutrino masses, neutrino oscillations, the possibility of a sterile neutrino and decay of a massive tau neutrino.

2.2 The Standard Model

2.2.1 Particles

The Standard Model represents the theoretical basis of modern particle physics. Though many theories go beyond this "Standard Model", they have no additional experimental justification.

All fundamental constituents of matter have a quantity associated with them that behaves like an intrinsic angular momentum. This quantity, the "spin", can take on values of

$$s = n\frac{\hbar}{2}, n = 0,1,2...$$ (2.1)

According to the exclusion principle first proposed by W. Pauli in 1925[10], particles with even n can be in identical quantum states while those with odd n cannot. Using this fact, Fermi and Dirac developed a statistical theory for the latter, while Einstein and Bose developed a theory for the former particles[11]. For this reason they became known as *Fermions* and *Bosons*.

In 1931, Dirac realized that all particles should have a counterpart – an antiparticle - with equal properties but opposite charge[12]. This prediction, confirmed for the electron only one year later[13], turned out to be a general principle of physics.

In the following decades a host of new particles was discovered. A first attempt to categorize them led to their classification as leptons (electrons, muons and their neutrinos) and hadrons (everything else)[14]. This distinction reflected the fact that only the second group interacted by way of the strong nuclear interaction.

The large number and variety of hadrons suggested an underlying fundamental principle. In 1964 Gell-Mann[15] and Zweig[16] independently proposed a model according to which all hadrons could be described by one of two combinations of three-dimensional representations of the SU(3) group. These were:

$$3 \otimes \overline{3} = 8 \oplus 1 \text{ (mesons)}$$

and

$$3 \otimes 3 \otimes 3 = 10 \oplus 8 \oplus 8 \oplus 1 \text{ (baryons)}$$

The three components of the representation were identified as new fundamental particles, now known as *quarks*. At that time three flavors - up (*u*), down (*d*) and strange (*s*) – were known, with fractional electrical charges $+2/3e, -1/3e, -1/3e$. Hadrons are made up either of one quark and one antiquark or of three quarks. The quark model was confirmed with the discovery of the Ω^- (*sss*) at the theoretically predicted mass.

Independently, deep inelastic scattering experiments performed in the late sixties with electrons and protons confirmed that protons had a substructure. Feynman and Bjorken proposed the parton theory, identifying the constituents of the proton as quarks and introducing an additional type of neutral particles – "gluons"- responsible for their binding[17].

Today, quarks and leptons, both fermions, are still considered to be the basic building blocks of matter. Six different quarks are known in addition to the three leptons and their associated neutrinos. They are commonly organized by "generations" and by their electrical charge.

In addition to the fermions there are a number of fundamental bosons mediating the interactions between them. Figure 2-1 gives an overview of all particles of the Standard Model.
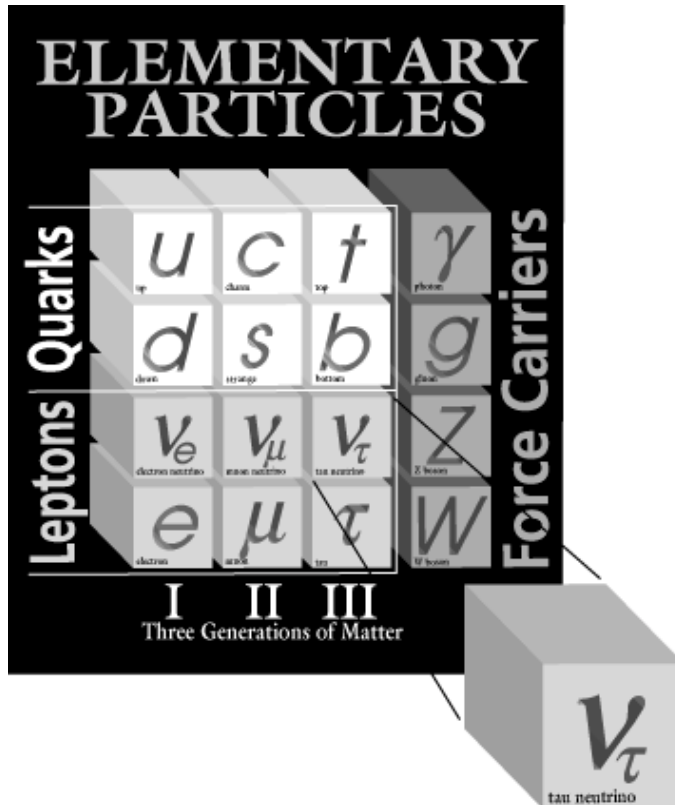
Figure 2-1: The particles of the Standard Model.

2.2.2 Interactions

All interactions between physical objects can be described by field theories. Non-quantized field theories include Maxwell's electrodynamics, the first formalism that contained expressions for fields, and Einstein's general theory of relativity. After the introduction of quantum mechanics in the 1920's, the need arose to find a field theory that was applicable to quantum objects.

Heisenberg and Pauli were the first to describe the basic principles of a quantized field theory in 1929[18]. However, in the original theories proposed to describe electromagnetic interactions between particles, some of the calculations resulted in

infinite results. Tomonaga[19], Schwinger[20] and Feynman[21] independently solved this problem in 1948 by a procedure that has since been known as *renormalization*.

The basic principle of quantum field theories is to introduce a local gauge transformation

$$\Psi(x) \rightarrow \Psi'(x) \equiv e^{i\alpha(x)}\Psi(x) \tag{2.2}$$

The covariance principle then demands that the free Dirac equation

$$(i\partial - m)\Psi(x) = 0 \tag{2.3}$$

be replaced by

$$(i\mathbb{D} - m)\Psi(x) = 0, D_\mu \equiv \partial_\mu + iA_\mu(x) \tag{2.4}$$

where the A_μ can be identified as the respective force fields, the simplest being the electromagnetic field. The local gauge can easily be generalized to

$$\Psi(x) \rightarrow e^{i\alpha_i(x)T^i}\Psi(x) \tag{2.5}$$

where the T^i are the generators of the SU(N) symmetry group. The first SU(2) gauge theory was introduced by Yang and Mills in 1954[22] and contained one neutral and two charged massless bosons. In 1967, Weinberg[23] and Salam[24] showed that the electromagnetic and weak interactions could be unified in a SU(2) x U(1) gauge theory. Using spontaneous symmetry breaking, they obtained three massive and one massless boson; the $W^\pm$, the Z and the photon.

Finally, Han, Nambu, Greenberg and Gell-Mann[17] extended the gauge principle to interactions between quarks. In order to reconcile the existence of particles such as $\Delta^-(uuu)$ with the Pauli principle, they postulated an additional quantum number called *color*. According to the corresponding theory, quantum chromodynamics (QCD), exchange of this property is facilitated by the 8 bosons of SU(3) gauge theory, the *gluons*.

2.2.3 The Electroweak Interaction

It has been mentioned above that neutrinos only interact by way of the weak nuclear interaction. The first attempt to describe weak nuclear interactions was made

by Fermi in 1934[25]. His theory did not include an intermediate boson, but correctly identified the coupling constant G as being universal to weak decay processes.

During the 1950s it was discovered that the decay of the K^+ did not always preserve parity. In 1956 Lee and Yang[26] postulated violation of parity conservation in weak decays. Only one year later, Wu et al.[27] demonstrated parity violation in the decay process $^{60}Co \rightarrow ^{60}Ni + e^- + \bar{\nu}$. It was soon followed by the discovery that parity violation is maximal[28], that is, all neutrinos are left-handed, and all antineutrinos are right-handed.

That result suggested an interaction of the form

$$H_{\text{int}} = \frac{G}{\sqrt{2}} \int d^3x [\bar{\psi}_p(x)\gamma_\mu(C_V + C_A\gamma_5)\psi_n(x)][\bar{\psi}_e(x)\gamma^\mu(1-\gamma_5)\psi_\nu(x)] \quad (2.6)$$

for the β-decay $n \rightarrow p + e^- + \bar{\nu}$. In this expression the term $(1-\gamma_5)$ projects out the right-handed state of the neutrino, while the C_i indicate the relative strengths of vector and pseudovector couplings.

Equation 2.6 remained the generally accepted form of the theory of weak interactions until 't Hooft proved the renormalizability of the unified electroweak gauge theory in 1971[29]. Here neutrinos (antineutrinos) are represented by two-component Weyl spinors ν_L ($\bar{\nu}_R$). Together with their charged counterparts they form doublets with respect to the weak interaction $SU(2)_L$ group, while the right-handed charged leptons transform as singlets without neutrino component.

The Lagrangians of the interactions involving neutrinos are described by:

$$L_{CC} = -\frac{G}{\sqrt{2}} \sum_{i=e,\mu,\tau} \bar{\nu}_{L_i}\gamma_\mu l_{L_i} W^\mu + h.c. \quad (2.7)$$

$$L_{NC} = -\frac{G}{2\cos\theta_W} \sum_{i=e,\mu,\tau} \bar{\nu}_{L_i}\gamma_\mu \nu_{L_i} Z^\mu + h.c \quad (2.8)$$

for charged and neutral currents. The massive bosons $W^\pm$ and Z appearing in these equations were discovered in 1983 at CERN[30], confirming the validity of the theory.

2.3 Non-Standard Model Neutrinos

2.3.1 Majorana Neutrinos

One of the most frequently considered extensions of the Standard Model is neutrino mass. As mentioned above, neutrino states can be expressed by two-component spinors that are solutions of the Dirac equation:

$$(i\gamma^\mu \partial_\mu - m)\psi = \begin{pmatrix} -m & i(\partial_0 + \sigma\nabla) \\ i(\partial_0 - \sigma\nabla) & -m \end{pmatrix}\begin{pmatrix} \psi_L \\ \psi_R \end{pmatrix} = 0 \qquad (2.9)$$

For $m=0$ there is no coupling between right- and left-handed components, in agreement with experimental observation. Therefore the two components can be described separately by the Weyl equation:

$$i(\partial_0 \underset{(+)}{-} \sigma\nabla)\psi_{L(R)} = 0 \qquad (2.10)$$

There are two different methods to introduce neutrino mass. The easiest is to postulate the existence of a Dirac mass term. This implies the existence of the two additional components ν_R and $\overline{\nu}_L$ that have not yet been observed.

Another way to describe massive neutrinos is the Majorana equation:

$$i(\partial_0 - \sigma\nabla)\chi - im\sigma^2\chi^* = 0 \qquad (2.11)$$

which for $m=0$ is identical to the Weyl equation. Two possible solutions are:

$$\chi = \frac{1}{\sqrt{2}}\left(\psi_L + \psi_L^C\right)$$
$$\omega = \frac{1}{\sqrt{2}}\left(\psi_R + \psi_R^C\right) \qquad (2.12)$$

with $\chi = \chi^C$ and $\omega = \omega^C$, so the particles described by this theory are their own antiparticles. The generalized mass Langrangian can then be written as:

$$L_{mass} = (\overline{\chi}, \overline{\omega})\begin{pmatrix} A & D \\ D & B \end{pmatrix}\begin{pmatrix} \chi \\ \omega \end{pmatrix} \qquad (2.13)$$

where A and B are new, while the D correspond to the old Dirac mass term. By diagonalizing the matrix one gets the two mass eigenstates:

$$M_{1,2} = \frac{1}{2}\left[(A+B) \pm \sqrt{(A-B)^2 + D^2}\right] \tag{2.14}$$

By choosing $B \approx \frac{1}{A} \approx 0, D \ll A$ the two masses are become approximately

$$M_1 \cong A$$

$$M_2 \cong \frac{D^2}{A} \tag{2.15}$$

This "see-saw" mechanism generates two different mass scales, one very heavy (M_1), and the other one very light (M_2). The light solutions can be identified with the known neutrinos while the heavy ones do not contradict known observations, provided that their mass is sufficiently large. The description of neutrinos as Majorana particles is favored by almost all extensions to the Standard Model[31]. Any unknown effects that could have an impact on this experiment would therefore be more likely if there was experimental evidence for neutrinos to be Majorana particles.

One distinctive feature of this approach is lepton number violation, caused by the identity of neutrinos and antineutrinos. It has been shown[32] that the neutrinoless double beta decay $(\beta\beta)_{0\nu}$ occurs if and only if neutrinos are massive Majorana particles. The best limit on this process has been set by the HEIDELBERG-MOSCOW experiment[33] investigating the decay $^{76}Ge \rightarrow ^{76}Se + 2e^-$. Their negative result corresponds to an upper limit on the effective Majorana neutrino mass of $m_{\nu_e,Maj} < 0.35\ eV$, $90\%\ C.L.(0.27\ eV, 68\%\ C.L.)$.

2.3.2 Model Independent Mass Measurements

There are several experimental techniques that can be used to search for a finite neutrino mass. The most straightforward are direct kinematic searches.

ν_e: The best limit has been set by investigation of the tritium beta decay $^3H \rightarrow ^3He + e^+ + \nu_e$. Two experiments have published results.

- Troitsk[34]: $m_{\nu_e}^2 = -1.9 \pm 3.4(stat.) \pm 2.2(sys.)eV^2c^{-4}$

- Mainz[35]: $m_{\nu_e}^2 = -1.8 \pm 5.1(stat.) \pm 2.0(sys)eV^2c^{-4}$

An interesting feature of these two measurements is that their central value corresponds to an imaginary value for the neutrino mass. However, the large error

margin leaves enough room for a neutrino with real mass, and there is always the possibility of some unaccounted-for systematic effect.

The Particle Data Group also bases its official limit for the v_e mass on Tritium experiments, their evaluation leads to a value of $m_{v_e} < 3\,eV$ [36]. Independently, the electron neutrino mass has been measured using neutrinos from supernova 1987A. Limits derived from comparison of photon and neutrino arrival times correspond to a neutrino mass $m_{v_e} < 15\,eV$ [37].

v_μ : A limit for the muon neutrino mass has been set using the decay channel $\pi^+ \to \mu^+ v_\mu$. Currently, the limit is $m_{v_\mu} < 190\,keV$ [38].

v_τ : Several results for limits on the tau neutrino mass inferred from tau decays have been published. The limit accepted by the Particle Data Group is $m_{v_\tau} < 18.2\,MeV$. For a discussion of the fitting technique and a summary of published results see ([39]).

There are also indirect methods that can be used to probe the neutrino mass. One of them is the limit from cosmological considerations. The currently favored cosmological model, assuming for the total neutrino energy density as a fraction of the critical energy density of the universe $\Omega_v h^2 < 0.1$, leads to:

$$m_{tot} \equiv \sum_v \frac{g_v}{2} m_v < 8eV \tag{2.16}$$

with $g_v = 2\,(4)$ for Majorana (Dirac) neutrinos[40].

Finally, the connection between the magnetic moment and the mass of a neutrino can be used to obtain a limit. The two are related by

$$\mu_v = \frac{3eG}{8\pi^2 \sqrt{2}} m_v = 3.1 \times 10^{-19} \mu_B \left(\frac{m_v}{1\,eVc^{-2}} \right) \tag{2.17}$$

Mass limits from magnetic moment limits are currently several orders of magnitude worse than those using other methods. An overview of current limits is given in Table 2-1. Constraints on neutrino masses also place limits on the magnitude of effects like neutrino decays and oscillations, whose relevance for this experiment will be described in the subsequent sections.

Neutrino	Magnetic moment limit	Mass limit (from μ)	Mass limit (PDG, 01/00)[36]
ν_e	$< 1.8 \times 10^{-10} \mu_B$ [41]	$< 5.8 \times 10^8\, eV$	$< 3 eV$
ν_μ	$< 7.4 \times 10^{-10} \mu_B$ [41]	$< 2.4 \times 10^9\, eV$	$< 190 keV$
ν_τ	$< 3.9 \times 10^{-7} \mu_B$ [42]	$< 1.3 \times 10^{12}\, eV$	$< 18.2 MeV$

Table 2-1: Mass and magnetic moment limits for neutrinos. The middle column shows the mass limit corresponding to the magnetic moment limit (see equation 2.17).

2.3.3 Neutrino Oscillation Theory

An interesting feature of massive neutrinos is that they can oscillate from one flavor to another. The basic principle is the distinction between weak eigenstates ν_w and mass eigenstates ν_m. Instead of assigning distinct flavor eigenvalues to the individual neutrinos, this extension to the Standard Model treats the three known observable neutrino types as mixtures of several massive states.

The phenomenon of neutrino (two-) flavor oscillations can be described by an equation of the form:

$$P(\nu_1 \rightarrow \nu_2; L) = \sin^2 2\theta \sin^2\left(\frac{1.27 km^{-1} \cdot \delta m_{1,2}^2 [eV^2] \cdot L}{E_\nu [GeV]}\right) \qquad (2.18)$$

where θ stands for the mixing angle. The result for P then corresponds to the probability of oscillation from ν_1 to ν_2 with a mass difference $\delta m_{1,2}$ for neutrinos of energy E_ν over a flight length L.

Other experiments have already set limits on oscillations between the three observed neutrino flavors that are beyond the sensitivity of this experiment. However, many theories include a fourth – sterile – neutrino. Since the tau neutrino has never before been directly observed, no limits on oscillations between it and a potential fourth neutrino could be set. A more detailed discussion of theory and experimental results, as well as a discussion of how oscillations might affect the observation of tau neutrino interactions, is given in Appendix C.

2.3.4 Massive neutrino decay

Other than through oscillations, there is also the possibility of the decay of a massive neutrino into other particles. Cosmological arguments show that any neutrino with mass 100 eV – 24 MeV has to be unstable if current models for nucleosynthesis are correct[43].

There are two different "non-exotic" decay modes for neutrinos with mass $m_\nu < O(10\ MeV)$:

$$\nu_H \rightarrow \nu_L + \gamma$$
$$\nu_H \rightarrow \nu_L + e^- + e^+$$

(2.19)

The corresponding Feynman diagrams are shown in Figure 2-2 and Figure 2-3. The calculation for the transition amplitude is discussed at length in ([44]). The second decay mode is found to be dominating above threshold ($m_\nu > 2m_e$). The lifetime decreases proportionally to m_ν^5 with a value of $\tau_\nu \cong 10^{-2}\ years$ near threshold.
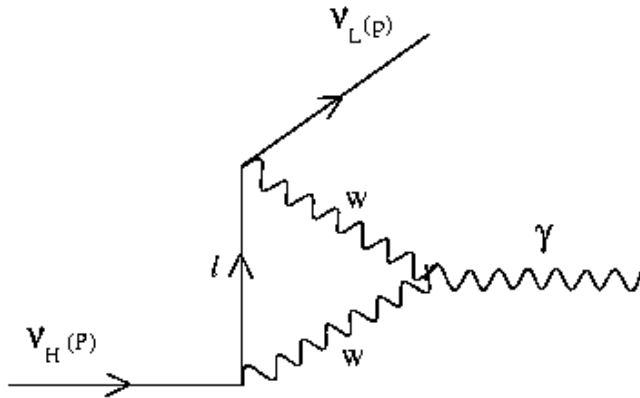
Figure 2-2: Massive neutrino decay into gamma, light neutrino.
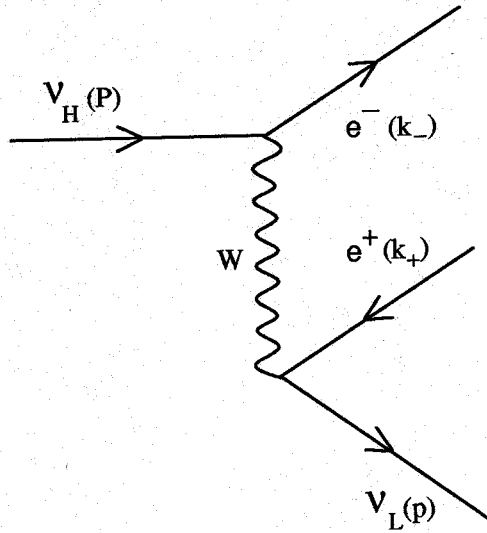
Figure 2-3: Massive neutrino decay into light neutrino, e⁺ and e⁻.

Therefore, the lifetime for a *1.1 MeV* neutrino is of the order of 10^{-2} years, or 3×10^5 sec. Since the lifetime decreases with the fifth power of the mass, one can estimate the decay probability for a neutrino:

$$P(\nu_\tau, decay) = 1 - \exp(-\gamma c\tau) = 1 - \exp\left(-\frac{m_\nu c^2}{E_\nu} \cdot \frac{L}{c} \cdot 3\times10^5 \text{ sec}\cdot\left(\frac{1.1\,MeV}{m_\nu}\right)^5\right) \quad (2.21)$$

For a tau neutrino with the highest mass allowed by experimental constraints, $m_{\nu_\tau} = 18.2\,GeV$, and energy of *5 GeV*, the probability for decay in this particular theory is $O(10^{-10})$ for the E872 experimental setup. This value is beyond the sensitivity of the apparatus.

However, no direct measurement of the tau neutrino lifetime has been done so far, as shown in Table 2-2. This leaves open the possibility of an unknown effect leading to decay of the ν_τ in flight and consequent decrease of the interaction yield.

Neutrino	Lifetime Limit	Comment
ν_e	$\tau > 5.7 \times 10^5 (m_{\nu_e}/eV)\sec.$ [45]	From SN1987A, no oscillation
ν_μ	$\tau > 15.4 (m_{\nu_e}/eV)\sec.$ [36]	LAMPF E225 collaboration
ν_τ	-	No official limit from PDG

Table 2-2: Lifetime limits for the three known neutrino types.

3 Experimental Setup

3.1 Introduction

The goal of this experiment was the direct observation of ν_τ charged-current interactions. The apparatus was built around a hybrid emulsion-electronic spectrometer (HES), whose design was based on similar systems used in Fermilab experiments E531[46] and E653[47]. A neutrino beam was produced using an 800 GeV proton beam impinging on a tungsten target, and the flux of background particles was reduced by a combination of passive shielding and sweeping magnets. Neutrino interactions occurred in nuclear emulsion modules, and event analysis was done using data both from the emulsion and an electronic spectrometer. The same technique was used in the experiment CHORUS[48] at CERN and was proposed for the FNAL Main Injector experiment COSMOS[49].

Nuclear emulsion is a "permanently active" medium, recording data regardless of electronic triggering, and because of its high price the available quantity was limited. This was a significant constraint in minimizing the background track density and maximizing the fraction of tau neutrinos in the beam.

Figure 3-1 gives an overview of the general philosophy of the neutrino beam production and emulsion target. A picture of the spectrometer is shown in Figure 3-11.

The principal sources for tau neutrinos are decays of charmed mesons, mainly D_s produced in the beam dump. In order to maximize the fraction of tau neutrinos, the beam dump had to be designed so that pions and kaons would reinteract before they could decay and produce other types of neutrinos (mainly ν_μ).
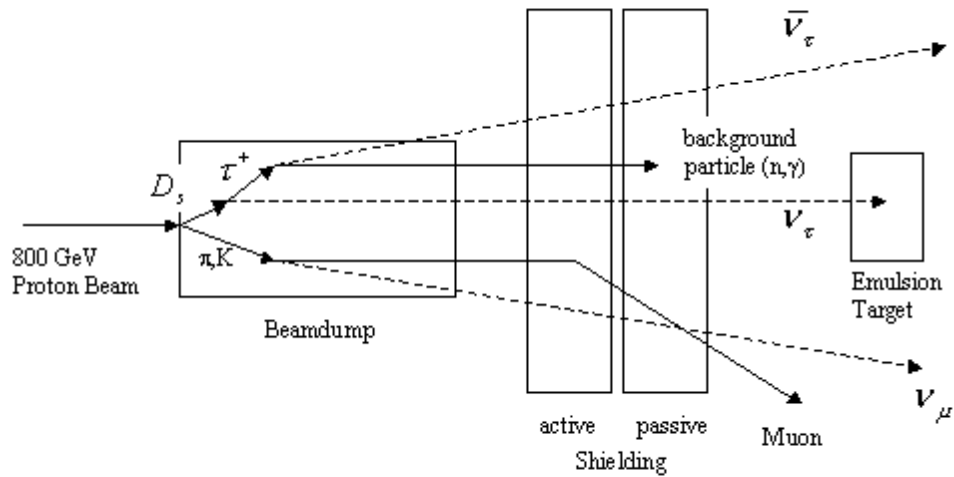
Figure 3-1: General principle of the neutrino beam and target.

The intense flux of background particles that always emanate from a beam dump provided a major problem. In addition to the expected muon background, significant contributions coming from thermal neutrons and soft gamma rays were identified in the test run.

A neutrino beam cannot be focused and spreads out over an increasing area with distance. Reducing the background by moving the target farther away thus leads to a reduction in neutrino flux. Therefore it was necessary to construct an elaborate combination of active and passive shielding systems to maintain a short distance between beam dump and target.

Muons were both swept away from the beam axis by dipole magnets and absorbed by large amounts of bulk material. To avoid the problem of reinteracting muons, shielding material was omitted in places of high muon flux as shown in Figure 3-2.
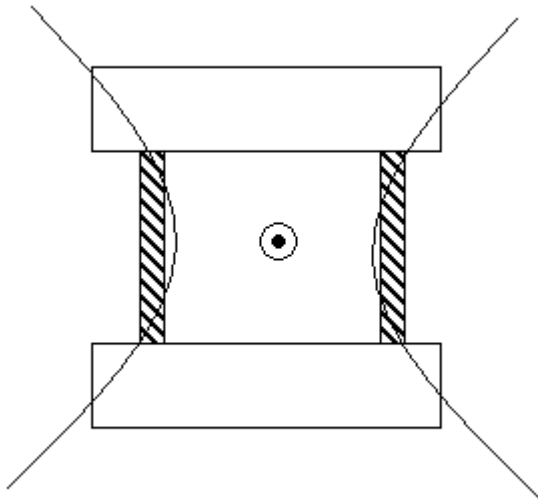
Figure 3-2: Sketch of material omitted in the passive shielding to reduce muon interactions. Circle with dot: beam axis; hatched area: omitted material; curved lines: approximate boundaries of muon "plume".

Electronic components were included for two purposes. Because of the high background track density, it was estimated that it would take approximately 100 years to scan the entire emulsion volume[50]. To accomplish the scanning process within a reasonable timeframe it was necessary to reduce the scanning volume by predicting the vertex location as accurately as possible. This was accomplished by placing scintillating fiber planes between the emulsion modules.

Secondly, event analysis required information about momentum and types of the particles produced in the interactions. It was provided by a conventional spectrometer, in which several drift chambers were used in conjunction with a dipole magnet. A calorimeter measured the energy of electromagnetic showers, and muons were identified by a specifically designed set of detection planes.

To ensure that only events with the right signature – no tracks entering the target volume, several coming out of it – were recorded, a veto wall and three trigger planes were installed. Electronic data acquisition was done using the standard Fermilab DART system.

The experimental hardware can be broken down into four main elements:

- A beam dump in which the neutrino beam is produced and the shielding system providing an attenuation of background particles.

- The emulsion target, in which the neutrino interactions occurred and the adjoined scintillating fiber planes.
- A spectrometer used to track and identify the daughter products of the interactions.
- Trigger and data acquisition systems to record the events.

For the purpose of this thesis, the spectrometer and electromagnetic calorimeter were of particular importance. Momentum data were obtained solely by using the downstream drift chamber system and the vertex location. The calorimeter measured electromagnetic energies. The emulsion system and the scintillating fibers were used implicitly because they provided vital information about the vertex location. However, no work was done specifically for this thesis using either of those two systems. Also excluded were the Vector Drift Chambers, because of their typically high multiplicity of hits, making track reconstruction impossible for most events.

The following is a detailed description of the individual components.

3.2 Neutrino Beam

The neutrino beam was generated using 800 GeV protons provided by the Fermilab Main Accelerator (Tevatron). The experiment was located on the Proton West (PW) beamline, which had been modified to accommodate beam intensities of up to 10^{13} protons per spill.

The maximum tolerable density of charged tracks in the emulsion integrated over the exposure of the individual modules ($\approx 10^{17}$ protons on target) was estimated to be of the order of $10^5 / cm^2$. The primary background sources were muons, photons and thermal neutrons. This value corresponds to a rate of 500 Hz during the beam spill. The unattenuated charged particle flux rate for a target located 35 m from the beam dump was estimated to be 10^7 Hz, so there had to be a reduction by a factor of the order of 10^5. The system used to achieve this reduction was a combination of passive shielding and active sweeping magnets, as illustrated in Figure 3-3. Its design was based on a Monte Carlo simulation of the shield using a code called *TRAMU*. It was modified from its original source[51] to gain speed and allow the inclusion of an external muon source.
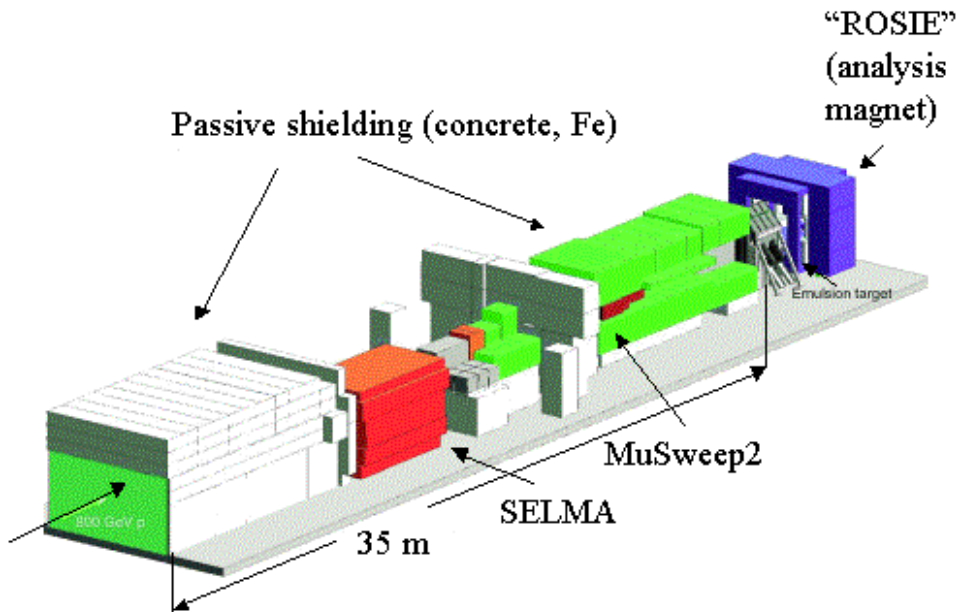
Figure 3-3: Overview of the shielding system.

3.2.1 Beam dump

The beam dump was a block of tungsten alloy[*] 10 cm x 10 cm in cross section and 102 cm long, corresponding to 10.4 nuclear interaction lengths. This ensured that only about one out of one thousand pions decayed before reinteracting. It was surrounded by a 10 cm jacket of copper connected to a closed-circuit radioactive water (RAW) system that removed the ≈25 kW of heat generated by the proton beam (Figure 3-4).

The design of the beam target provided an alternative configuration that was intended to be used for a more detailed investigation of background sources. This was the "half density side", consisting of 25 mm wide strips of tungsten separated by 25 mm of air. This mode was not used effectively during the run

---

[*] "Heavimet", containing about 10% Cu, Ni and Fe

.
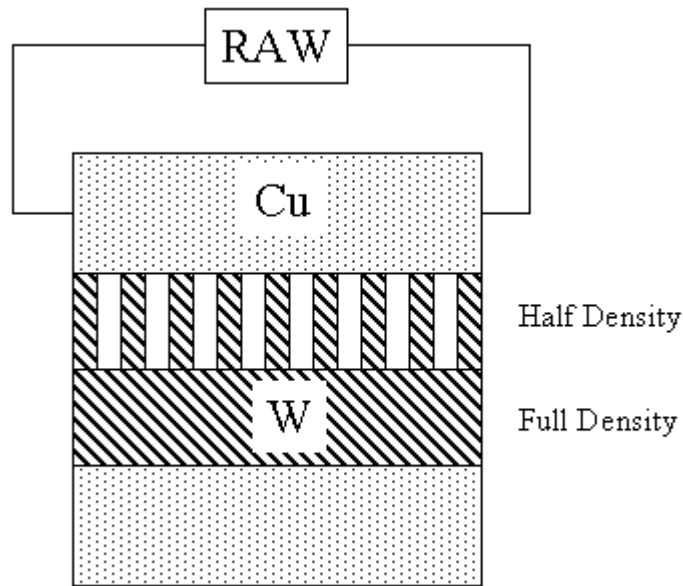
Figure 3-4: Sketch of the beam dump with copper jacket and cooling system.

3.2.2 Active Shielding

Two sweeping magnets were located immediately downstream of the beam dump (see Figure 3-3).

- "SELMA" was the previously installed dipole magnet PW8AN1, with a length of 7.4m and a vertical field of 3.2 T.
- "MuSweep2" was installed specifically for this experiment and had a vertical magnetic field of 1.9 T over a length of 5m. The design and function was similar to the sweeping magnet used in the KTeV experiment[52].

The effect of the sweeping system was to form two horizontal "plumes" of muons separated by about 2 meters at the position of the emulsion target. Figure 3-5 shows the distribution of the muon plume as measured during a calibration ("PW5") run.

3.2.3 Passive Shielding

The passive shielding, consisting of more than 500 tons of steel and concrete, extended over a total length of 18 m. Much of the steel had previously been part of the E705/771 downstream muon system[53]. During the early phase of the run, an unexpectedly high rate of background was discovered, and lithium iodide detectors were placed at eight different locations along the beamline to investigate its source. The flux was found to be consistent with thermal neutrons and soft gamma rays emitted by activated material[54]. Additional lead and concrete shielding was installed around the target hut, reducing thermal neutron flux by about 95%[55].

After installation of this additional shielding and the rearrangement of the shielding material as shown in Figure 3-2, the background flux was reduced to a level that can be tolerated by emulsion.
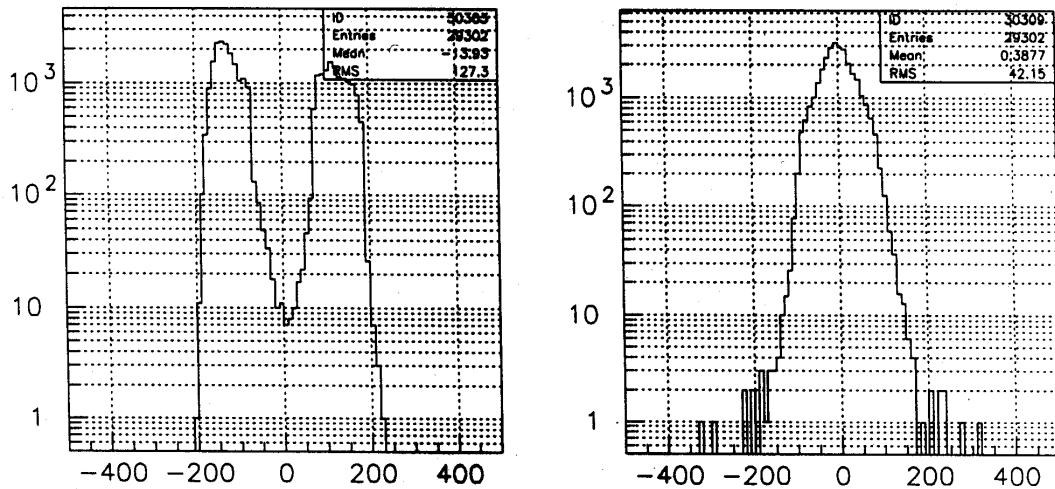
Figure 3-5: Horizontal (left) and vertical (right) distribution of the muon plume at the position of the muon-ID walls. The x-axis shows the position relative to the beam axis in centimeters.
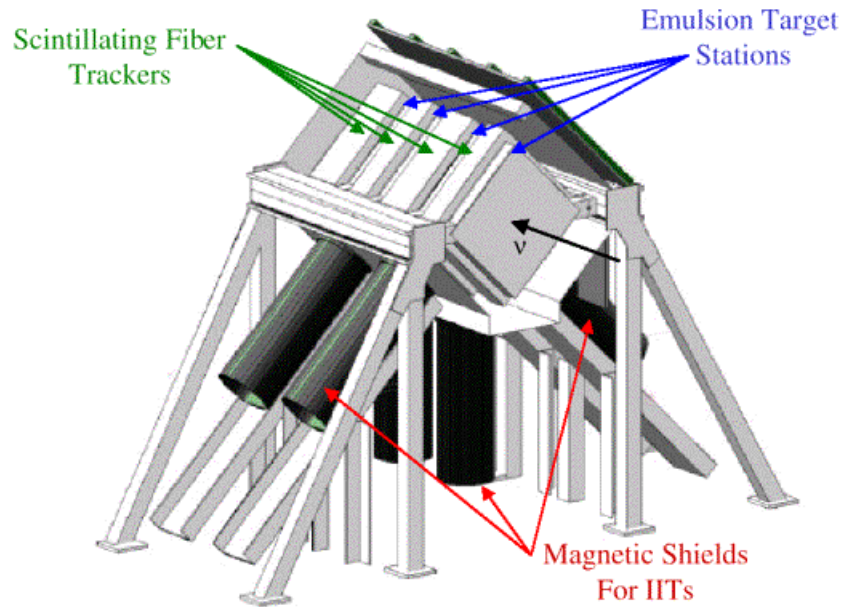
Figure 3-6: Target Stand.

3.3 Target Area

The target area was located 35 m downstream from the end of the beam dump, and contained both emulsion modules and several scintillating fiber planes used to track charged particles produced in the interactions. It was encased by a layer of lead 13 mm to 20mm thick to protect it from ambient radiation during the data taking. An overview of the target area is given in Figure 3-6.

3.3.1 Emulsion Target

The main goal of this experiment – observation of tau neutrino interactions – required identification of tau leptons. The signature of a tauon decaying into a single charged daughter, occurring in 86% of all tau decays, is a charged track that appears to have a "kink" at the position of the decay. For typical neutrino energies

($\approx 100\, GeV$) one can expect the kink angle to be of the order of a few tens of milliradians, with a primary track length of millimeters or less. To allow identification of tau events, the detector has to be able to record charged tracks with a spatial resolution in the micrometer range. Nuclear emulsion fulfills all these requirements.

The emulsion itself consisted of silver bromide crystals embedded in gelatin. These turned into small grains of silver with a diameter of ≈0.2 μm when hit by a charged particle, and after development formed visible spots ≈0.8 μm in size. The target consisted of up to four separate modules each made up of 50 to 80 individual sheets. The sheets were 50 cm x 50 cm in cross section and compressed together under vacuum to form a solid unit with a thickness of 6 to 7 cm.

Two factors, other than the constraints imposed by the required resolution, were decisive in the design of the emulsion modules. One was the high price of nuclear emulsion - about $300K for 100 kg. The other was the desire to have as massive a target as possible in order to maximize the number of neutrino interactions. In this experiment, two different methods were used (see Figure 3-7).

- Conventional "bulk" emulsion, as used in several previous neutrino experiments[46,47,48]. In "bulk" modules, emulsion accounted for 95% of the total mass. Each module had 84 sheets made of a 90 μm thick plastic base coated with 330 or 350 μm of emulsion. The total thickness of this module type was 7cm and it contained 15 liters of emulsion gel.

- The "ECC" (emulsion cloud chamber) type module, first used for the specific purpose of recording neutrino interactions in E872, is a less costly alternative. The name came from the fact that the concept is similar to the cloud chambers that were widely used several decades ago. In this design sheets of stainless steel make up most of the mass, while emulsion is applied only in thin layers between those sheets. As opposed to the bulk configuration, this type of module is not a volume-tracking detector. Rather, it is a sampling detector comparable to a system using pixel planes.

25

ECC type emulsion modules have both advantages and disadvantages. Obviously the mass is higher with less emulsion, resulting in more interactions at a lower cost. Furthermore, background tracks resulting from soft γ–rays are less frequent than in the conventional type. The downside is that since only individual points along tracks are recorded, the probability of mismatching tracks is higher. Also, most interactions will occur in the steel, and it is possible that the tau lepton decays before reaching the subsequent emulsion layer. This leads to uncertainties regarding the event topology and makes correct identification of the event more difficult. Finally, secondary interactions simulating decays are harder to exclude if they occurred in the passive material because low energy tracks from nuclear breakup do not reach the next emulsion plane and hence cannot be seen.

Two different ECC configurations were used, ECC200 and ECC800, named after the thickness in microns of the plastic base. Figure 3-7 shows the three different module types and illustrates the way each of them would record a short decay typical tau event.

In addition to the modules themselves, "changeable sheets" were mounted in front of and behind every module. Each of these single emulsion sheets was replaced frequently during the run, so their track density was much lower than in the modules themselves. This permitted better linking of the emulsion tracks to tracks recorded electronically in the scintillating fiber system. Alignment of changeable sheets with the modules was accomplished through use of a set of 16 ^{55}Fe radioactive sources located on the supporting structure.

Bulk

420/440 µm

$2X_0$

330/350 µm emulsion (white), 90 µm plastic base (hatched)

ECC200

1350 µm

$3X_0$

985 µm steel (solid), 80 µm emulsion (white), 205 µm base (hatched),
80 µm emulsion

ECC800

2000 µm

$\approx 2.5X_0$

1000 µm steel (solid), 100 µm emulsion (white), 800 µm base (hatched),
100 µm emulsion
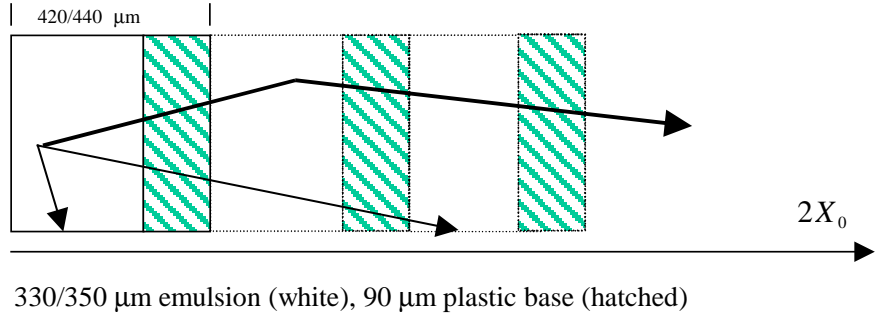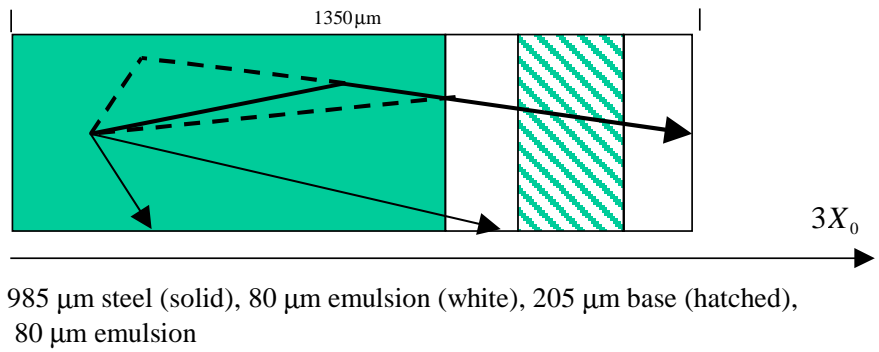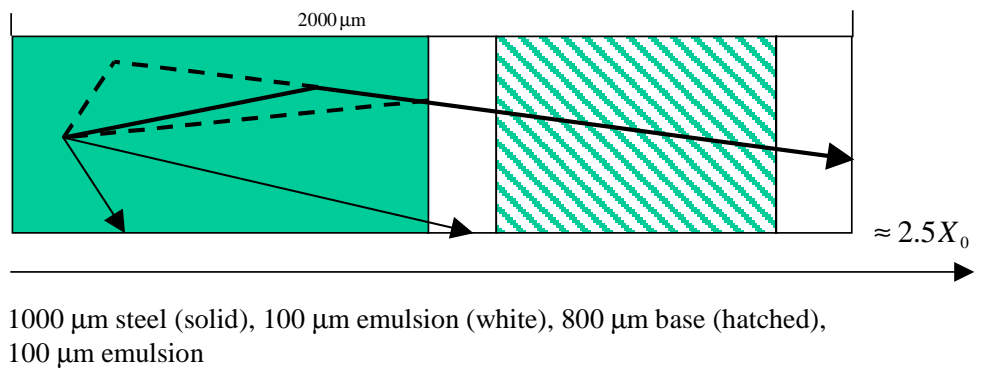
Figure 3-7: The different types of emulsion modules with example for tau CC event (short decay). Bold arrow: tau and charged daughter, bold dashed: ambiguities, thin arrows: other charged primary tracks.

System	z-position [cm][*]
Emulsion Station 1	1.52
SF1	19.9
Emulsion Station 2	30.2
SF2	48.6
Emulsion Station 3	59.5
SF3	77.9
Emulsion Station 4	88.5
SF4	114.8

Table 3-1: Position of systems in target area.

3.3.2 Scintillating Fibers
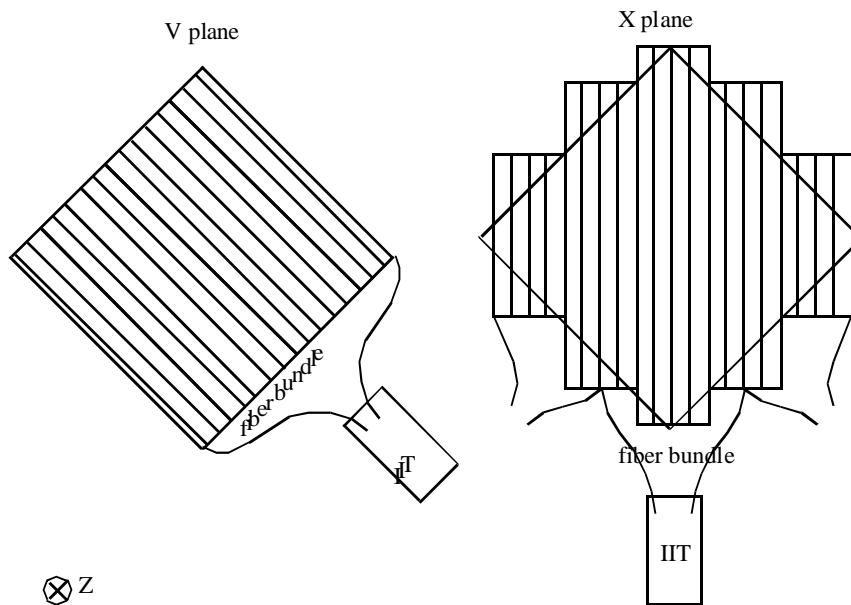
Figure 3-8: Layout of the scintillating fiber planes.

[*] Center of system relative to upstream end of emulsion station 1 (2.909m upstream of center of analysis magnet).

Several scintillating fiber planes were installed behind each of the emulsion modules to allow electronic vertex reconstruction. Their orientations are shown in Figure 3-8.

A total of 60000 scintillating fibers were used, distributed over 4 units, each consisting of several individual planes. The fibers had a diameter of 0.5 mm and varied in length between 0.7 m and 1.2 m. An aluminum mirror mounted on one end was used to increase the light output on the other side. The pulse height variation over the length of the fiber was measured to be less than 15%.

The planes were oriented in 3 directions. Their names indicate the coordinate measured.

- *x*, representing vertical orientation, with 1615 fibers.
- *u*, oriented at +45° to the vertical with 1132 fibers.
- *v*, at -45° to the vertical also having 1132 fibers per plane.

The fibers were placed side by side and covered an area of 56 cm x 56 cm per plane as shown in Figure 3-8. Every unit had one single *x* plane, but there were two variants with different numbers of *u* and *v* planes.

- Type I, located behind modules 1 and 3, with 6 *u* and 6 *v* planes.
- Type II, located behind modules 2 and 4, with 4 planes in both orientations.

Table 3-1 shows the position along the beam axis of emulsion modules and scintillating fiber planes.

Fibers were read out by six image intensifier (IIT) modules placed in large soft-iron canisters to shield them from the fringe field of the analysis magnet. Figure 3-9 illustrates how the system worked. Light coming from the fibers was used to produce electrons in a photocathode. The electrons were accelerated by an electric field of several thousand volts and focused onto a phosphor screen where they produced more photons. A fiber-optic plane composed of millions of small-diameter fibers directed those photons to another photocathode. This process was repeated four times leading to an overall light multiplication factor of $3-4\times10^6$. The quantum efficiency of the individual photocathodes was 20%.

The fourth phosphor screen was connected to a 768x493 pixel CCD video camera. Each scintillator was thereby mapped onto an area with a diameter of 3 pixels. A custom-built ADC read out the CCD camera at a rate of 24 MHz. The mean readout time for a single event was 24 ms, making the scintillating fiber system the dominant factor in the deadtime for data acquisition.

The complexity of the IIT system made it impossible to map the fiber positions to the CCD coordinates during assembly. For this reason, an optical calibration system was installed in which several fibers per plane were connected to an electroluminescent plate. These "fiducial" fibers were illuminated between runs and provided the necessary information to generate a map that was accurate to a fraction of the diameter of a pixel. Figure 3-10 shows the resolution of the scintillating fiber planes measured during a calibration run.
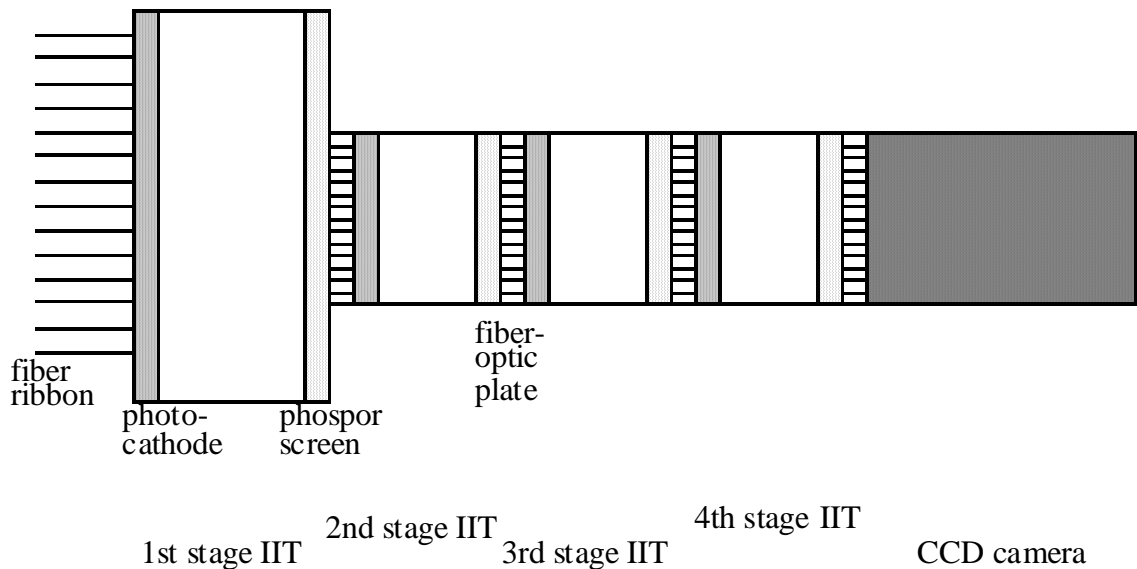
Figure 3-9: Schematic view of Scintillating Fiber readout system.
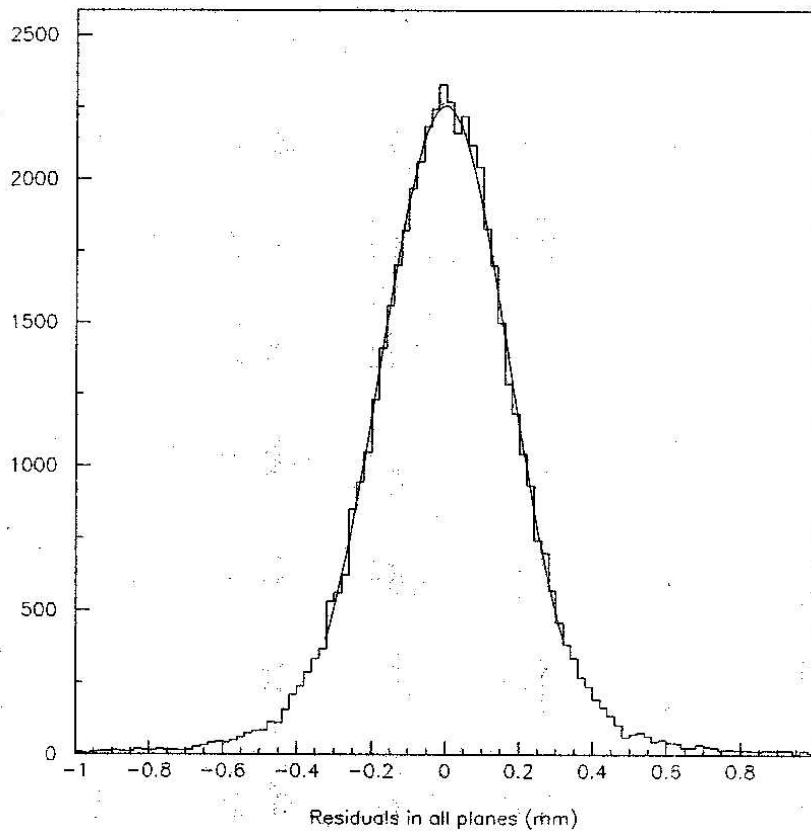
Figure 3-10: Measured Scintillating Fiber resolution in calibration run (single muon tracks).

3.4 Spectrometer

Figure 3-11 shows an overview of the spectrometer. Neutrinos enter the area from the lower right. The interactions used in the analysis occur in the target area described above. Drift chambers are positioned downstream on both sides of the analysis magnet ("ROSIE"), which provided a transversal momentum "kick" of 225 MeV. The remaining elements are the electromagnetic calorimeter and the muon ID walls at the downstream end.
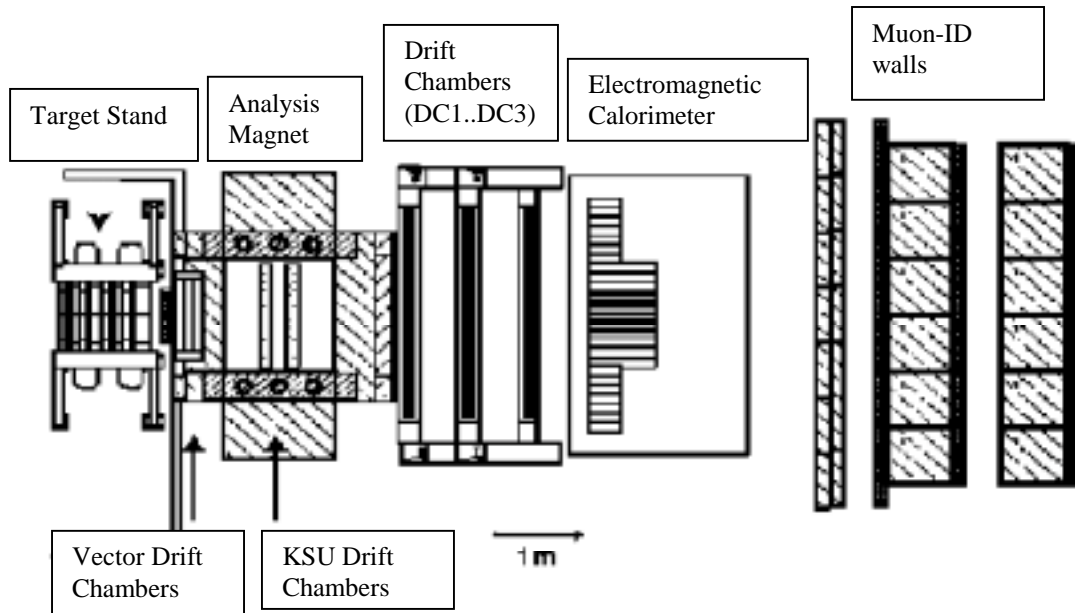
Figure 3-11: Overview of the spectrometer.

3.4.1 Drift Chambers

There were three separate sets of drift chambers, one upstream, one downstream and one inside the analysis magnet.

- The first three drift chambers were located 44 cm ahead of the upstream mirror plate of the analysis magnet. They had previously been used as vertex drift chambers (VDC) in the experiment E665[56].

- Another three drift chambers (DC1..3) were located downstream of the analysis magnet. DC1 had previously been used in the E705/771[53], DC2 and 3 in E557/683[57].

- Two more drift chambers, KSX and KSY, so named because they were built at Kansas State University and oriented to measure horizontal (x) and vertical (y) particle coordinated, were added during the run. KSY was in place for about 2/3, KSX for only 1/3 of the run.

The exact specifications for the drift chambers are given in Table 3-2.

For the analysis described in this thesis, only the downstream drift chambers and to a very limited extent, the upstream chamber inside the magnet were used. The

reason for this restriction was the high multiplicity of tracks in most events caused by electromagnetic showering in material downstream of the interaction vertex. Data from the KSX/KSY chambers was of better quality but available only for part of the event sample. The unrestricted use of those systems would therefore have presented the risk of introducing a bias to the data.

Figure 3-12, Figure 3-13 and Figure 3-14 show efficiencies and resolutions of the individual drift chambers measured during a calibration run with single muon tracks. Figure 3-15 shows the resolution of the KSY chamber. The value shown is the residual for reconstructed tracks in dependence of the distance to the next sense wire. Figure 3-16 illustrates the global alignment of the spectrometer system. The quantity shown corresponds to the measured bend angle for muons with the analysis magnet turned off. The tracks were reconstructed using information from all available systems. Any offset of the distribution therefore indicates a misalignment between the systems while the spread is a measure of the overall resolution.
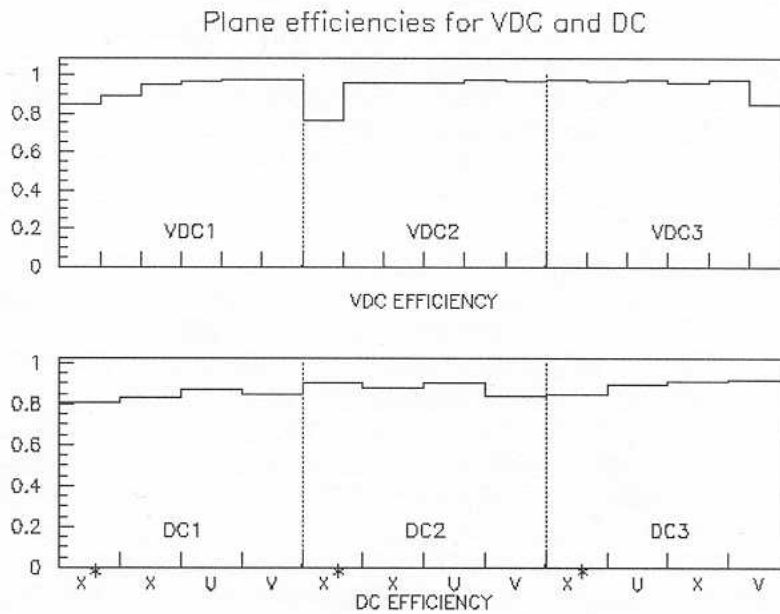
Figure 3-12: Drift Chamber efficiency (calibration run, single muon tracks).
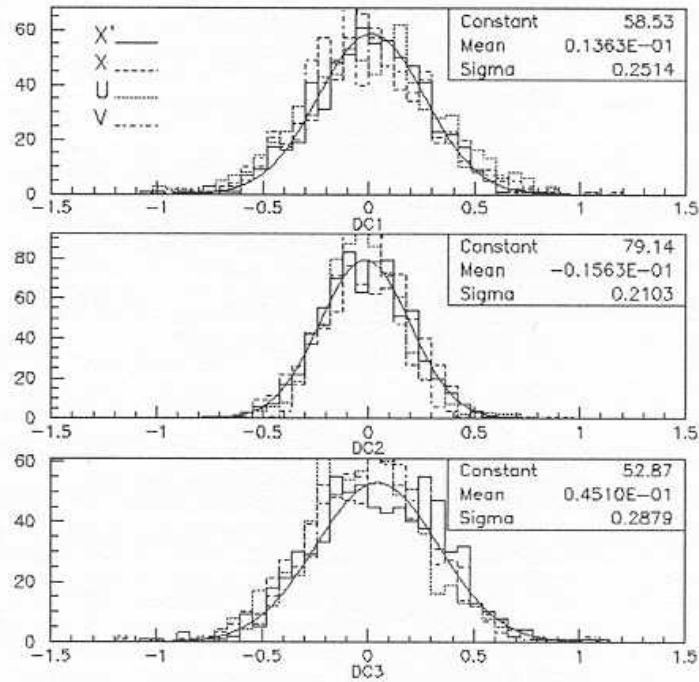
Figure 3-13: Measured DC resolution (calibration run, single muon tracks). X-axis in mm.
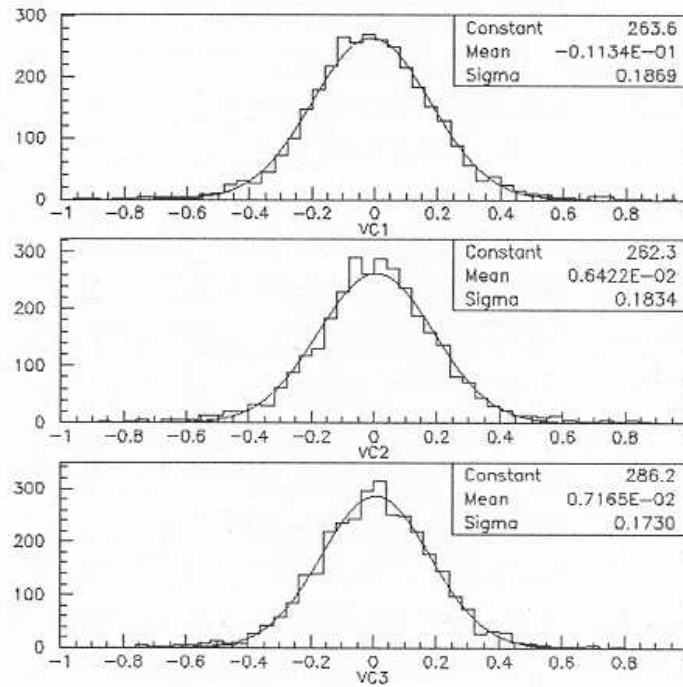
Figure 3-14: Measured VDC resolution (calibration run, single muon tracks). X-axis in mm.
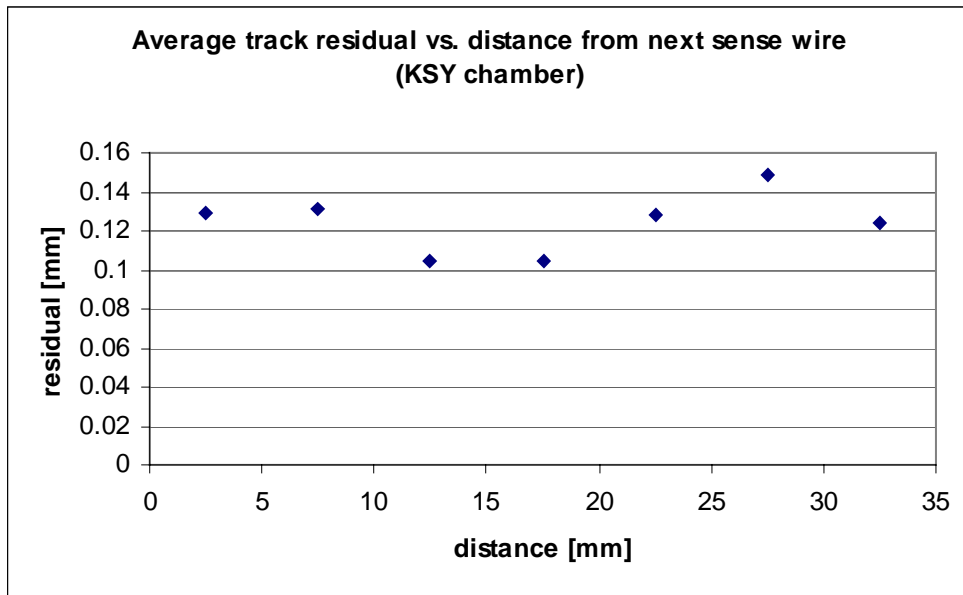
Figure 3-15: Measured resolution for KSY drift chamber (calibration run, single muon tracks).
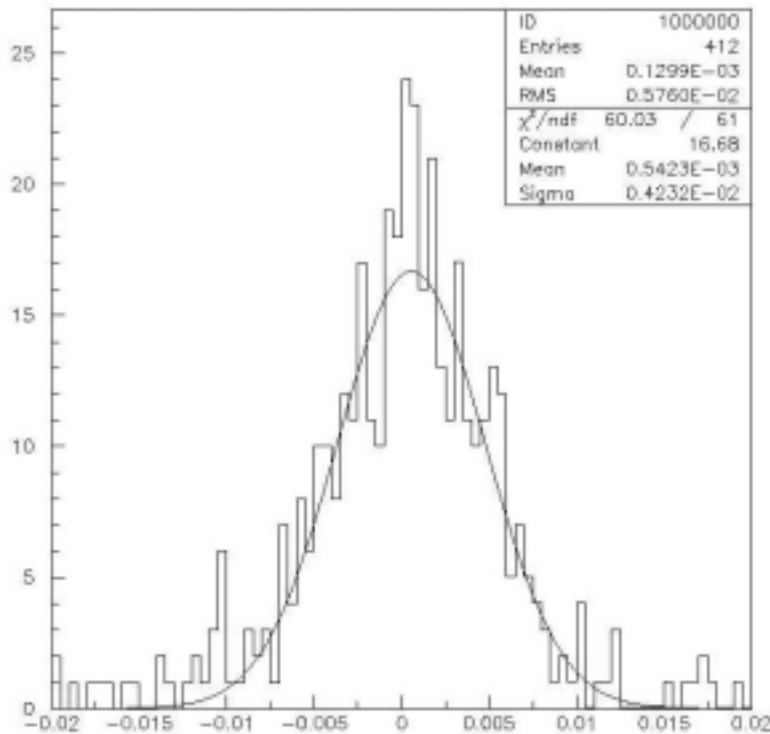
Figure 3-16: Overall drift chamber/scintillating fiber alignment (calibration run). The scale of the x-axis indicates bend angle in mrad/ 0.225 (corresponding to 1/p in momentum measurement).

Name	Position[*]	Orientation	Active Area [cm x cm]	Planes	Sense wires per plane	Resolution [μm]
VDC1	-1.294	0°	100 x 70	6	16	200
VDC2	-1.224	-4.2°(u')	100 x 70	6	16	200
VDC3	-1.153	+4.2°(v')	100 x 70	6	16	200
KSX	-0.0945	0°	140 x 100	4	17	150
KSY	0.267	90°	140 x 100	4	22	150
DC1	1.818	2 x 0°/±16.7° (x, x', u'', v'')	223 x 160	4	160[**]	350
DC2	2.623	2 x 0°/±16.7°	330 x 160	4	176/192	350
DC3	3.432	2 x 0°/±16.7°	330 x 160	4	176/192	350

Table 3-2: Drift chamber properties.

3.4.2 Electromagnetic Calorimeter

High-energy electrons are produced in ν_e charged-current interaction as well as in tau decays. On their passage through material they produce electromagnetic showers. A calorimeter can measure the energy of those particles in each shower that hit its active area. This information can be used to obtain an estimate for the energy of the original electron. Since ν_e events deposited more electromagnetic energy than other neutrino interactions, the energy spectrum from the calorimeter was used in the

---

[*] relative to center of magnet
[**] not all active

analysis as an independent data sample for the investigation of the event sample composition.

The calorimeter was composed of 400 individual blocks covering a total area of 3.75m x 1.95m. There were three separate regions, as shown in Figure 3-17.

- The central region, containing 10x10 small (7.5cm x 7.5cm) scintillating glass blocks to improve position resolution in this area.
- The intermediate region, formed from 74 larger (15cm x 15 cm) scintillating glass blocks.
- The outer region with 224 lead glass blocks.
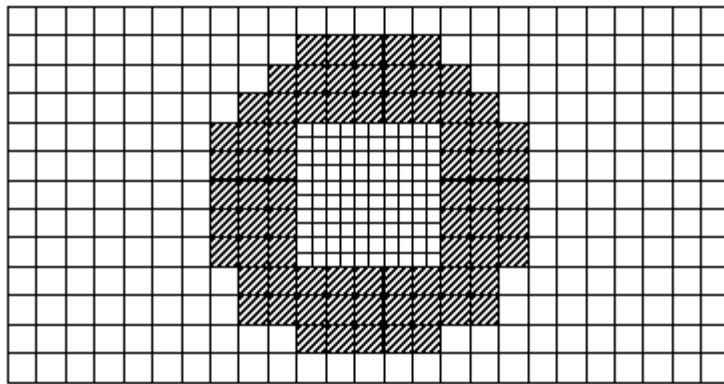
Figure 3-17: Structure of the calorimeter. The large scintillating glass blocks are marked.

All scintillating glass blocks had a depth of 89 cm, or 20.9 radiation lengths, while the lead glass blocks were 41.5 cm, or 16.8 radiation lengths deep. All blocks were read out by phototubes with individually adjustable voltages.

Calibration of the system was performed in two steps. Before the run, a selected number of blocks was exposed to particles of known energy at Brookhaven National Laboratory. During the run, the other blocks were normalized by comparing their response to high-energy muons to the response of the previously calibrated blocks. In addition, an LED system was used to monitor individual blocks and to correct for variations during the run.

The resolution of individual calorimeter blocks was determined in a test beam[58] to be

$$\delta E / E \approx 10\% + 10\% / \sqrt{E}$$ (3.1)

where E is the measured energy (in GeV). There were slight variations from block to block and between different periods of the run.

3.4.3 Muon ID walls

Since muons pass through matter more easily than other particles, a muon identification system can be constructed by placing particle detectors behind a generic shield of material of sufficient thickness.

There were two reasons to include a muon ID system in the experimental setup. The first is the necessity to identify primary muons. Hadronic reinteractions with the target material can produce tracks that mimic tau decays. If a lepton can be identified as one of the emulsion tracks coming from the primary vertex, the event can be classified as an electron or muon charged-current interaction, reducing possible background. The second reason is that ν_μ charged-current interactions can be used as an independent method to normalize the expected total interaction yield, as described in this thesis.

Muon identification is essential to this analysis because – as mentioned above – muons from light meson decays make up the bulk of the background events. Other than in the identification of muons in tau candidate events, the goal here is to only classify those tracks as muons that are identified unambiguously. For this reason hit multiplicity cuts were imposed on candidate tracks, and those parts of the muon ID system whose performance was questionable were not used.

The system consisted of three separate walls, called A, B and C. A 42 cm thick layer of steel in front of wall A and two 91 cm thick layers between the walls served to block other particles that were not fully absorbed in the calorimeter (see Figure 3-18).

Proportional tubes made up about 80% of the active area of the walls, and were arranged in two H-shaped planes, one horizontal and one vertical, to allow readout for

both x and y position. The planes were divided into several subsections with detectors of different lengths, as shown in Figure 3-19.

Each proportional tube had a cross section of 4 cm x 4 cm with a length varying from 1.3 m to 6.25 m depending on its position in the wall. They were operated using a 95% Ar / 5% CO_2 mixture. Inside them was a 60 μm sense wire spanning the whole length of the tube.

Plane	Scintillators	Prop. Tubes	Total
AX	112	264	376
AY	48	88	136
BX	96	232	328
BY	48	88	136
CX	96	232	328
CY	48	88	136
Sum	448	992	1440

Table 3-3: Detector systems used in muon ID walls.

Each four adjacent tubes formed a module, the principal building block of the walls. Each module had one four-channel amplifier/discriminator card reading out the current signal from the sense wires. In total, there were 248 proportional tube modules.

Because the proportional tubes had a resolving time of about 1 μsec, they were not suitable for the region of the muon "plume". These gaps in the coverage were filled with scintillator hodoscopes, which had a resolving time of only 15 ns. These were arranged in one vertical and one horizontal layer. Each of the scintillator elements had a width of 4 cm, matching the size of the proportional tubes, and a thickness of 1.5 cm. The vertical elements were 1 m, the horizontal elements 2.3 m long. Each element was wrapped individually in aluminum foil for optical isolation. Due to their poor performance, as demonstrated below, the scintillators were not used in the identification of muon tracks. The two systems combined covered an area of 6.25 m x 3.7 m for the upstream (A) wall, and 5.48 m x 3.25 m for the two remaining walls[59].
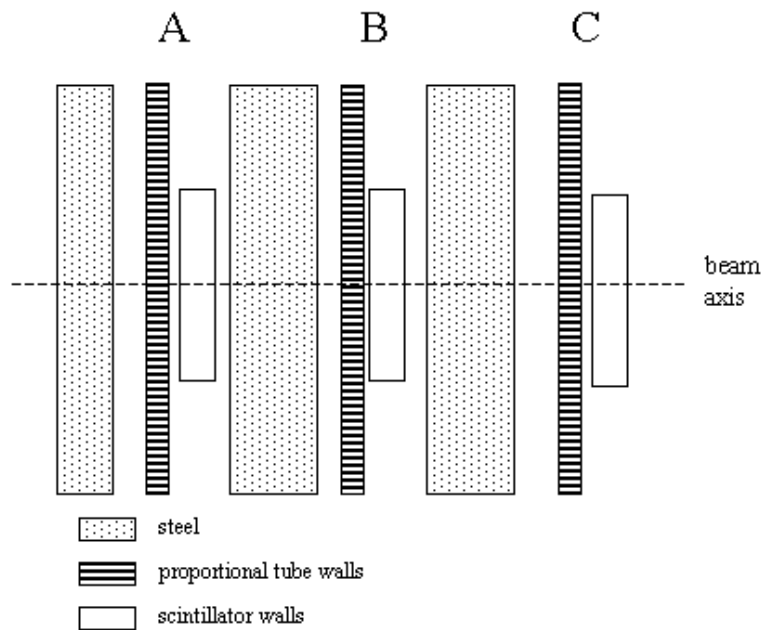
Figure 3-18: Sketch of the muon ID system.
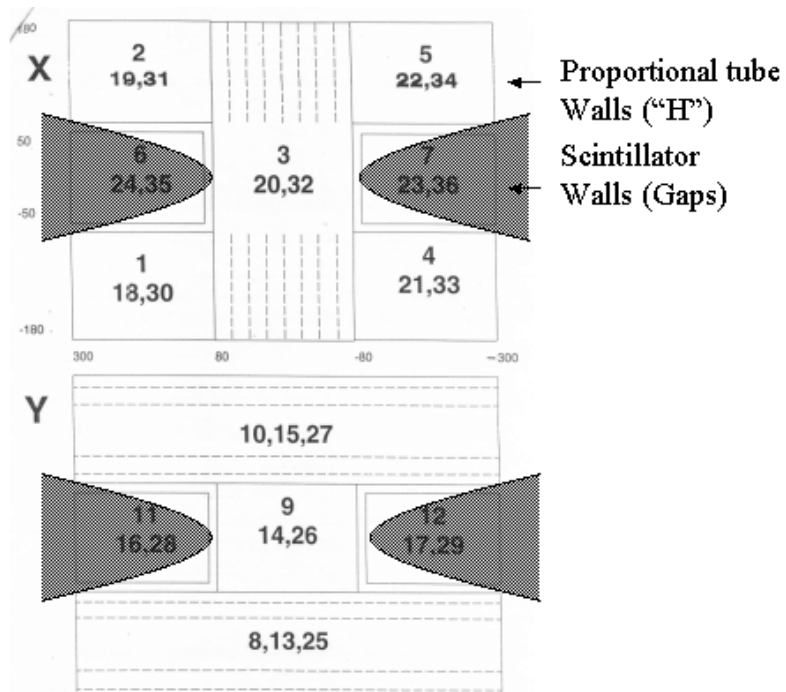
Figure 3-19: Muon ID wall x and y planes with plane numbers (wall A, B, C) as used in analysis code. The small numbers show spatial position in E872 coordinate system. The scintillator walls are placed in the gaps left by the proportional tube coverage.
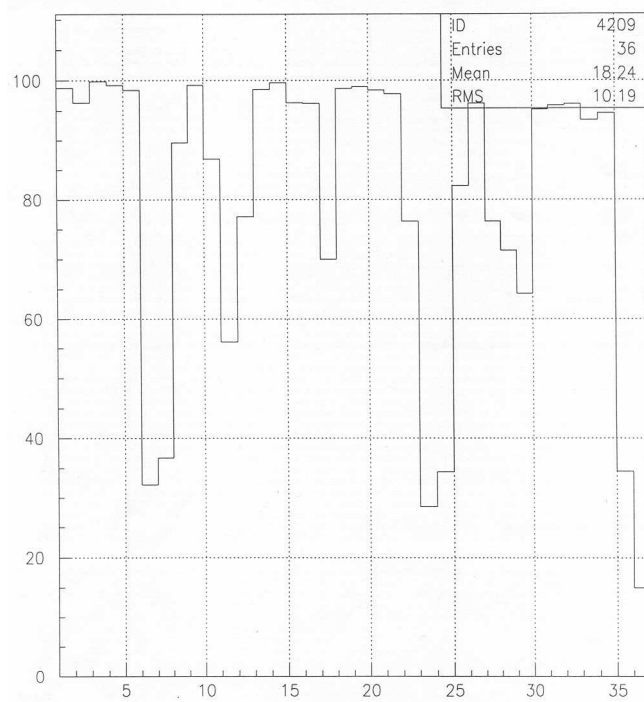
Figure 3-20: Muon Plane response in percent (no distance cut). For explanation of x-axis see Figure 3-19. The "dips" in the plot correspond to scintillator planes (Calibration data, single muon tracks).
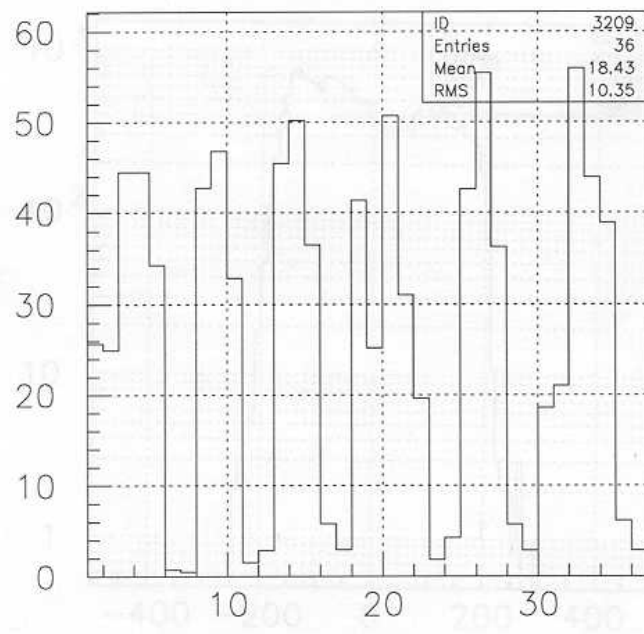
Figure 3-21: Hits associated with drift chamber tracks as percentage of total hits in plane. The "dips" in the plot correspond to scintillator walls (calibration data, single muon tracks).

41

A major problem of the muon ID system was the bad performance of the scintillator walls. Using data from a calibration run, drift chamber tracks were projected to the position of the muon ID walls and checked for hits in the corresponding planes.

Figure 3-20 shows the response of the muon ID planes. It should be noted that no distance cut was applied, and tracks were not required to have associated hits in all three walls. Therefore the value is related to, but does not represent, the actual efficiency. The plot shows that scintillator planes typically registered fewer than 80%, and sometimes even fewer than half, of the muons passing through.

The quantity in Figure 3-21 shows the hits associated with drift chamber tracks as a fraction of the total number of hits for the individual planes. This quantity is a measure for the number of random hits. Again, no strong cuts were applied. The extremely low value for some of the scintillator planes is caused by extensive crosstalk between the individual channels. The ratio of hits associated with actual muon tracks to total hits was in some cases as low as a few percent, compared to about 50% for the proportional tube walls.

Since the performance of the scintillators is considerably worse than that of the proportional tubes, as stated previously they were not used to tag muons in the analysis.

The actual efficiency of the proportional tubes was calculated by counting only adjacent muon ID hits within a distance of 10 cm. Tracks were required to have hits in 4 out of 6 possible planes with at least one hit in each of the three walls. Using the approximation that all individual tubes have the same efficiency η, the relative probabilities f_n for tracks with n muon ID hits are:

$$f_6 = \eta^6$$
$$f_5 = 6\eta^5(1-\eta) \tag{3.2..4}$$
$$f_4 = 12\eta^4(1-\eta)^2$$

The factor of 12 in the last expression, as opposed to 15 in the binomial distribution, comes from the requirement of having at least one hit in each muon ID wall.

Figure 3-22 shows the distribution of hits per track in calibration data and the best fit. The resulting value for the efficiency η is 93%.

The measured resolution of the muon ID system is shown in Figure 3-23.
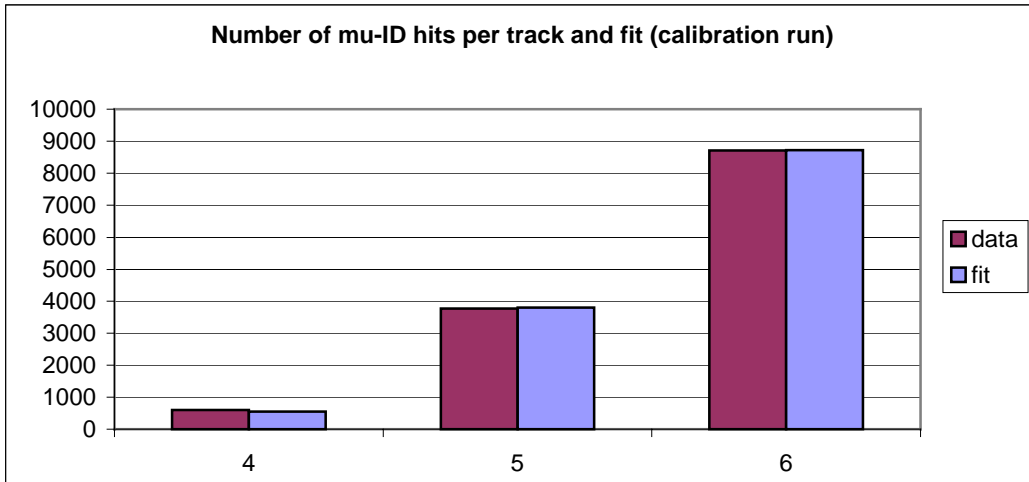
Figure 3-22: Number of muon ID hits per track; calibration data and fit to theoretical distribution.
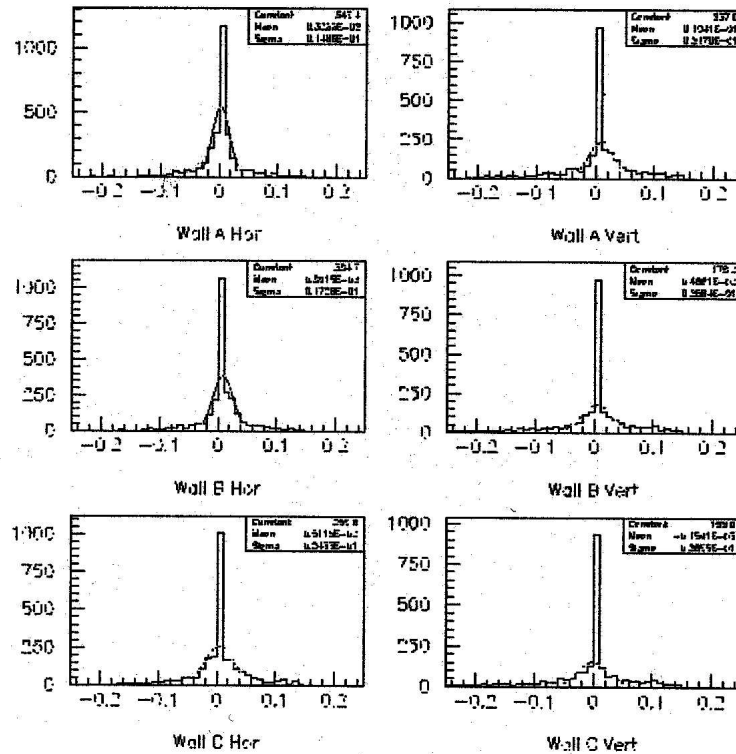
Figure 3-23: Measured muon ID resolution (calibration run, single muon tracks). X-axis in meters.

3.5 Trigger and DAQ

3.5.1 Trigger System

The veto wall, located in front of the target box, covered a total area of 140 cm x 152 cm and was composed of two layers of 5 scintillation counters each. The counters were read out on both ends by photomultiplier tubes. With a minimum ionizing particle detection efficiency of >95% for the individual counters, the total veto wall efficiency was better than 99%.

There were three separate trigger walls.

- T1 was made from bundles of scintillating fibers covering an area of 70 cm x 70 cm. It had eight segments and was located between the second and the third emulsion module. Each segment was individually read out by a phototube.

- T2 was placed downstream of the last emulsion module. It was identical to T1 except that it had nine segments and covered an area of 80 cm x 80 cm.

- T3 was located downstream of the fiber/emulsion system and consisted of 8 plastic scintillator paddles 10cm x 80cm in dimension. They were read out via lightguides 49 cm long attached to both ends connecting them to two phototubes.

Each of the trigger counters had an efficiency of better than 97% for minimum ionizing particles[41]. Triggering on physics events was done by requiring hits in adjacent segments of (T1.and.T2) or (T2.and.T3). Figure 3-24 shows the trigger logic.

The trigger system was designed for a trigger rate of ≈5Hz. In combination with a readout time of 24ms - dominated by the fiber tracking system - this resulted in a deadtime of less than 10%.

It should be noted that the actual rate of neutrino events was of the order of a few millihertz. Most triggers were caused by charged particles entering the target volume from the side. Their main source was interactions of background muons with the surrounding material, as illustrated in Figure 3-25.
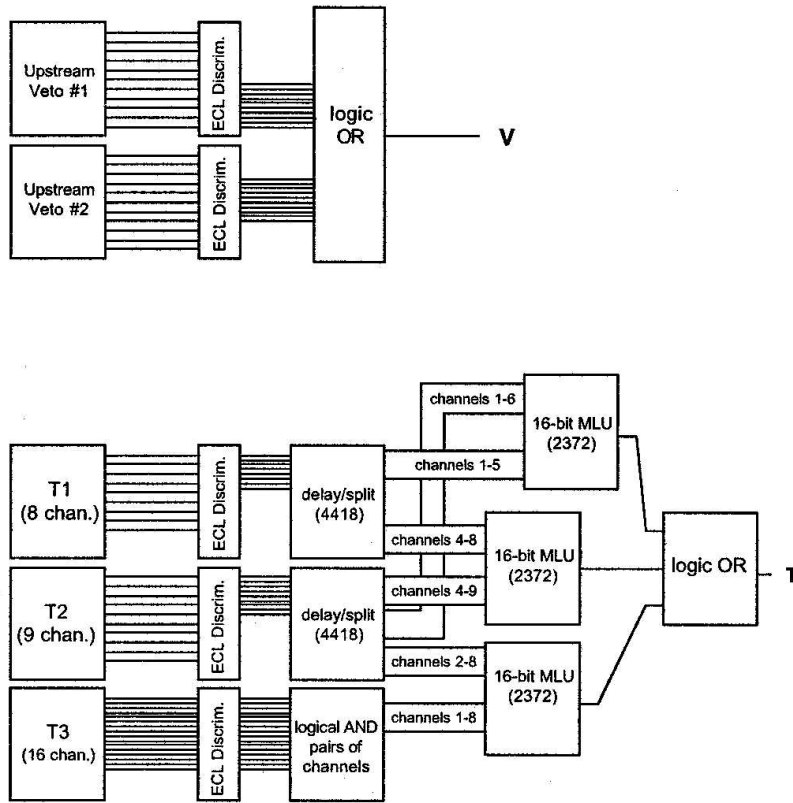
Figure 3-24: E872 Trigger Logic.
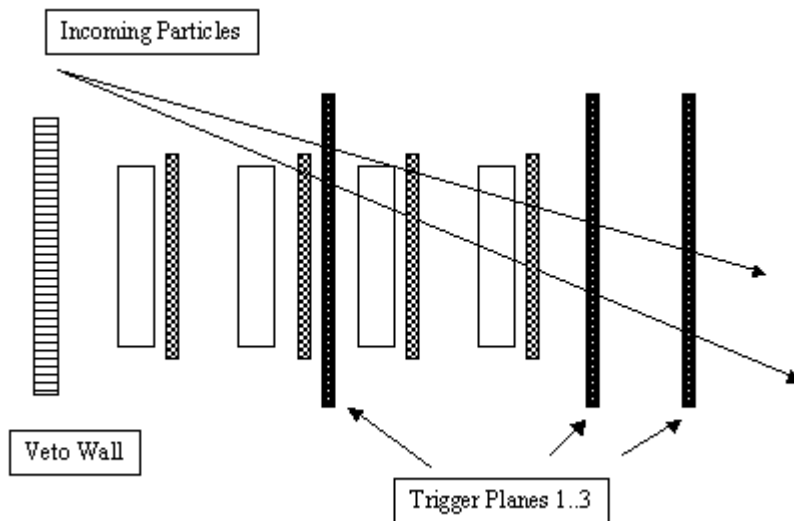
Figure 3-25: Example of background trigger event. A reduction of this type of event was achieved with the shielding modification shown in Figure 3-2. For a discussion of shielding issues see Section 3.2.

3.5.2 Data Acquisition

The E872 DAQ system used an implementation of Fermilab DART[60] architecture hardware and software. Electronic signals coming from detector elements were digitized using standard CAMAC ADCs and TDCs. Online monitoring and data storage to tape were done by a workstation connected through a TCP/IP network with a typical speed of 500-600 KB/sec to the VME processor that gathered information from the various modules. Additional details of the Data Acquisition system are described in Section 4.2.

4 Event selection

4.1 Overview

As mentioned previously, the raw event rate exceeded the rate of neutrino interactions by several orders of magnitude. This chapter will give an overview of the various steps that reduced the recorded data set to a real neutrino event sample.

Data acquisition process was done in four periods distinguished by different emulsion target configurations. Table 4-1 gives an overview of integrated exposure and target configuration for these individual periods.

Period	Protons on Target	Station 1	Station 2	Station 3	Station 4
1	5.40×10^{16}	ECC1	-	ECC3	-
2	4.40×10^{16}				ECC/Bulk4
3	1.03×10^{17}		ECC/Bulk2	ECC/Bulk3	
4	1.55×10^{17}	ECC/Bulk1			Bulk4

Table 4-1: Target configurations and exposure for all run periods.

Data was reduced by the following steps:

- The hardware trigger system, as described in Section 3.5.1.
- A set of computer routines for electronic event preselection, or "stripping".
- Scanning of the electronic event display by eye and selection of likely neutrino interaction candidates.
- Selection of events for attempted vertex location in the emulsion.
- Actual emulsion analysis and event topology reconstruction.

For the purpose of this thesis, muon events with electronically reconstructed vertices were selected separately. The goal for this was to obtain as clean an event sample as possible.

Sections 1-4 of this chapter contain a description of the general event selection process that lead to the identification of the four tau neutrino events. Section 5

describes the selection of muon charged-current events, done solely for the purpose of this thesis.

4.2 Hardware Event Selection

Hardware event triggering was accomplished by adjacency requirements in the trigger wall hodoscopes. An illustration of this principle is shown in Figure 4-1. During the first half of the run, a trigger (T1) required at least one double adjacency between two planes and one or more hits in the last plane. This condition was later modified to facilitate the detection of elastic interactions. An alternate acceptable trigger condition (T2) was introduced, requiring only a single adjacency, but in addition requiring at least one hit consistent with a minimum ionizing particle in the central part of the electromagnetic calorimeter.

The trigger rate at full beam intensity (8×10^{12} protons per spill) was $\approx$3 Hz for T1 triggers. For T1.or.T2 it increased to $\approx$4 Hz. The total deadtime for the latter was 13%[61].

An entirely different trigger condition was used for calibration runs. The beamline setup provided the opportunity to direct the proton beam at a target (PW5) about 200 m upstream of the tungsten beam dump. In this mode large quantities of muons were produced through light-meson decays. Provided that their energy was high enough, these muons penetrated the passive shielding system and could be used for calibration and alignment of the electronic detector systems. In this case the trigger condition required one hit each in the upstream veto wall and in trigger planes one and three.

The electronic information was transferred through an Ethernet link to a workstation, where it was stored on magnetic tapes in the standard Fermilab DART[60] format. The size of the individual neutrino events varied from <100 KB to >1 MB depending on hit multiplicity. Background events typically were smaller by about one order of magnitude, so the maximum data transfer rate was approximately 15 MB per proton spill, or 500-600 KB/sec.
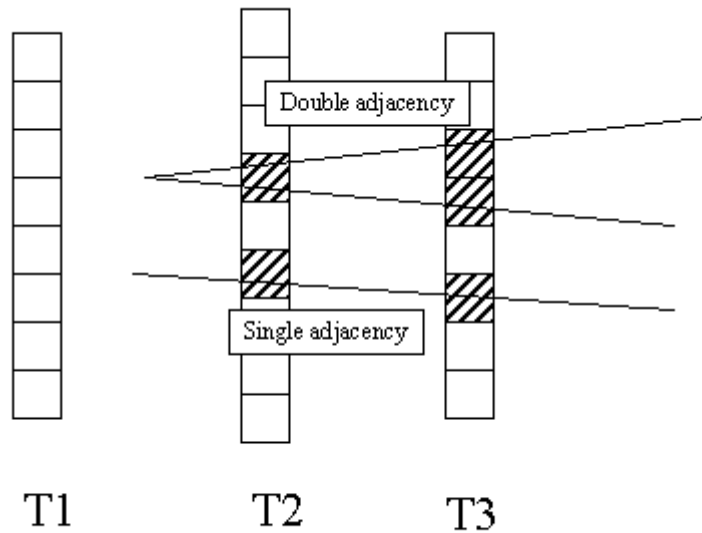
Figure 4-1: Examples of trigger hodoscope adjacencies.

4.3 Stripping

Completed data tapes were analyzed on the Fermilab UNIX cluster; Figure 4-2 shows a flow chart of the procedure[62]. The functions of the four passes used were:

- pass1: Filter out obvious background events (no visible spectrometer tracks).

- pass2: Keep events fulfilling one of three conditions:

    o One or more drift chamber tracks pointed within 0.5 m of the most downstream emulsion module.

    o A vertex was reconstructed from one scintillating fiber view.

    o The calorimeter contained   30 GeV of visible energy.

- pass3: Create interspill events (needed for calibration).

- pass4: Generate calibration histograms.

In total, 325 data tapes were recorded, each with a typical processing time of ≈ 15 hours. This procedure reduced the total number of events from $\approx 10^7$ to $\approx 10^5$.

Remaining events were visually scanned by a team of two physicists. Each of the two first scanned the events by himself; once a pass was completed, results were compared and discrepancies reconciled. The criteria for event selection required that:

- There had to be a reconstructed vertex from scintillating fiber information having three or more high-energy tracks or a particle shower. The location of this vertex had to be within an emulsion module.

- The total event energy (from reconstructed spectrometer tracks and calorimeter) had to be greater than 5 GeV.

Both requirements were designed to reject low-energy background events like the one shown in Figure 3-25. The 902 events surviving this pass were submitted to Nagoya University for emulsion analysis. For the events that were selected as likely neutrino interactions, a vertex location prediction was made using electronic information. Four different routines were used in combination for this purpose. The accuracy for this vertex prediction, estimated using located events, is about ±0.5 cm in the transverse (u,v) and ±5 cm in the longitudinal (z) direction[63].

The overall efficiency of the scanning procedures has been estimated by a Monte Carlo study[64]. It was found that the stripping efficiency depends on the number of visible tracks in the scintillating fiber system (see Figure 4-5). The typical efficiency for charged-current events is about two thirds, and is slightly lower for neutral-current events.
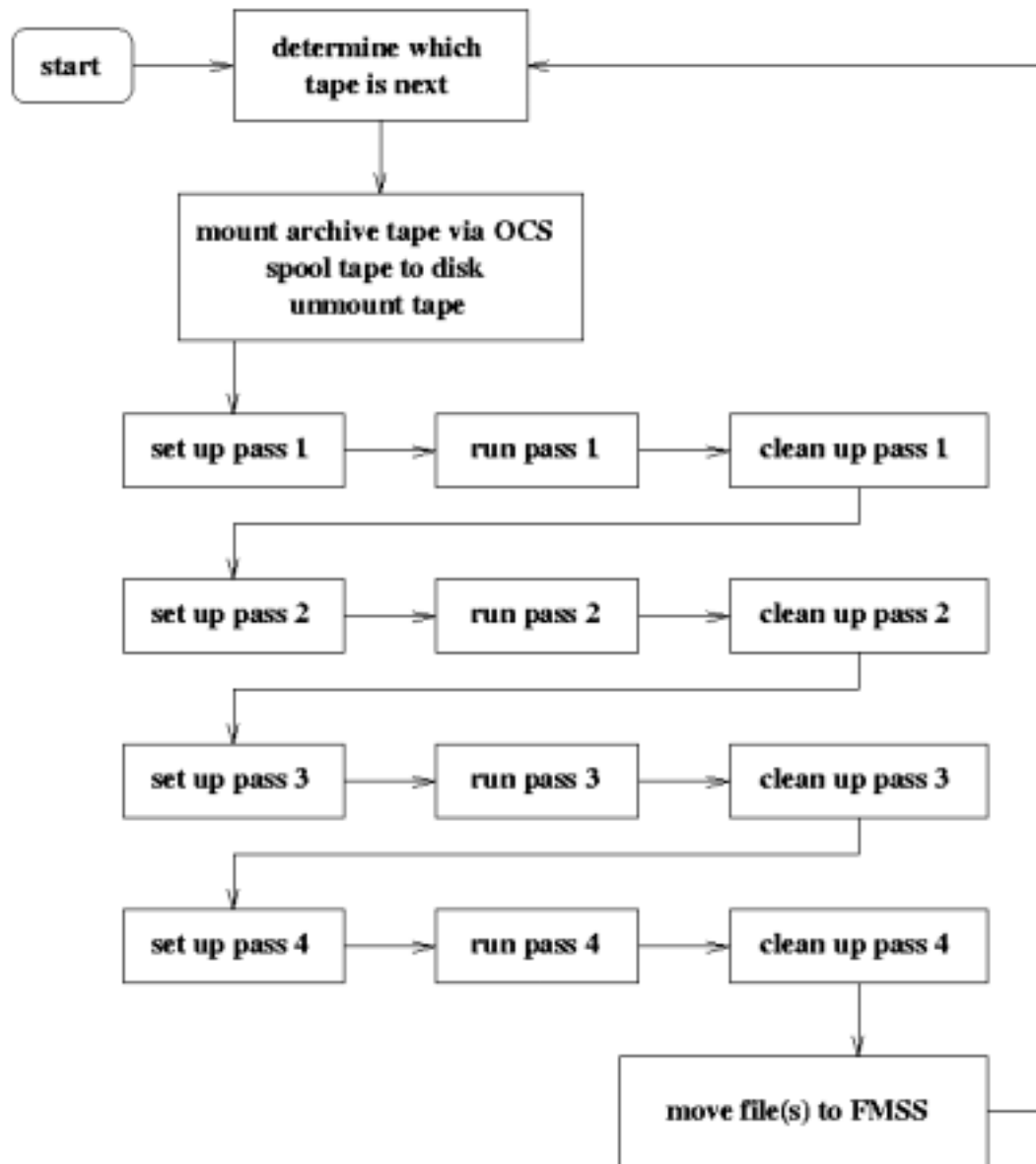
Figure 4-2: Flow chart of the electronic stripping procedure.

4.4 Emulsion Scanning

All emulsion processing, scanning and measurement was done at Nagoya University. Table 4-2 shows the total exposure and mass for each emulsion type. The number of interactions in a given module is expected to be proportional to its mass and to the number of protons on target during the time it was installed.

Module	Total Exposure [pot]	Mass [kg]	Mass*Exposure [fraction of total]
ECC1	2.01×10^{17}	100.49	21.7%
ECC3	9.8×10^{16}	100.49	10.6%
E/B1 (ECC part)	1.55×10^{17}	49.15	8.2%
E/B2 (ECC part)	2.58×10^{17}	42.12	11.6%
E/B3 (ECC part)	2.58×10^{17}	44.46	12.3%
E/B4 (ECC part)	1.47×10^{17}	36.71	5.8%
Total ECC			70.2%
E/B1 (bulk part)	1.55×10^{17}	19.35	3.2%
E/B2 (bulk part)	2.58×10^{17}	25.15	7.0%
E/B3 (bulk part)	2.58×10^{17}	21.28	5.9%
E/B4 (bulk part)	1.47×10^{17}	27.73	4.4%
Bulk4	1.55×10^{17}	56.10	9.3%
Total Bulk			29.8%

Table 4-2: Exposure and mass for different emulsion module types.

Two additional cuts were imposed on events prior to emulsion analysis. The first was a fiducial volume cut, eliminating vertices predicted to be in regions with high muon flux. High track density in those regions would have made the analysis extremely difficult. The region that was designated as fiducial volume varied with the individual emulsion module.

The second cut was based on the number of visible particle tracks originating from the vertex. Events with low multiplicities were eliminated because they were too hard to locate. These additional cuts reduced the number of events selected for emulsion scanning from 901 to 511.

Two methods were used to scan emulsion. The first relied on changeable sheets (CS Scan). In this method, additional emulsion sheets were located in front of and behind each emulsion module. These sheets were replaced frequently, and therefore had a much lower track density than the emulsion modules themselves. The success with this method was only moderate, especially for events with high particle multiplicities.

The second method required digital scanning of the entire volume around the predicted vertex location (Net Scan). In this case, events with high track multiplicities are favored. Figure 4-3 shows a flow chart of the procedure. The requirements for located vertices using this method are:

- three or more tracks originating from the vertex with momentum >100 MeV (estimated from amount of multiple scattering).

- all tracks within <4 μm at closest approach (impact parameter, IP).
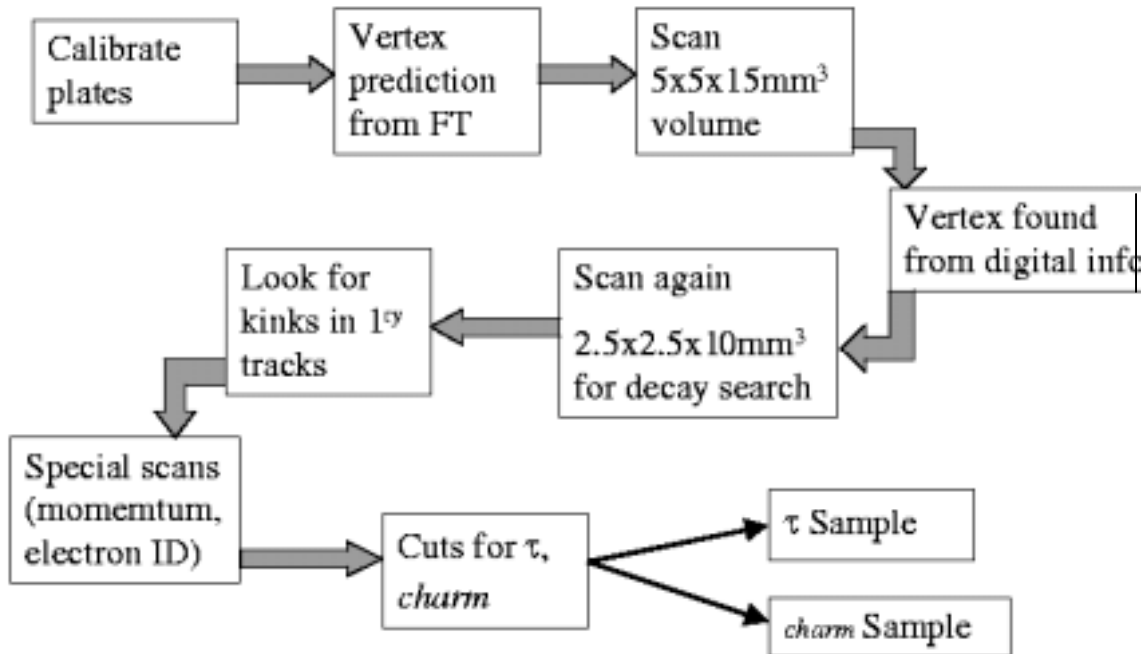
Figure 4-3: Flow chart of the emulsion scanning procedure (FT: Fiber Tracker).

These requirements provided an efficient method to distinguish tracks originating at the primary vertex from randomly associated background tracks. An illustration of this is given in Figure 4-4.
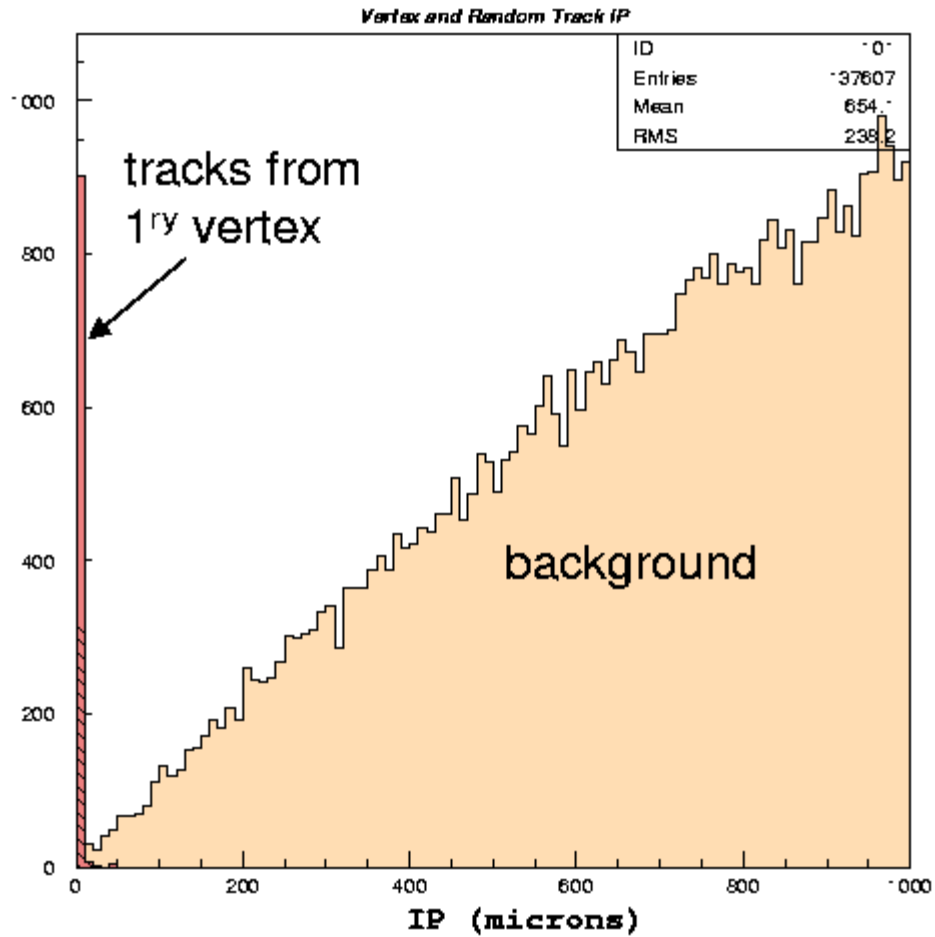
Figure 4-4: Primary vertex tracks and random association in dependence of impact parameter (IP)

Once the primary vertex was located, all tracks were followed downstream. The spatial resolution of the emulsion was found to be 0.3 μm[65] and the angular resolution, where applicable, $\approx$1.5 mrad[66].

The location efficiency depended on the type of module and the z-position of the predicted vertex within the individual modules. Table 4-3 shows all vertex location efficiencies for the three module types[67].

Module Type	Vertex location efficiency
Bulk	78%
ECC 200	62%
ECC 800	48%

Table 4-3: Vertex location efficiency for emulsion module types.

Another useful way to determine location efficiency statistically is to compare the primary track multiplicity for located and simulated events. As mentioned above, the Net Scan method of emulsion analysis favored events with higher track multiplicities and events with fewer than 3 primary tracks could only be located by the less efficient CS Scan method. The result is a significant reduction of the location efficiency for low-multiplicity events. Figure 4-5 shows the result for all located events compared to a LEPTO Monte Carlo distribution[68].
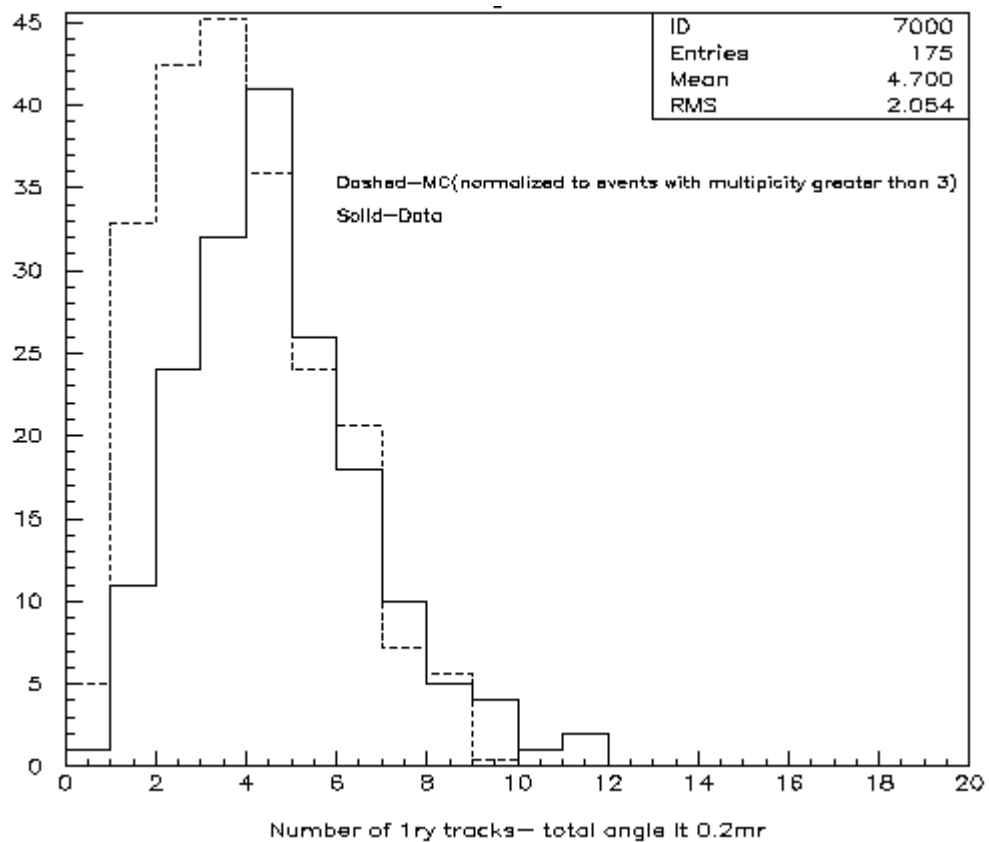
Figure 4-5: Track multiplicity for located events and LEPTO Monte Carlo (normalized).

The number of events after each of the analysis steps is given in Table 4-4. A description of further emulsion analysis and a discussion of kink search results is given in ([69]).

Cut	Number of events
Hardware Triggering	6.6×10^6
Automated Stripping	$\approx 10,000$
Electronic Vertex Prediction	901
Inside Fiducial Volume	699
Emulsion Data Exists	511
Located Vertex	261
Complete Emulsion Information	203

Table 4-4: Number of events after cuts (as of January 2001).

4.5 Tau Events

Figure 4-6 shows the four tau CC events and their event parameters. The decay kink is clearly visible in each picture. Each dot along the tracks represents an emulsion measurement. The primary tau track has been directly located in all cases. For a comprehensive discussion of individual events see ([70]).

Individual event probabilities were calculated using five parameters related to the event topology (decay length, kink angle, daughter momentum, primary angle, angle of lepton vs. sum of all other charged tracks)[71]. While there is no final result yet, preliminary values indicate that event 3263_25102 has a substantial chance of being a secondary interaction. The other three events are solidly identified as tau decays, with probabilities around 90% or higher.
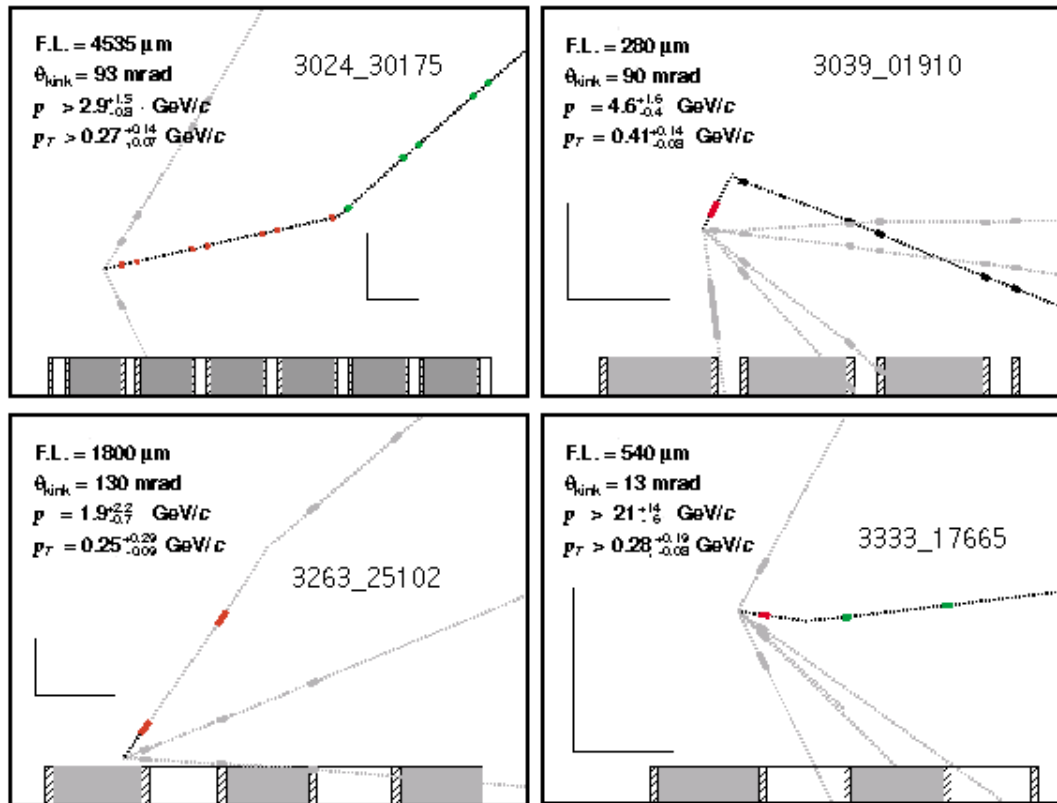
Figure 4-6: The four tau neutrino charged current events. The scale is given by the perpendicular lines (vertical: 0.1 mm, horizontal: 1 mm). The bar on the bottom shows the target material (solid: steel, hatched: emulsion, clear: plastic base).

4.6 Muon Event Selection

4.6.1 Introduction

As mentioned in Section 1.3, for the purpose of this thesis, muon events were identified in the electronic sample. Using downstream drift chamber, muon-ID system and vertex position information, tracks were reconstructed and their momenta were calculated.

For the calorimeter energy spectrum analysis, all located events were used and no additional cuts had to be imposed. However, in order to obtain a clean muon charged-current interaction sample, the muon track had to be reconstructed to provide an unambiguous identification of the event type. All procedures detailed in this section, as opposed to the ones in the previous sections of this chapter, were done exclusively

for the purpose of this thesis. The following is a description of the procedure used to extract muon events used in the analysis.

The original event sample was the 511 events selected at Nagoya University for attempted location in the emulsion. Of these, 261 events had a located primary vertex and 203 had complete emulsion information. Vertices for events not located in the emulsion were reconstructed electronically using the E872 offline analysis code.

4.6.2 Track Reconstruction

In order to identify muon CC interactions, a track reconstruction algorithm was used to find tracks in the downstream drift chambers and check for correlated hits in the muon ID walls. Because of high hit multiplicity upstream of the analyzing magnet, no information from the vector drift chambers or the scintillating fiber system was used. Instead, the bend angle of the track in the analysis magnet was calculated using a track downstream of the magnet together with the vertex position itself, as shown in Figure 4-7. An estimate for the bend angle error and the resulting error on the track momentum is given in Appendix A.
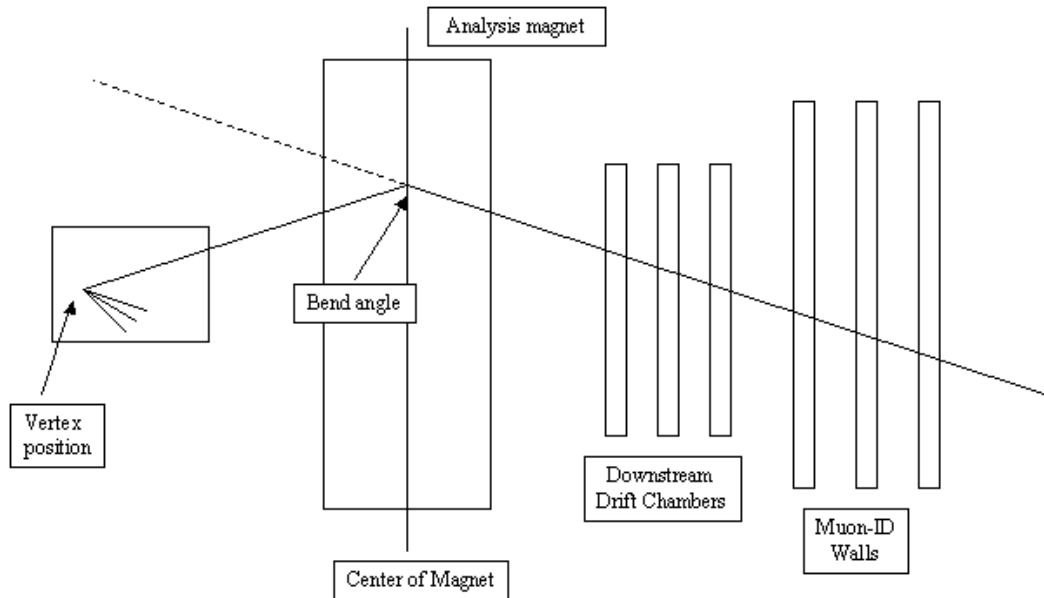
Figure 4-7: Systems used in reconstruction of muon tracks.

Drift chamber tracks were found by reconstructing lines in the x view and then looking for intersecting hits in the u and v views in order to get spatial tracks. The

58

requirement for an x view line was to have at least one hit in one of the x planes of each of the three drift chambers or hits in both x planes of two drift chambers. A drift chamber track also required three additional hits in the u and/or v views. If no muon candidate track was found in the event, the search was extended to tracks with only two u or v hits. Only tracks with a slope of less than 400 mrad with respect to the beam axis were allowed. Figure 4-8 and Figure 4-9 show the distribution of χ^2 per degree of freedom (*dof*) for DC lines (x-view) and tracks (3D) as well as theoretical curves for different numbers of drift chamber hits *n*. Both data distributions agree with expectation at low values of χ^2/dof but indicate a large background from hit ambiguities and random hit alignment at higher values. For both *x* lines and complete spatial tracks a cut of $\dfrac{\chi^2}{dof} < 5$ was used.
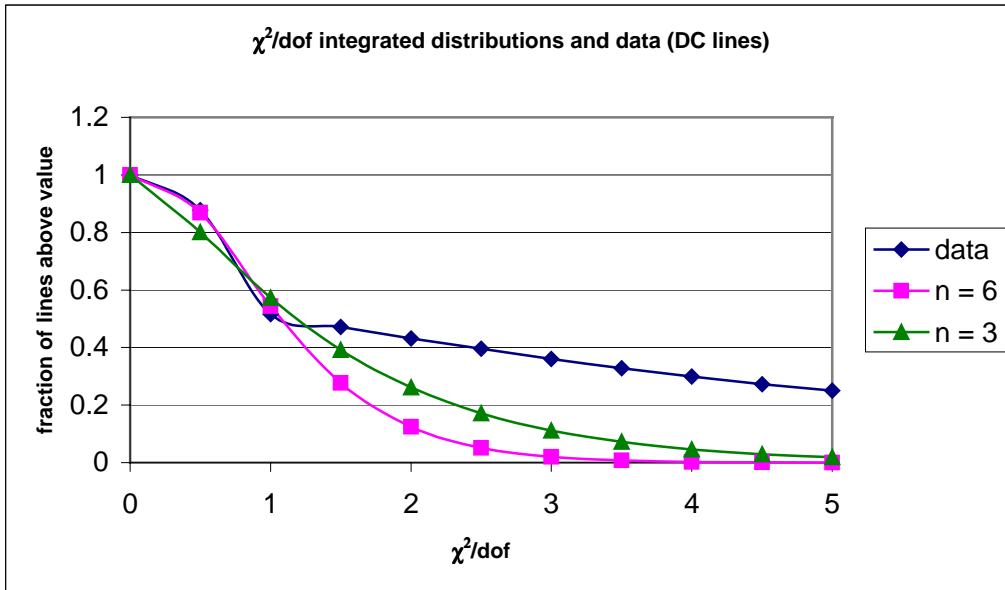
Figure 4-8: χ^2/dof-distribution for downstream drift chamber (x-view) lines. The parameter n indicates the degrees of freedom in the theoretical distribution.
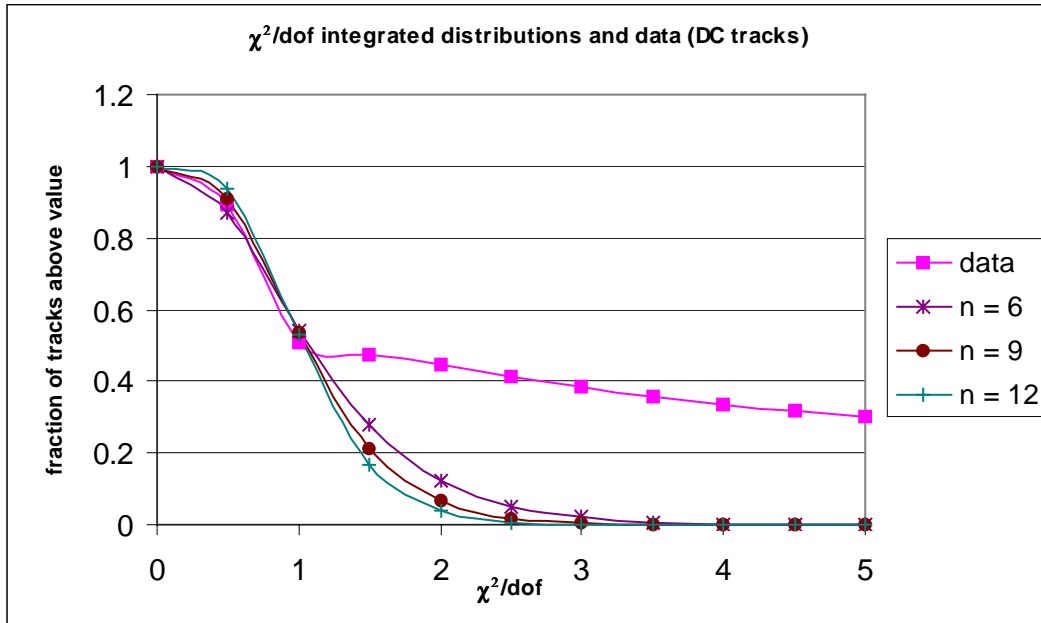
Figure 4-9: χ^2/dof distribution for downstream drift chamber (3-dimensional) tracks. The parameter n indicates the degrees of freedom in the theoretical distribution.

4.6.3 Muon Identification

Drift chamber tracks were projected to the position of each muon ID wall and checked for adjacent hits within 10 cm of the track. A muon track was required to have 4 or more associated hits out of 6 possible, with at least one hit in each of the three muon-ID walls. Figure 4-10 shows the hit multiplicity distribution for data events, compared to a fit to the calibration data from Section 3.4.3. The two shapes are in reasonable agreement, consistent with little background from random associations.
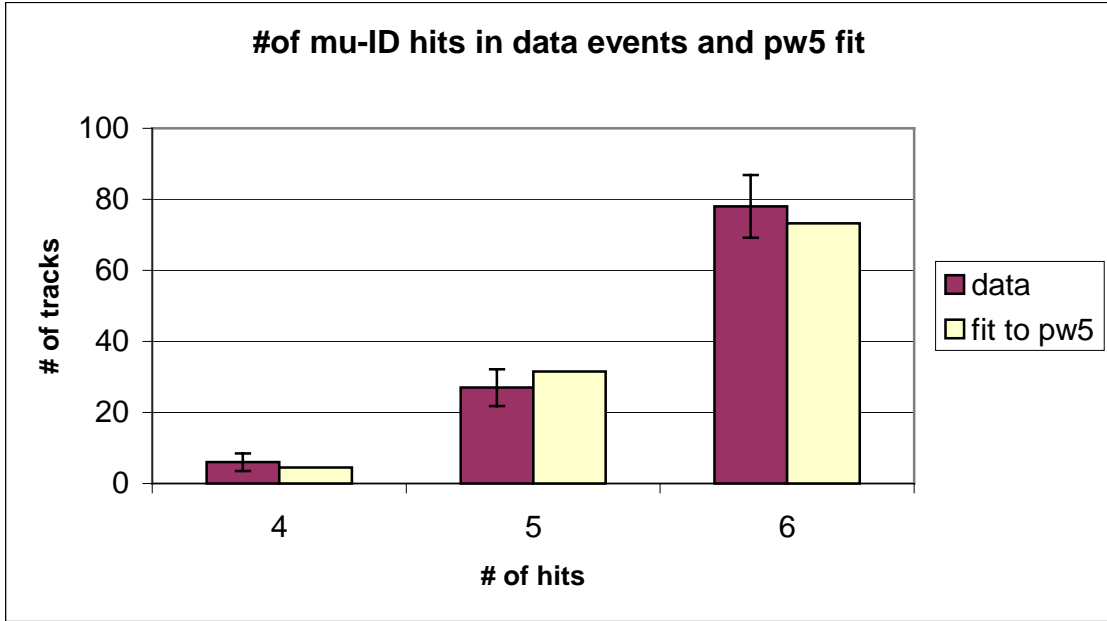
Figure 4-10: Muon ID wall efficiency in data events.

4.6.4 Electronic Cuts

Once a muon candidate track was found, it was refit using all drift chamber and muon ID hits. Because of the high value of σ (8cm) for the muon walls, the final track was essentially the same as the original drift chamber track.

The following additional cuts were imposed on the final tracks in the offline analysis code:

- $\dfrac{\chi^2}{dof} < 2$ (see Figure 4-11, Figure 4-12).

- An impact parameter of < 2.5 cm at the vertex position in the y (non-bend) plane (see Figure 4-13, Figure 4-14).

- Track momentum >5 GeV/c.
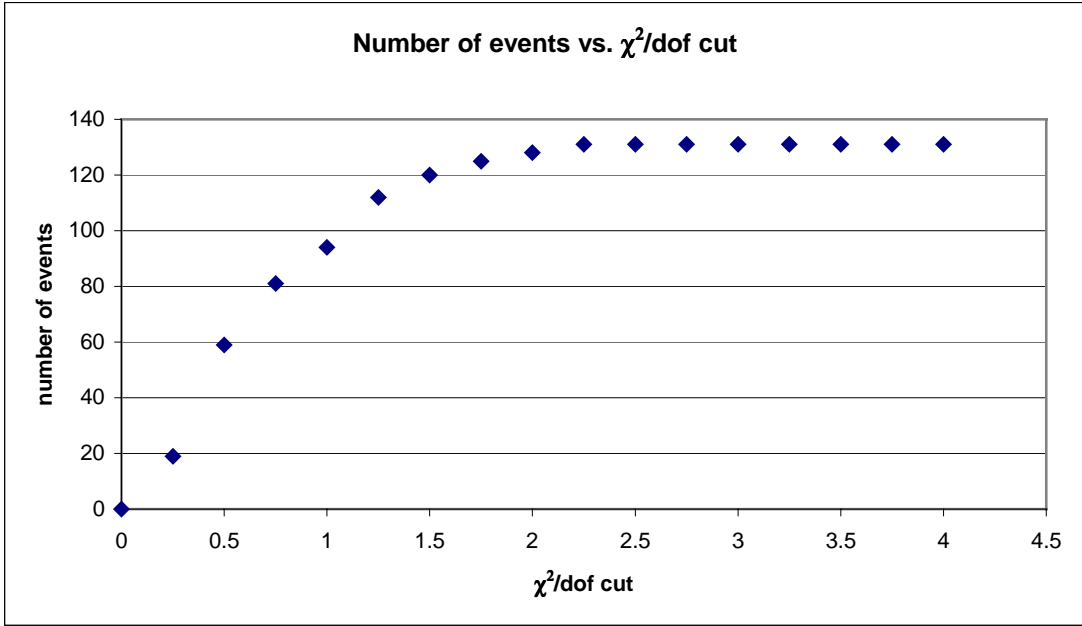
Figure 4-11: Effect of χ^2/dof cut on number of selected events.
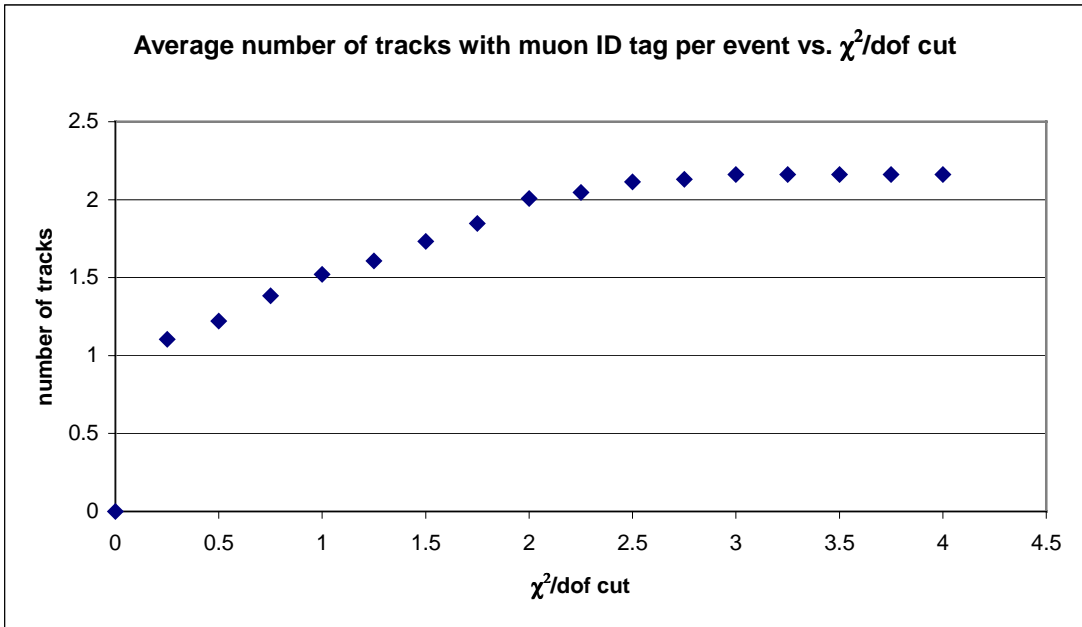
Figure 4-12: Effect of χ^2/dof cut on track ambiguity.
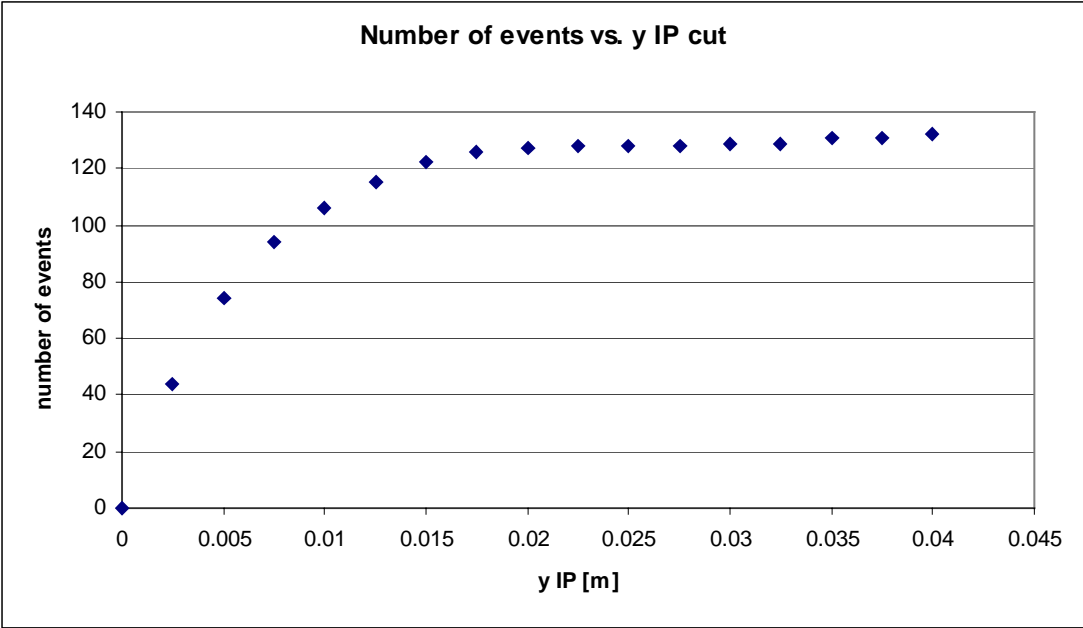
Figure 4-13: Effect of y impact parameter cut on number of selected events.
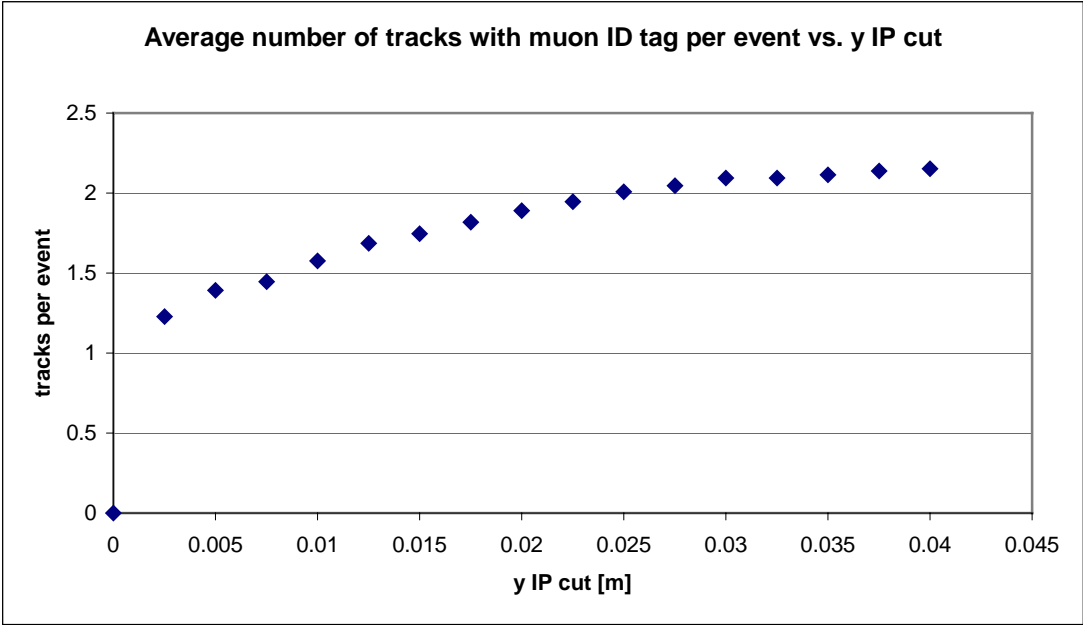
Figure 4-14: Effect of y impact parameter cut on track ambiguity.

4.6.5 Additional Cuts

The remaining candidate tracks were visually scanned and possible background events were removed. The criteria for removal were:

- Multiple adjacent muon candidate tracks with irreconcilably different momentum values ($|\frac{1}{p_1} - \frac{1}{p_2}| > .02$).

- >3 DC tracks within 3 cm distance and >25 DC tracks within 20 cm (isolation cut).

An overview of the effects of cuts on final muon tracks is given in Table 4-5. In many cases there still remained several spatially clustered muon candidate tracks for each event (see multiplicity plots Figure 4-12, Figure 4-14). In that case the final muon momentum was calculated using the average of the individual values weighted by the tracks' χ^2.

Table 4-6 summarizes all cuts imposed on muon tracks.

Cut	Events removed	Remaining events
Original Sample from offline analysis code		**134**
Irreconcilable momentum values	1	133
Isolation cut	5	128
Final Sample used in fit		**128**

Table 4-5: Effect of additional cuts on muon event sample.

Parameter	Cut
DC x-view lines, χ^2 / dof	5
DC 3-dimensional tracks, χ^2 / dof	5
Distance to vertex in y-view	2.5 cm
Number of muon-ID hits[*]	4, 1 in each wall, ≤ 10 cm distance
Final track χ^2 / dof	≤ 2
Track momentum	5 GeV
Different p values in same event	$\|\dfrac{1}{p_1} - \dfrac{1}{p_2}\| \leq .02$
Isolation cut	≤ 3 DC tracks within 3 cm distance or ≤ 25 DC tracks within 20 cm

Table 4-6: Summary of cuts on muon tracks.

4.6.6 Additional Checks on Muon Events

In order to ensure that there are no inadvertent biases in muon event selection, several additional checks were performed. A good opportunity to confirm the quality of the track fit is presented by the KSY chamber. The inclusion of hits in this system is not legitimate on a general basis because data is only available for a fraction of the events. However, it can be used to check for any mistakes in the fitting procedure. The closest approach of the reconstructed track to the vertex position was calculated with and without the inclusion of KSY hits in the fit. With the use of this additional information more data points are available for track fitting, and one expects the fit quality to improve. Consequently, in most cases the distance between vertex and track

---

[*] Only proportional tube planes were used (see Section 3.4.3)

should decrease. Figure 4-15 shows that this is indeed the case for the majority of events, confirming the validity of the fitting procedure.

It is also possible to check for any biases in the muon event selection by comparing the vertex location of tagged muon events to the overall distribution. Figure 4-16 shows the position of electronically-predicted vertices in the directions perpendicular to the beam axis. The radial distribution of the vertex locations is shown in Figure 4-17. No significant difference between the two distributions can be seen.

Figure 4-18 shows the distribution of events with respect to the emulsion module that contains the primary vertex. The value labeled "expectation" corresponds to the fraction of events projected to be in each module, as shown in Table 4-2. Again, the there is reasonable agreement between the individual distributions.
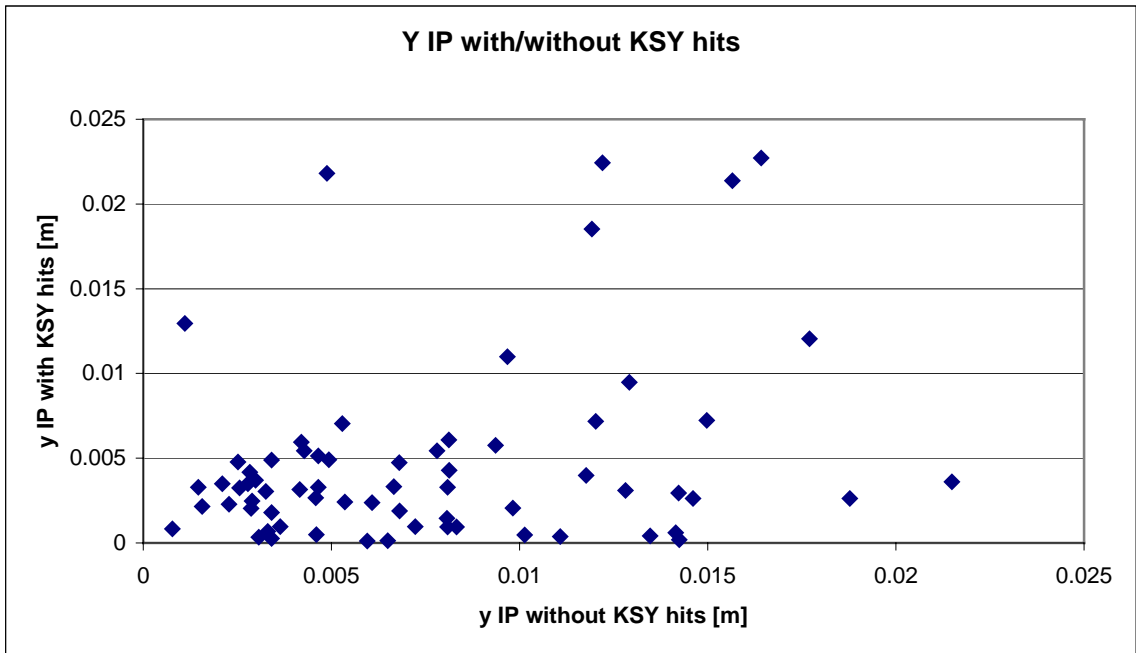
Figure 4-15: Closest approach of the reconstructed muon track to the vertex position in the y view (KSY check).

Predicted vertex position
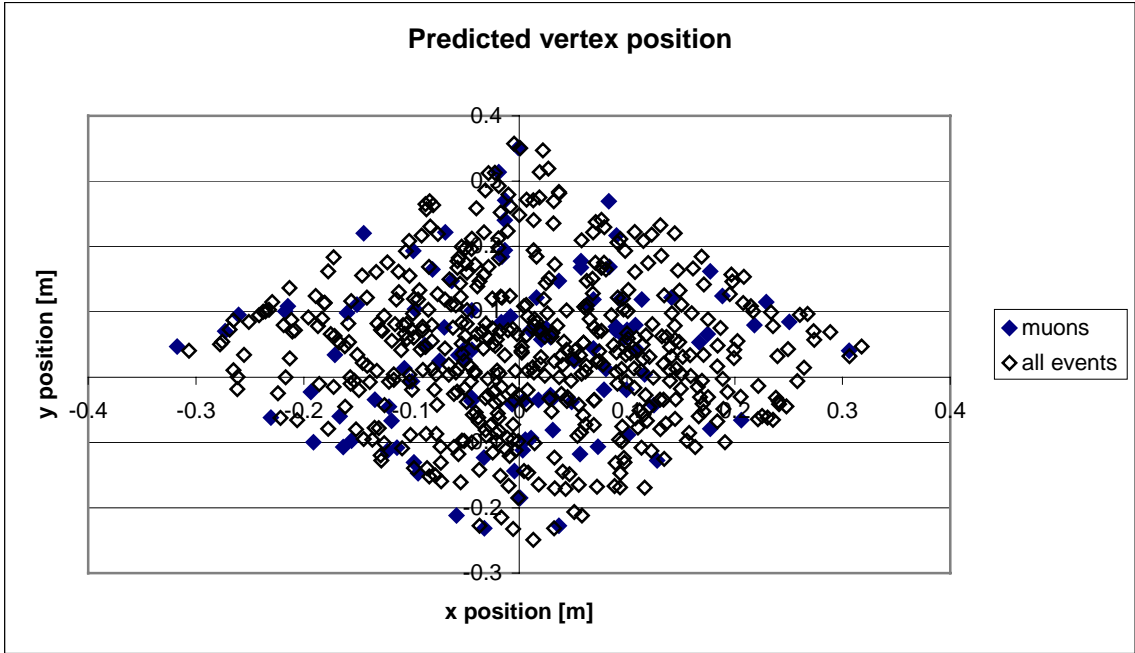
Figure 4-16: Electronically predicted vertex position in the emulsion for muon events and for overall sample.

Radial vertex distribution
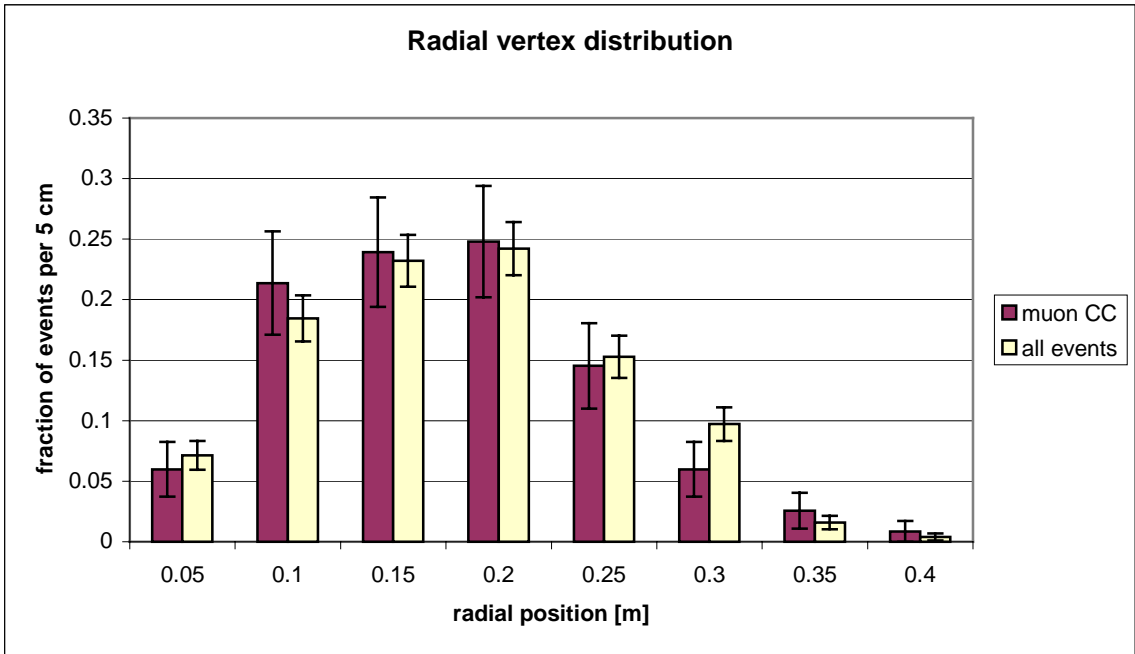
Figure 4-17: Electronically predicted vertex position as function of distance to beam axis.
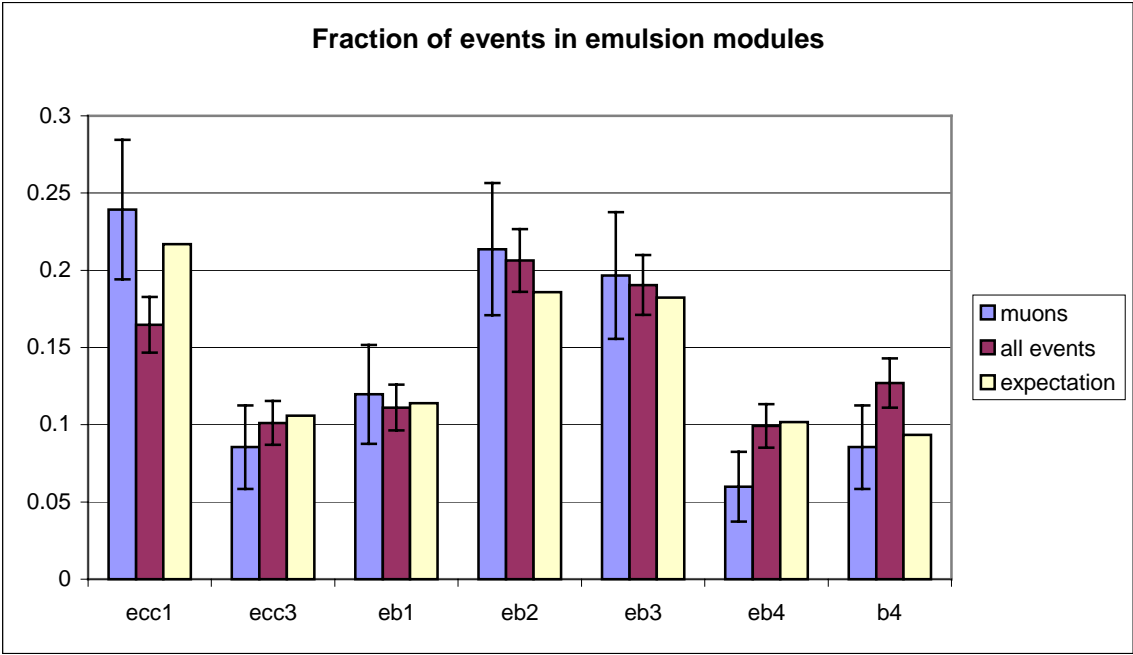
Figure 4-18: Distribution of events by module.

5 Phenomenology and Simulation

5.1 Introduction

Investigating beam composition required accurate simulation of each of its individual components. The purpose of this was to account for several efficiencies relating to event selection and reconstruction. The two spectra generated in the simulation were the muon track momentum distribution and the energy distribution in the calorimeter. Energy spectrum simulation was performed for all types of events, since no particular selection was done for the sample used in the final fit. The muon momentum spectrum was divided into two components, "prompt" for the neutrinos from charm decays, and "nonprompt" for background muon neutrinos from light mesons.

A hit level Monte Carlo program was used to generate observable spectra. Hits of charged particles were simulated for each individual detector system according to its sensitivity and resolution.

The processes relevant for understanding the experiment are:

- Production of heavy quarks, especially charmed mesons, in interactions of the proton beam with the target nuclei: $p + N \rightarrow D + X$.

- The subsequent semileptonic and leptonic decays: $D \rightarrow \nu_l X$.

- The decay of tau leptons: $\tau \rightarrow \nu_\tau X$.

- The interactions of neutrinos with matter in the emulsion target: $\nu + N \rightarrow X$.

The Monte Carlo simulation can be divided into three separate parts:

- Generation of neutrinos in the beam dump.

- Neutrino interactions in the target material.

- Tracking of charged daughter particles through the apparatus.

In generating tau neutrinos several different channels have to be simulated:

- Primary charm decay (D mesons and Λ_c baryons).

- Decay of light mesons (π, K) not reinteracted in the material.

- Decay of secondary charm produced by reinteractions of light mesons.
- Tau lepton decay.

Figure 5-1 shows a sketch of the various types of neutrino production.
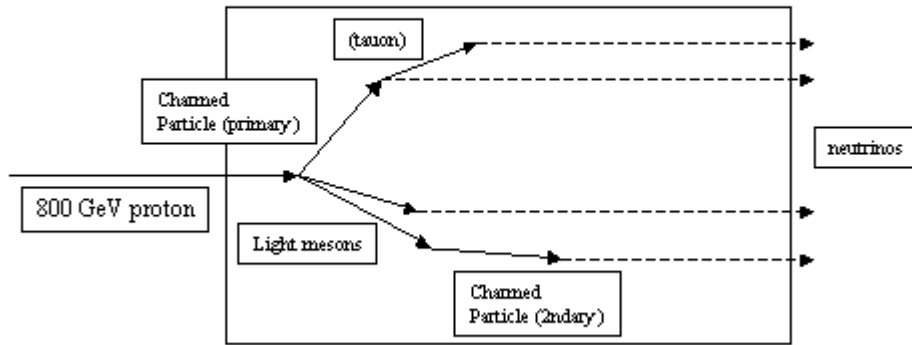
Figure 5-1: Neutrino production processes in the beam dump.

The second step was the generation of neutrino interactions in the target area using the LEPTO program package[72], specifically designed to simulate deep inelastic scattering processes.

Finally, tracking of interaction products through the apparatus was accomplished using the GEANT detector description tool[73].

The following is a detailed description of each of the processes and its implementation in the event simulation. Section 5.2 describes neutrino production in the beam dump. Section 5.3 details interaction of neutrinos with nuclear matter (Deep Inelastic Scattering) and implementation of event selection efficiencies in the simulation.

5.2 Neutrino Production

5.2.1 Charm Production

The interaction between the proton beam and the tungsten target produces a variety of hadron species. Because the beam dump is a massive block, most long-lived particles such as π's and K's will reinteract before decaying. While most

neutrinos in the beam come from light meson decays, but are produced at high angles and low energies, the dominant contribution to the neutrino interactions comes from decays of short-lived particles, and specifically from charmed mesons.

The dependence of the individual cross sections on A can be expressed by the empirical equation[74]

$$\sigma(A) = \sigma(A = 1)A^{\alpha} \tag{5.1}$$

where A denotes the atomic mass.

The total charm production cross section per incident proton on target (*pot*) is therefore

$$\frac{N_{c\bar{c}}}{pot} = \frac{\sigma_{c\bar{c}}(A)}{\sigma_{pN}(A)} = \frac{\sigma_{c\bar{c}}(A = 1)A^{\alpha_{c\bar{c}}}}{\sigma_{pN}(A = 1)A^{\alpha_{pN}}} \tag{5.2}$$

For the total proton-nucleon cross section the parameter α_{pN} has been found to be 0.7[75]. The corresponding values for the charm cross section are shown in Table 5-1.

Experiment	Beam	Target	Energy	$\alpha_{c\bar{c}}$
WA 92[76]	π	W, Cu	350 GeV	0.95±0.07
E789[77]	p	Au, Be	800 GeV	1.02±0.04
E769[78]	π	W, Cu, Si	250 GeV	1.00±0.06
WA 82[79]	π	Si, W	350 GeV	0.92±0.06
Average				0.986±0.027

Table 5-1: Experimental values for $\alpha_{c\bar{c}}$.

In order to calculate the total cross section one then has to measure the cross section per nucleon. Several experiments have published results for this value using a variety of beam particles and energies. A comprehensive discussion of charm production data and the ratios of the individual D mesons is given in ([41]). Another – smaller – contribution comes from the charmed baryon Λ_c. Its production cross section as a fraction of total charm has been measured using a refit to E531 data[80] as

$$\frac{\sigma(\Lambda_c)}{\sigma(charm)} = 0.11 \pm 0.04 \text{ for } E > 20 \text{ GeV}.$$

A summary of the production cross sections for the relevant charmed particles is shown in Table 5-2.

Particle	$\sigma(pN,800\ GeV)$ [μbarn]
D_s	11.3±2.2
$D^\pm$	27.4±2.6
D^0	5.2±0.8
Λ_c	5.4±2.1

Table 5-2: Production cross sections for charmed mesons.

For the differential cross section, the empirical expression

$$\frac{d^2\sigma}{dx_F\,dp_t^2} \propto (1-|x_F|)^n\, e^{-bp_t^2} \tag{5.3}$$

with

$$x_F \equiv \frac{p_L}{p_{L,\max}} \tag{5.4}$$

has been found to represent a good approximation for moderate values of the transverse momentum p_t [81].

The parameters n and b have been measured for D mesons by two experiments with 800 GeV protons on a fixed target. The result is shown in Table 5-3.

Experiment	b	n
E653[82]	$0.84^{+0.10}_{-0.08}$	$6.9^{+1.9}_{-1.8}$
E743[83]	$0.8^{-0.2}_{-0.2}$	$8.6^{+2.0}_{-2.0}$
Average:	$0.83^{+0.09}_{-0.08}$	$7.7^{+1.4}_{-1.4}$

Table 5-3: Fit parameters b and n for 800 GeV proton-nucleon interactions.

Λ_c production has been studied by the E781 collaboration using a 540 GeV proton beam. Their result is $n(\Lambda_c) = 3.5 \pm 0.4$ [84]. Since there is no published result for b, the approximation $b(\Lambda_c) = 1.0$ was used in the simulation.

Another concern is the size of the leading quark effect, which implies that forward production of particles is enhanced if they share a quark with the incoming

beam. The production ratio of D^+ and D^- as a function of x_F has been measured by several experiments. In the region up to $x_F = 0.3$, where most of the mesons are produced, WA 82[85] and E769[86] find no asymmetry, while E791[87] finds a small effect of order 10%. For the asymmetry between D_s^- and D_s^+, E791 obtains a null result[88]. In this thesis leading-quark effects will be assumed to be negligible.

Theoretical calculations of the total charm cross section suffer from large uncertainties due to the strong dependence on the charm quark mass, which is not well known. Figure 5-2 and Figure 5-3 show the results from a calculation at the next-to-leading-logarithm level[89], together with experimental results, for π-N and p-N interactions.
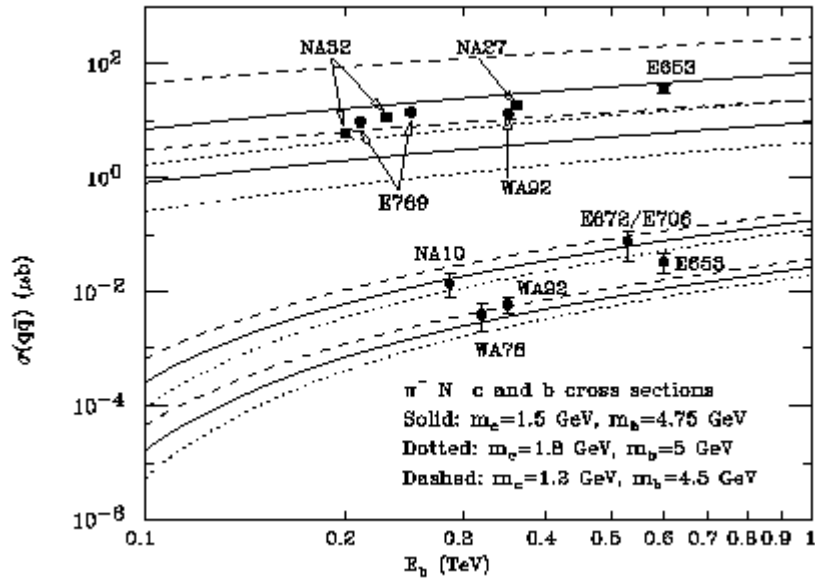
Figure 5-2: Charm and bottom production cross sections in pion-nucleon collisions: Experimental results and theoretical calculation([90]). The two bands correspond to uncertainties in theory.

73
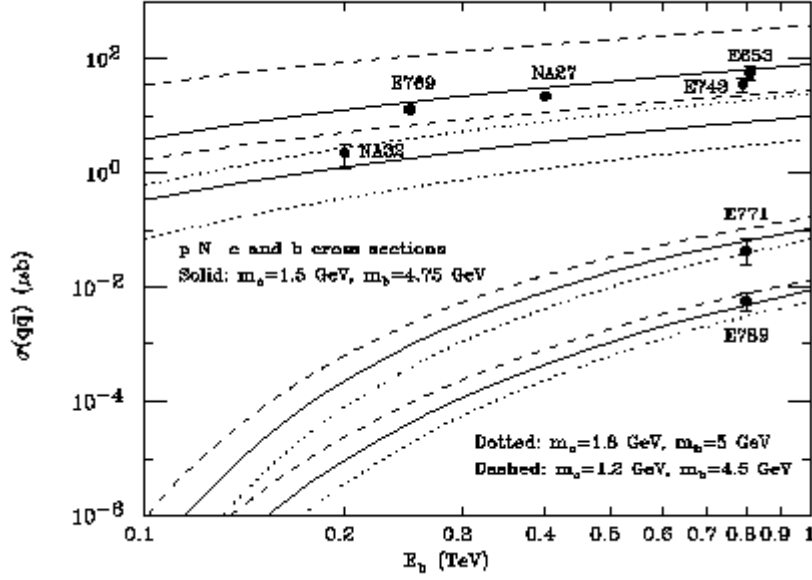
Figure 5-3: Charm and bottom production cross section in proton-nucleon collisions: Experimental results and theoretical calculation ([90]). The two bands correspond to uncertainties in theory.

5.2.2 Neutrino Production

The branching fractions of most leptonic and semileptonic decay modes of charmed mesons are reasonably well known[36]. However, the branching ratio for $D_s \to \tau \nu_\tau$ has not been measured very accurately but can be inferred from other decay modes using lepton universality.

The rate for the leptonic decay $D_s \to l \nu_l$ is given by:

$$\Gamma(D_s \to l\nu_l) = \alpha \cdot f_{D_s}^2 m_l^2 (1 - \frac{m_l^2}{m_{D_s}})^2 \tag{5.5}$$

The proportionality factor

$$\alpha = \frac{G_F^2}{8\pi} m_{D_s} |V_{cs}|^2 \tag{5.6}$$

is well-known experimentally. Therefore the ratio of two leptonic decay widths can be expressed as:

$$\frac{\Gamma(D_s \to l_1 \nu_{l_1})}{\Gamma(D_s \to l_2 \nu_{l_2})} = \frac{m_{l_1}^2 (1 - \frac{m_{l_1}^2}{m_{D_s}^2})^2}{m_{l_2}^2 (1 - \frac{m_{l_2}^2}{m_{D_s}^2})^2}$$

(5.7)

The branching ratio to tauons can be calculated by using the decay constant f_{D_s} as measured in muonic decays. As shown in Table 5-4, this improves the result considerably compared to using only direct measurements of $D_s \to \tau \nu_\tau$.

Experiment	Decay	f_{D_s} [MeV]
CLEO[91]	$D_s \to \mu \nu_\mu$	280±45
WA 75[92]	$D_s \to \mu \nu_\mu$	238±70
BES[93]	$D_s \to \mu \nu_\mu, D_s \to \tau \nu_\tau$	430±160
E653[94]	$D_s \to \mu \nu_\mu$	280±40
L3[95]	$D_s \to \tau \nu_\tau$	309±80
DELPHI[96]	$D_s \to \tau \nu_\tau$	330±95
Average		285±25

Table 5-4: Measurements of the D_s decay constant.

The branching ratios of the various charmed particle decays are summarized in Table 5-5. If not indicated otherwise, the source for the numbers is ([36]). The value for the inclusive muonic branching ratio of D_s has not been measured. However, following the pattern for the other D mesons, it should be approximately the same as the electronic one.

	$\to \nu_e X$	$\to \nu_\mu X$	$\to \nu_\tau \tau$
D_s	$8^{+6}_{-5}\%$	$\approx 8^{+6}_{-5}\%$ [*]	(6.3±0.5)%
$D^\pm$	(17.2±1.9)%	(16.0±3.0)%	7.2×10^{-4} [97]
D^0	(6.75±0.29)%	(6.6±0.8)%	Not allowed
Λ_c	(2.1±0.6)%	(2.0±0.7)%	

Table 5-5: charmed meson branching ratios to final states including neutrinos.

---

[*] Assuming $BR(D_s \to \nu_\mu X) \approx BR(D_s \to \nu_e X)$.

For the subsequent tau lepton decays, the relevant parameters are decay modes and branching ratios supplied by the Particle Data Group[36].

5.2.3 Neutrino Production Monte Carlo

In the Monte Carlo simulation, charmed mesons were generated with momentum distributions as described by equation 5.3. The parameters b and n were supplied by the user. Meson decays were simulated by the subroutine GENBOD using standard decay modes as described above. The production of neutrinos from Λ_c decays was simulated separately.

Neutrino contributions from light meson and secondary charm decay required a more involved simulation of the production process. Interactions of 800 GeV protons with tungsten were simulated with GEANT, and all π and K mesons were recorded. For each step in the tracking algorithm, the following weight was assigned based on the probability of the corresponding particle to decay:

$$w \equiv \frac{l}{\gamma c \tau} = \frac{lmc}{E\tau} \tag{5.8}$$

where l is the length of the GEANT step and m and τ the mass and lifetime of the particle. Figure 5-4 shows a typical shower of light mesons produced by 10 incident protons as simulated in the Monte Carlo. Each dot corresponds to one GEANT step.

Although pions make the dominant contribution to the total neutrino flux, kaons account for almost as many neutrino interactions because of the higher average energy of their neutrinos. In the Monte Carlo, separate data files were generated for individual light meson contributions.

The same approach was used to simulate secondary charm production. Here, instead of simulating decays after each GEANT step, a charmed meson was generated, weighted according to the production cross section at the corresponding meson energy.

All neutrino production from charm, being common for all neutrino types, was summarily called "prompt". The contribution from light meson decays, producing almost exclusively muon neutrinos, was called "nonprompt".
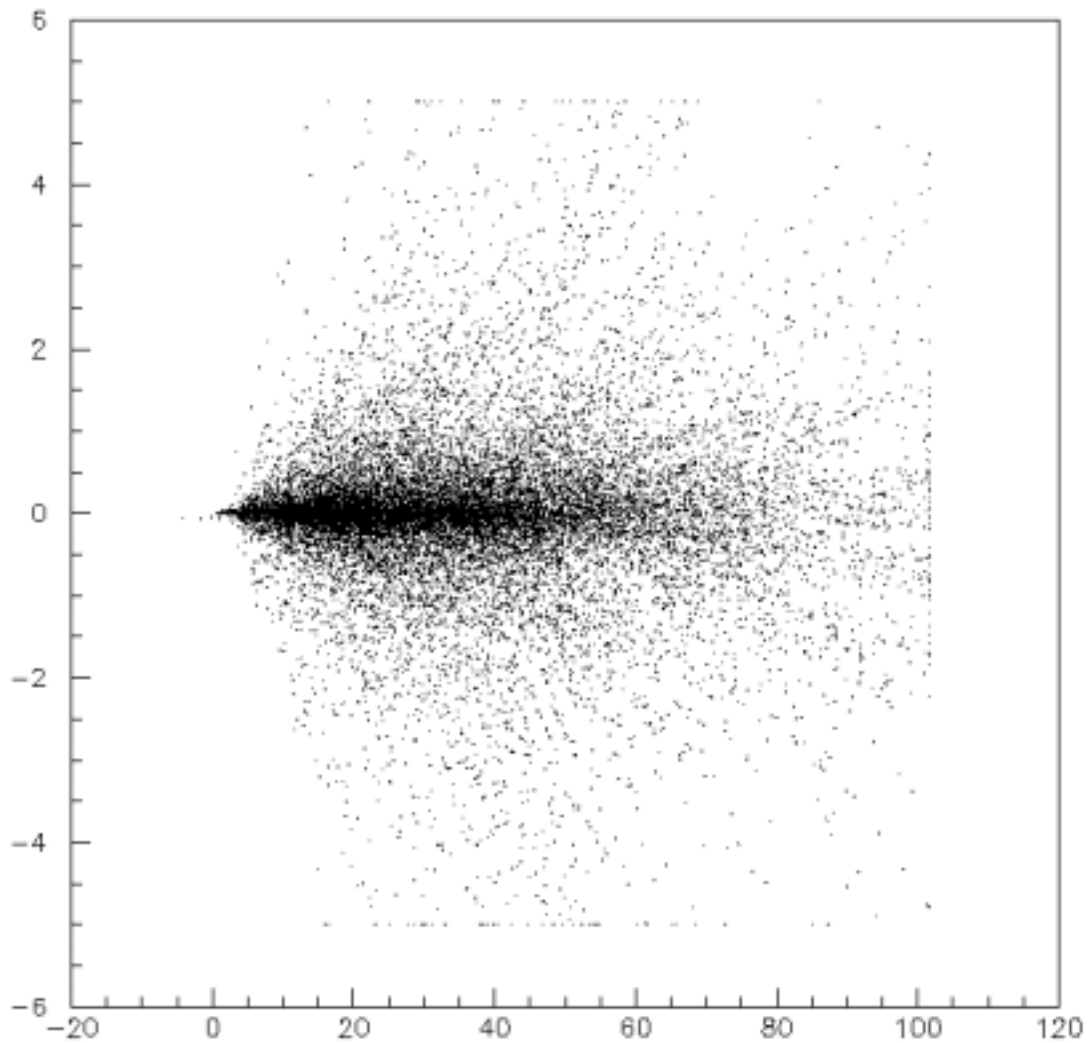
Figure 5-4: Meson shower in the beam dump from ten 800GeV protons incident from the left (Monte Carlo simulation). Scale on both axes is in cm. Each dot represents one GEANT tracking step of a light meson (pion or kaon).

5.3 Neutrino-Nucleon Interactions (DIS)

High-energy neutrinos typically interact via deep inelastic scattering (DIS). A sketch of this interaction topology is presented in Figure 5-5. The incoming neutrino interacts with a nucleon of the target material, producing both a lepton and a shower of hadrons. In the case of tau interactions, the lepton decays after a short distance, typically of the order of a few millimeters. 86% of τ decay modes

contain a single charged daughter, leaving a signature "kink" in the visible track that can be used to identify tau neutrino interactions.
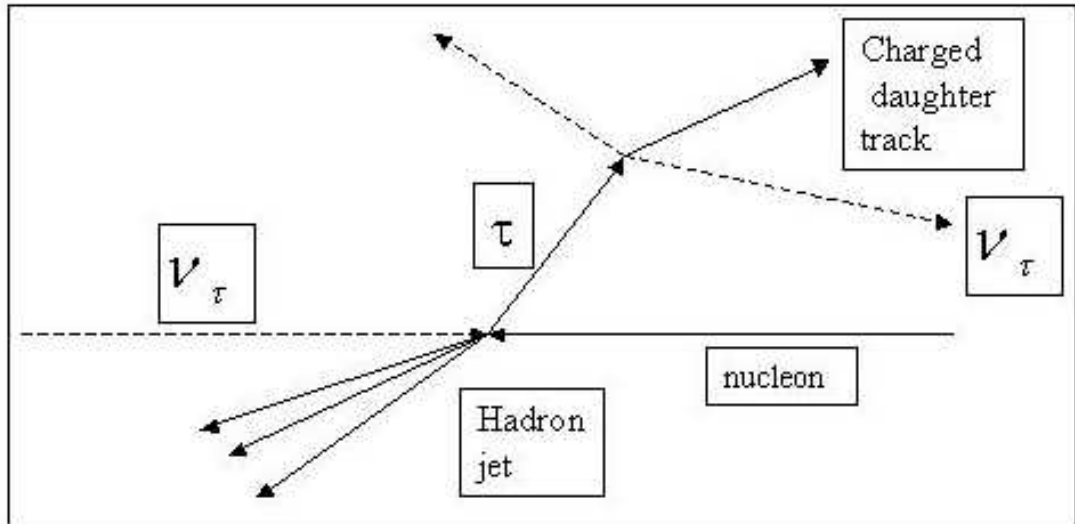
Figure 5-5: Tau Neutrino charged-current interaction in CM system.

5.3.1 Phenomenology

The kinematic variables used to describe the deep inelastic scattering interactions are shown in Figure 5-6.
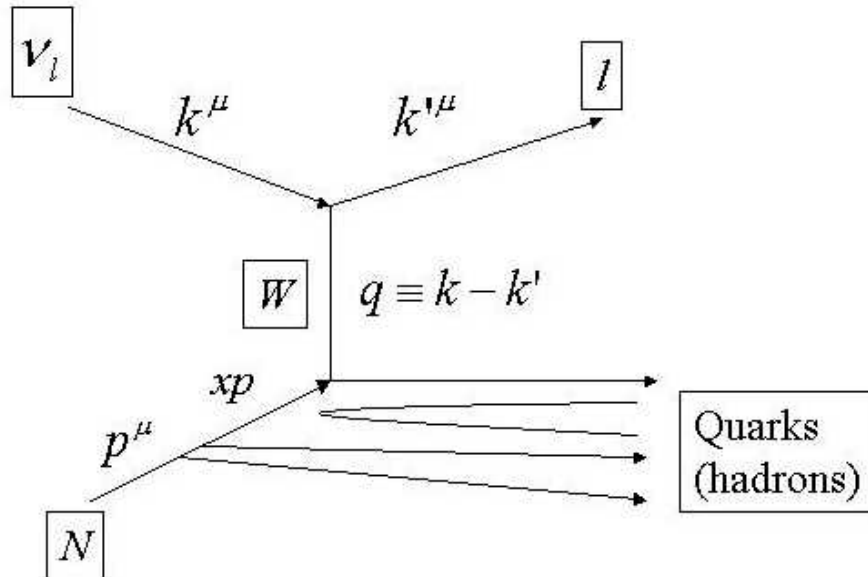
Figure 5-6: Kinematic variables in DIS.

The three relevant variables, the squared momentum transfer Q^2, the inelasticity y and the Bjorken-x, are given by:

$$Q^2 \equiv -q^2 \equiv (k-k')^\mu (k-k')_\mu \tag{5.9}$$

$$y \equiv \frac{E_{had,lab}}{E_{v,lab}} = \frac{pq}{pk_{lab}} \cong \frac{1}{2}(1-\cos\theta_{CM}) \tag{5.10}$$

$$x \equiv \frac{-q^2}{2qp} = \frac{Q^2}{2m_N E_{had}} \tag{5.11}$$

The differential (anti-) neutrino-nucleon cross section expresses in terms of these variables is:

$$\frac{d^2\sigma^{vN(\bar{v}N)}}{dxdy} = \frac{G^2 m_N E_v}{\pi}\left[(1-y)F_2^{vN}(x) + \frac{y^2}{2}2xF_1^{vN}(x) \pm y(1-\frac{y}{2})xF_3^{vN}\right] \tag{5.12}$$

with $\left(\pm \begin{array}{l} + \to v \\ - \to \bar{v} \end{array}\right)$, where the $F_i^{vN}(x)$ are the structure functions that describe the momentum distribution of partons in the nucleons. In the large-q^2 limit, and neglecting non-fermion parton contributions, one gets

$$\frac{2xF_1}{F_2} \cong 1 \tag{5.13}$$

and the cross section simplifies to:

$$\frac{d^2\sigma^{vN(\bar{v}N)}}{dxdy} \cong \frac{G^2 m_N E_v}{\pi}\left[(1+(1-y)^2)(F_2^{vN}(x) \quad xF_3^{vN})\right] \tag{5.14}$$

The structure functions may be written in terms of the nucleon's quark- and antiquark content:

$$\begin{aligned} F_2^{vN}(x) &= 2x(q(x)+\bar{q}(x)) \\ xF_3^{vN}(x) &= 2x(q(x)-\bar{q}(x)) \end{aligned} \tag{5.15}$$

This leads to:

$$\begin{aligned} \frac{d^2\sigma^{vN}}{dxdy} &\cong \frac{G^2 m_N E_v x}{\pi}\left[q(x)+\bar{q}(x)(1-y)^2\right] \\ \frac{d^2\sigma^{\bar{v}N}}{dxdy} &\cong \frac{G^2 m_N E_v x}{\pi}\left[\bar{q}(x)+q(x)(1-y)^2\right] \end{aligned} \tag{5.16}$$

Integrating over x then gives:

$$\frac{d\sigma^{\nu N}}{dy} \cong \frac{G^2 m_N E_\nu}{\pi} \left[Q + \overline{Q}(1-y)^2 \right]$$ (5.17)

with Q and $\overline{Q}$ exchanged for antineutrinos, where $\overset{(-)}{Q} \equiv \overset{(-)}{q}(x)x\,dx$.

Only the following charged-current processes involving u and d quarks and their antiparticles are allowed:

$$\nu_l d \rightarrow l^- u$$
$$\nu_l \overline{u} \rightarrow l^- \overline{d}$$
$$\overline{\nu}_l u \rightarrow l^+ d$$
$$\overline{\nu}_l \overline{d} \rightarrow l^+ \overline{u}$$ (5.18)

A nuclear material containing equal numbers of protons and neutrons - and hence equal numbers of u and d quarks - would therefore have a cross section 3 times larger for neutrinos than for antineutrinos, since $\int_0^1 (1-y)^2 \, dy = 1/3$. However, the values become more equal because of the presence of a quark "sea" containing the same number of quarks and antiquarks. The total cross section in muon neutrino CC interactions was measured[36] to be:

$$\sigma(\nu N) = 0.677 \pm 0.014 \times 10^{-38} \, cm^2 GeV^{-1}$$
$$\sigma(\overline{\nu} N) = 0.334 \pm 0.008 \times 10^{-38} \, cm^2 GeV^{-1}$$ (5.19)

Muon and electron masses are negligible for the neutrino energies in this experiment (>5 GeV), and cross sections for CC events can be assumed to be linear in E. In the case of ν_τ CC events, the finite tau lepton mass gives rise to a kinematic factor K_F such that

$$\sigma_{\tau CC}(E) = K_F(E)\sigma_{\mu CC}(E) = K_F(E) \cdot \alpha \cdot E$$ (5.20)

The method to calculate this factor numerically has been described by Albright and Jarlskog[98], and the result is shown for ν_τ and $\overline{\nu}_\tau$ in Figure 5-7.
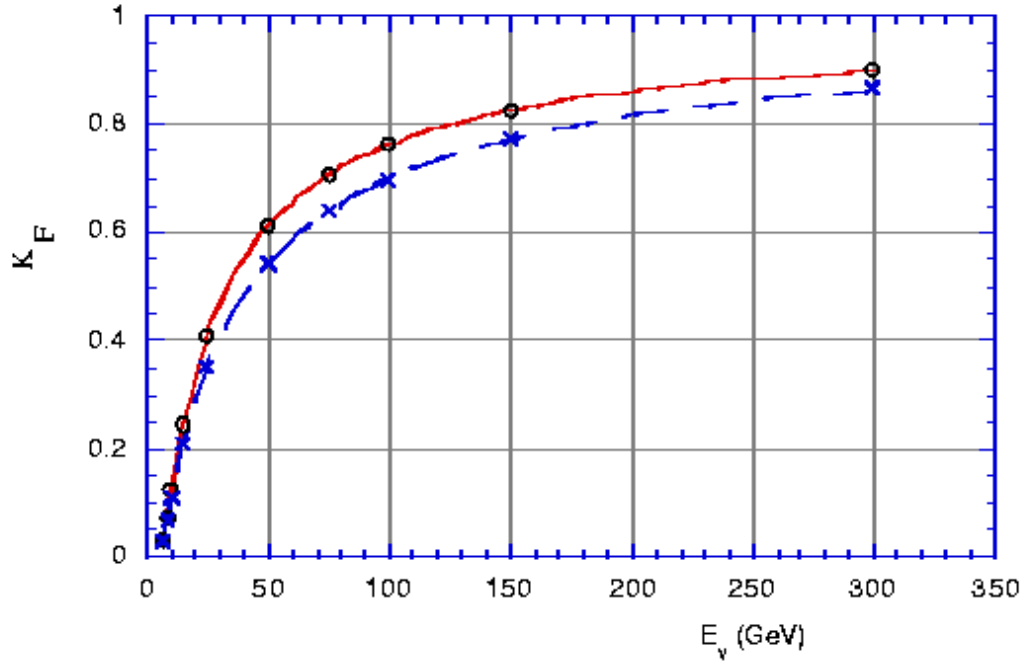
Figure 5-7: Kinematic factor for tau neutrino charged-current interactions (solid: neutrino, dashed: antineutrino).

Neutral current interactions make an additional contribution to neutrino events. The general expression for the differential cross section in neutrino neutral current interactions is:

$$\frac{d\sigma}{dy} = \frac{G^2 m E_\nu}{2\pi} \left[(g_V \pm g_A)^2 + (1-y)^2 (g_V \quad g_A)^2 + O\left(\frac{m}{E_\nu}\right) \right] \qquad (5.21)$$

Here g_V and g_A correspond to the vector and axial coupling strengths and m is the mass of the target particle. In neutrino-nucleon scattering, accounting for the dominant part of neutral current events, there are additional effects due to quark-quark interactions. The ratio of the total cross section for neutral current to charged-current events for $E_\nu > 30\,GeV$ has been measured by the CCFR collaboration[99] to be:

$$R_{\nu\bar{\nu}} \equiv \frac{NC(\nu) + NC(\bar{\nu})}{CC(\nu) + CC(\bar{\nu})} = 0.3117 \pm 0.0014(stat.) \pm 0.0018(ex.) \pm 0.0014(th.) \,(5.22)$$

5.3.2 Neutrino Interaction Simulation

The neutrino interaction Monte Carlo used a neutrino sample generated in the production simulation. The neutrinos were subjected to a geometrical target cut and an energy cut of *>5 GeV*, and then used as input for the LEPTO program package. Particles produced in the interaction were tracked through the apparatus with GEANT. All four target configurations were modeled separately in the simulation.

The user could choose form and level of detail in the output. This ranged from a complete DAFT data file with all simulated electronic detector hits, to a simple text file containing only basic interaction parameters. This information was used to model event selection, as described in Section 4. The following cuts and weights were applied:

- Interaction weight: This was simply the neutrino energy for muon and electron neutrinos; for tau neutrinos the kinematic factor was included as well.

- Trigger cut: For each event both possible trigger conditions were recorded. Depending on the event fulfilling both, one, or none of the trigger conditions, the weight supplied by the interaction routine was multiplied by a factor of 1, 0.5 or reduced to zero.

- Stripping and eye scanning: The events were weighted according to the number of primary charged tracks visible in the downstream scintillating fiber plane. Figure 5-8 shows the factors used to simulate the limited efficiency of the procedure. Their values depend on the emulsion module station in which the event took place. A comprehensive discussion of this factor can be found in ([41]).

- Emulsion analysis: The dependence of the location efficiency on the number of emulsion tracks is described in Section 4.4. For events with 3 or fewer tracks within 200 mrad of the forward direction, the weight was modified by another factor corresponding to the ratio of located to expected events, as shown in Figure 4.6.

- Muon event selection: The same momentum and geometry cuts were applied as in the event selection discussed above.

Efficiency multiplicator
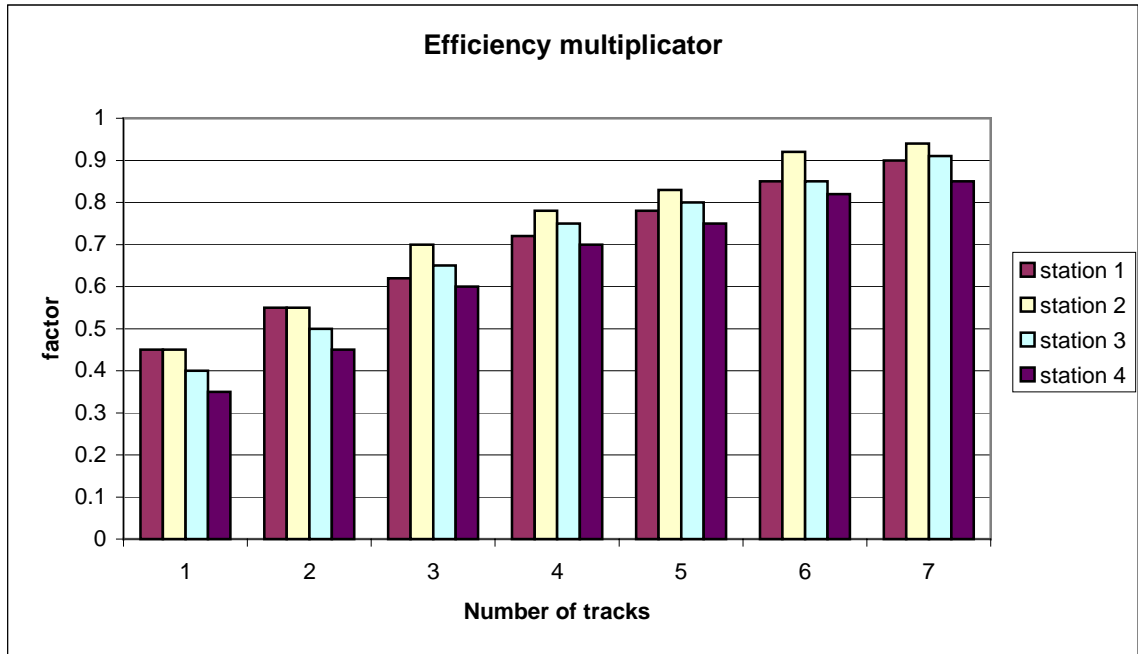
Figure 5-8: Multiplicative factor used to simulate stripping/eye scanning efficiency. The value depends on the emulsion module station (most upstream: station 1).

5.3.3 Monte Carlo Results

Energy spectra for the five components of the neutrino beam are illustrated in Figure 5-9 and Figure 5-10. Those spectra include the geometrical target cut and the interaction weight. While the prompt neutrino contribution for muon and electron neutrinos is of almost identical shape, the situation for tau neutrinos is different. Figure 5-11 shows the energy spectrum for tau neutrinos. The lower peak stems from tau neutrinos originating in D_s decays, the higher peak from those produced in the decay of the tau lepton itself.

Table 5-6 shows the efficiencies for event selection and muon identification in muon charged-current events from all sources. Table 5-7 and Table 5-8 show the efficiencies for vertex location in the emulsion for all types of neutrino events.
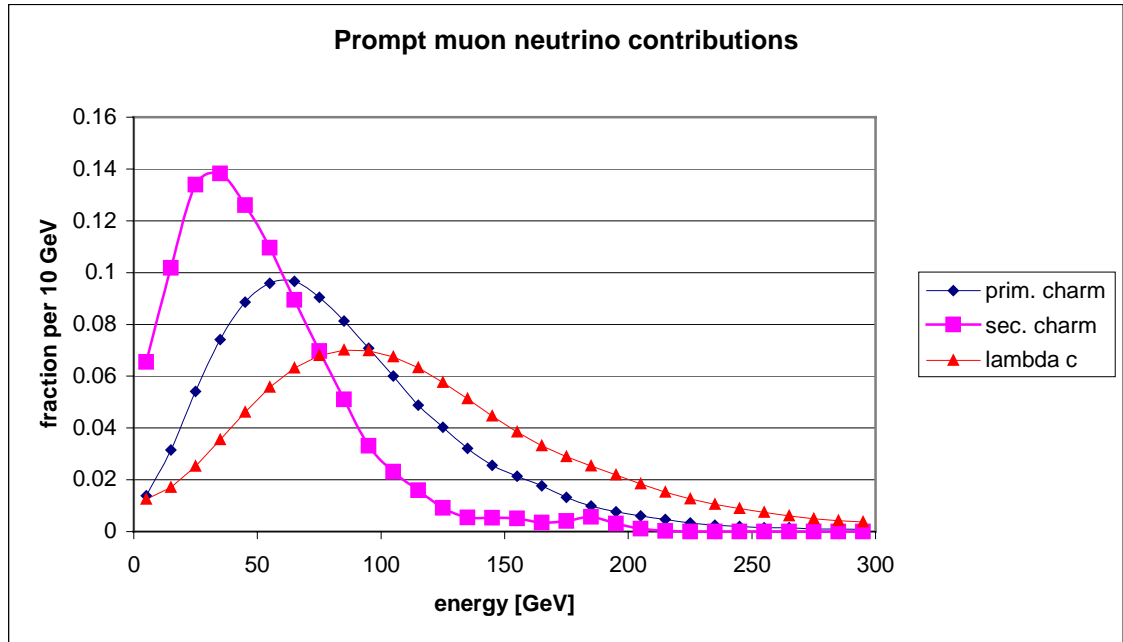
Figure 5-9: Simulated energy spectra for the three different prompt neutrino contributions. The spectra are essentially the same for muon and electron neutrinos. Each component is individually normalized to unit area.
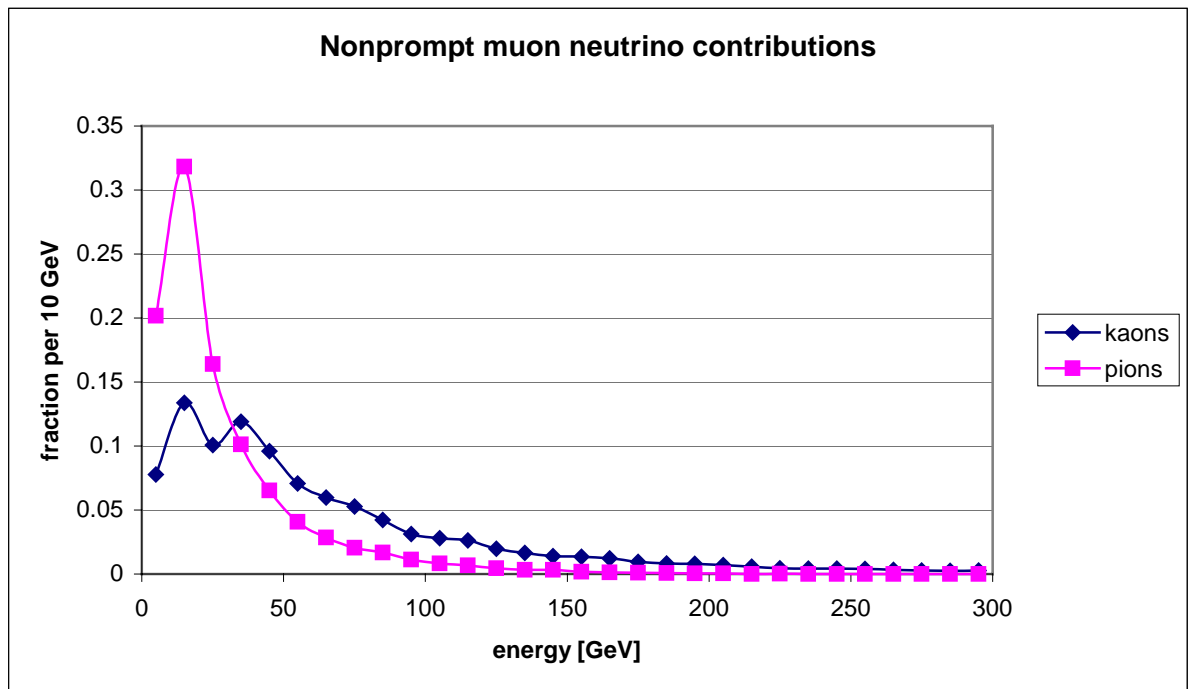
Figure 5-10: Simulated energy spectra for the two nonprompt muon neutrino contributions. Each component is individually normalized to unit area.
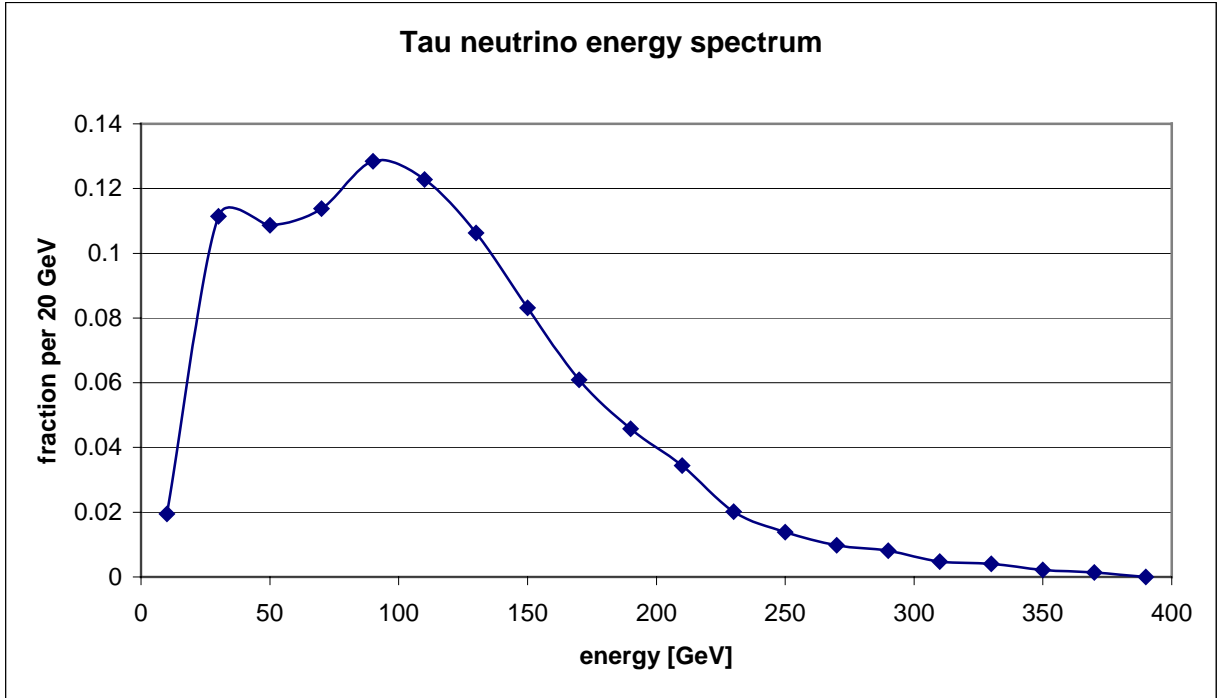
Figure 5-11: Simulated energy spectrum of interacting tau neutrinos. The two peaks are caused by the two different tau neutrino sources (D_s decay into $\tau \nu_\tau$ and subsequent $\tau \to \nu_\tau X$ decay).

Neutrino source	*D* mesons	Pions	Kaons	Λ_c	Sec. Charm
T1	92.0%	72.7%	85.1%	94.3%	63.6%
T1.or.T2	97.4%	79.5%	90.7%	98.7%	71.6%
Average trigger efficiency	94.7%	74.6%	78.7%	96.5%	67.6%
Stripping	80%	75%	79%	81%	78%
Muon Momentum > 5 GeV	98.8%	94.8%	97.9%	99.0%	98.9%
Muon ID wall cut	73.5%	46.2%	63.0%	79.7%	62.5%
Overall efficiency	55%	25%	43%	62%	33%

Table 5-6: Efficiencies for electronic event selection and muon identification, from Monte Carlo simulation, for all significant muon neutrino sources.

Neutrino source	D mesons	Pions	Kaons	Λ_c	Sec. Charm
T1	92.0%	72.7%	85.1%	94.3%	63.6%
T1.or.T2	97.4%	79.5%	90.7%	98.7%	71.6%
Average trigger efficiency	94.7%	74.6%	78.7%	96.5%	67.6%
Stripping	80%	75%	79%	81%	78%
Vertex Location	79%	60%	73%	83%	74%
Overall efficiency	60%	34%	51%	65%	39%

Table 5-7: Monte Carlo event selection efficiencies for vertex location in emulsion (muon neutrino charged-current interactions).

Interaction type	e CC	τCC	NC
T1	97.2%	96.0%	81.6%
T1.or.T2	99.3%	98.4%	86.7%
Average trigger Efficiency	98.2%	97.2%	84.2%
Stripping	80%	80%	81%
Vertex Location	73%	73%	75%
Overall efficiency	57%	56%	52%

Table 5-8: Monte Carlo event selection efficiencies for vertex location in emulsion (non-muon CC neutrino interactions).

6 Result

6.1 Introduction

The reason to use actual data instead of a first-principles calculation for the determination of the ν_τ-nucleon cross section can be seen by looking at the equation for the event yield.

The total number of observable neutrino interactions of type α is:

$$N_{ev,\alpha} = n_\alpha(E) \cdot \sigma_{\nu_\alpha N}(E) \cdot \varepsilon_\alpha(E) \cdot dE \tag{6.1}$$

where

$$n_\alpha(E) \equiv \sum_i \sigma(pN \to C_i X) \cdot BR(C_i \to \nu_\alpha X) \cdot \eta_\alpha(E) \cdot \frac{dN_{\nu_\alpha,prod}(E)}{dE} \tag{6.2}$$

is the energy distribution of the neutrinos incident on the emulsion target. Here $\eta(E)$ is the geometrical target acceptance and $\varepsilon(E)$ is the event location/selection efficiency. Both depend on the neutrino energy and type. The C_i stand for charmed particles involved in the neutrino production ($D^\pm, D^0, D_s, \Lambda_c$). The contributions from all possible sources have to be summed.

The various efficiencies would lead to a large systematic error in any first principles calculation. Using actual data reduces the magnitude of this error, since unknown factors that are common to all event types cancel out, and the size of other errors can be reduced. The constant factor in the cross section of tau neutrino charged-current interactions can be calculated as

$$\sigma_{0\tau CC} = \frac{N_{ev,obs}(\nu_\tau CC)}{N_{ev,obs}(\nu_x CC)} \cdot \frac{\bar{\varepsilon}_{\nu_x CC}}{\bar{\varepsilon}_{\nu_\tau CC}} \cdot \frac{N_{\nu_x,on\_tgt}}{N_{\nu_\tau,on\_tgt}} \cdot \frac{n_{\nu_x}(E) \cdot EdE}{n_{\nu_\tau}(E) \cdot K_F(E) \cdot EdE} \cdot \sigma_{0xCC} \tag{6.3}$$

where σ_{0xCC} is the constant factor in the cross section for massless neutrino charged-current interactions, corresponding to the parameter α in equation 5.20. The overall event selection efficiency is denoted as $\bar{\varepsilon}$. In this equation the kinematic factor K_F has been explicitly factored out.

If the tau neutrino is a standard neutrino, then its cross section in charged-current interactions is given by:

$$\sigma_{\pi CC}(E) = \sigma_{0\pi CC} \cdot E \cdot K_F(E) \tag{6.4}$$

and

$$\frac{\sigma_{0\pi CC}}{\sigma_{0xCC}} = 1 \tag{6.5}$$

The disadvantage of using real data is that the calculation has to rely on a comparatively small number of events, introducing a statistical error that dominates the final result.

Two kinds of data were used to obtain an estimate for the beam composition. The first is the muon momentum spectrum for identified muon events, the second the distribution of electromagnetic calorimeter energy in the entire event sample.

Muon charged-current events can be easily identified. However, in order to use them for the purpose of event yield normalization, it is important to find the fraction of muon events coming from neutrinos produced in charm decays (prompt) as opposed to those from light meson decays (nonprompt). This can be achieved by fitting the momentum spectrum of the primary muons to a mixture of the expected spectra for both sources and leaving the ratio as a free parameter.

Another identifiable data sample is electron charged-current events, as they deposit more energy in the electromagnetic calorimeter. Because of this fact, simulated distributions to the data can be used to determine the fraction of electron charged-current events in the total event sample.

6.2 Muon Charged-Current Events

6.2.1 Muon momentum Distributions

Calculating the effective prompt neutrino spectra depends on the number of neutrinos produced per proton on target, on target acceptance and on the interaction probability for each of the individual components.

For the contribution from primary charm, the number of neutrinos per proton on a target with atomic number A is:

$$\frac{N_{\nu_x}}{pot} = \quad \sigma(C_i, A) BR(C_i \rightarrow \nu_x X) \tag{6.6}$$

where parameters are defined as in equation 6.2. Relevant parameters for the calculation are listed in Table 5-2 and Table 5-5.

For secondary charm, the number of neutrinos per proton on target required a separate Monte Carlo program. Table 6-1 shows the results for the three prompt contributions to the muon neutrino spectrum. The error on the average energy results from the uncertainties in the differential cross section (parameters b and n).

Component	$N_\nu \, pot^{-1}$ on emulsion target	$\overline{E}_\nu$ on emulsion target [GeV]	Selection efficiency	Expected fraction of identified interactions
Primary charm	$3.0 \pm 0.7 \times 10^{-5}$	56±6	55%	90.3±2.2%
Secondary charm	$2.0 \pm 1.0 \times 10^{-6}$	33±5	33%	7.5±3.3%
Λ_c	$1.5 \pm 0.7 \times 10^{-6}$	81±6	62%	2.2±1.1%

Table 6-1: Normalization of prompt muon neutrino interactions. All values are from Monte Carlo. For details on selection efficiency see Table 5-6.

The nonprompt component comes from decays of pions and kaons. The result of the normalization is shown in Table 6-2. Since the physics of light mesons is well understood, there are no major systematic uncertainties. Background sources not included in the simulation are discussed in Appendix B. They were not included in the fit, since expected numbers of muon events from these sources are very small.

Figure 6-1 shows the muon momentum distributions as simulated by the Monte Carlo program.

Component	$N_\nu \, pot^{-1}$ on emulsion target	$\overline{E}_\nu$ on emulsion target [GeV]	Selection efficiency	Expected fraction of identified interactions
$\pi^{\pm}$	6.9×10^{-5}	15.3	25%	47%
$K^{\pm}, K_L^0$	2.6×10^{-5}	26.7	43%	53%

Table 6-2: Normalization of nonprompt muon neutrino interactions. All values are from Monte Carlo. For details on selection efficiency see Table 5-6.
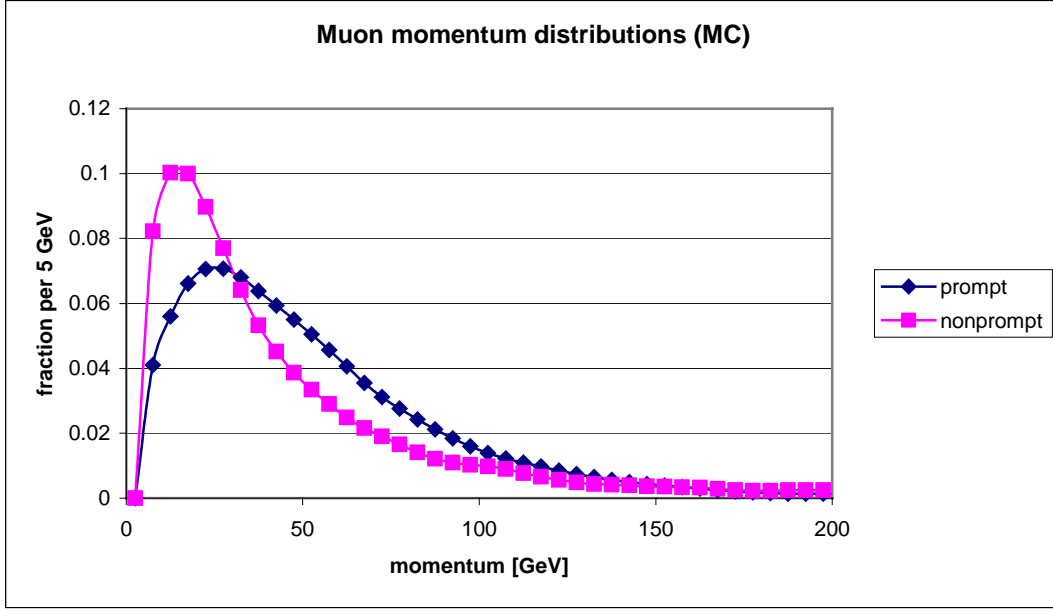
Figure 6-1: Monte Carlo momentum distributions for prompt and nonprompt muons. Both distributions are normalized to unit area.

6.2.2 Fitting Procedure

The muon momentum data obtained in the event reconstruction as described in section 4.5 was binned and fitted to the Monte Carlo distribution using two different methods.

The first is a least squares method, in which data and Monte Carlo distributions are binned into bins of the same size. The theoretical distribution was normalized such that

$$\sum_{i=1}^{bins} n_i^{th} = \sum_{i=1}^{bins} n_i^{obs} \tag{6.7}$$

where n_i is the number of events in each bin. The best fit is then found by minimizing the quantity

$$S \equiv \sum_{i=1}^{bins} \left(\frac{n_i^{obs} - n_i^{th}(\alpha)}{\sigma_i} \right)^2 \tag{6.8}$$

The theoretical shape depends on a free parameter α, in this case the ratio of prompt to total muon events, such that

$$n_i^{th}(\alpha) = \alpha \cdot n_i^{th,prompt} + (1-\alpha) \cdot n_i^{th,nonprompt} \tag{6.9}$$

Provided the number of events in each bin is sufficiently large, the error can be assumed to be Gaussian with

$$\sigma_i = \sqrt{n_i^{th}} \approx \sqrt{n_i^{obs}} \tag{6.10}$$

The standard error on the result then can be calculated by finding the value α' so that

$$S(\alpha') = S_{min}(\alpha) + 1 \tag{6.11}$$

The second method used for the fitting was a maximum-likelihood method. In that case, the theoretical shapes are normalized to unity to represent probability distributions $P(p)$. A best fit is then calculated by maximizing the function

$$l(\alpha) \equiv \ln L(\alpha) \equiv \ln \sum_{i=1}^{n_{events}} \alpha \cdot P_{pr}(p_i) + (1-\alpha) \cdot P_{nonpr}(p_i) \tag{6.12}$$

where the p_i are individual momentum values in the data sample. The standard error is then calculated by finding the value α' for which

$$l(\alpha') = l_{min}(\alpha) - 1/2 \tag{6.13}$$

Ideally, both methods should yield the same result. Comparing them therefore provides an additional systematic check. A more detailed description of the fitting methods can be found in ([100]).

6.2.3 Muon spectrum fit results

The result for the fit of the Monte Carlo distributions to the muon momentum data is shown in Figure 6-2. The two methods are compared in Table 6-3.

The two fitting methods give nearly identical results. The best fit has a value of $\chi^2/dof = 3.55/8$.
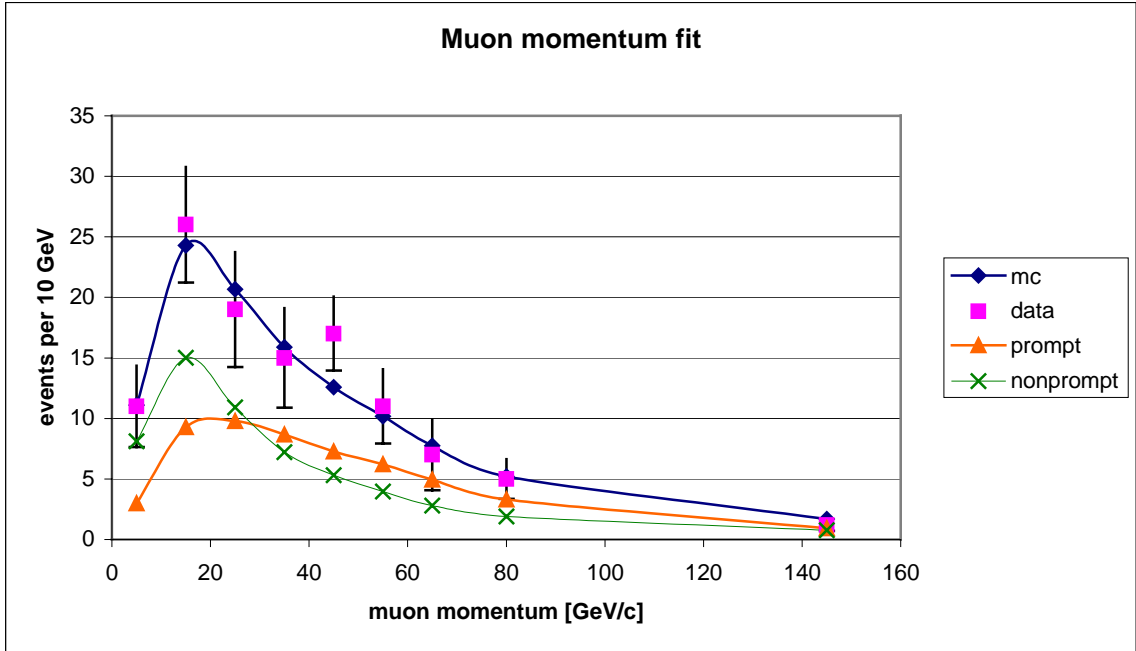
Figure 6-2: Composition of muon sample by neutrino source (mean).

Fit Method	Result (prompt/total)
Maximum Likelihood	0.48±0.19
Least Squares	0.49±0.18
Combined:	0.49±0.18(*stat.*) ±0.01(*sys.*)

Table 6-3: Result of fit to muon momentum data.

6.2.4 Consistency Checks

6.2.4.1   Momentum Cut

Another way to check the consistency of the result is to vary the momentum cutoff. Figure 6-3 shows the expected fluctuations in the result as a function of the momentum cut. The plot was generated using samples of fake data generated in a Monte Carlo simulation.

While varying the momentum cut one has to correct the fit result to account for different fractions of each component remaining. The corrected fraction is related to the raw fit result by

$$\frac{f_{\mu CC,prompt,corr}}{f_{\mu CC,nonprompt,corr}} = \frac{\int_{p_{cut}}^{\infty} \hat{n}_{nonprompt}(p)dp}{\int_{p_{cut}}^{\infty} \hat{n}_{prompt}(p)dp} \frac{f_{\mu CC,prompt,raw}}{f_{\mu CC,nonpromt,raw}} \qquad (6.14)$$

where $f_{\mu CC,(non)prompt}$ is the ratio of (non)prompt to total muon charged-current interactions and $\hat{n}(p)$ is the muon momentum distribution normalized to unit area. The calculation of the corrected ratio of prompt to total is straightforward.

Figure 6-4 shows the value for the ratio as a function of the momentum cut. The values are consistent within error bars and there is no visible trend in either direction. The size of the error bars in the plot is limited by the physicality of the solution ($0 \le p/total \le 1$).
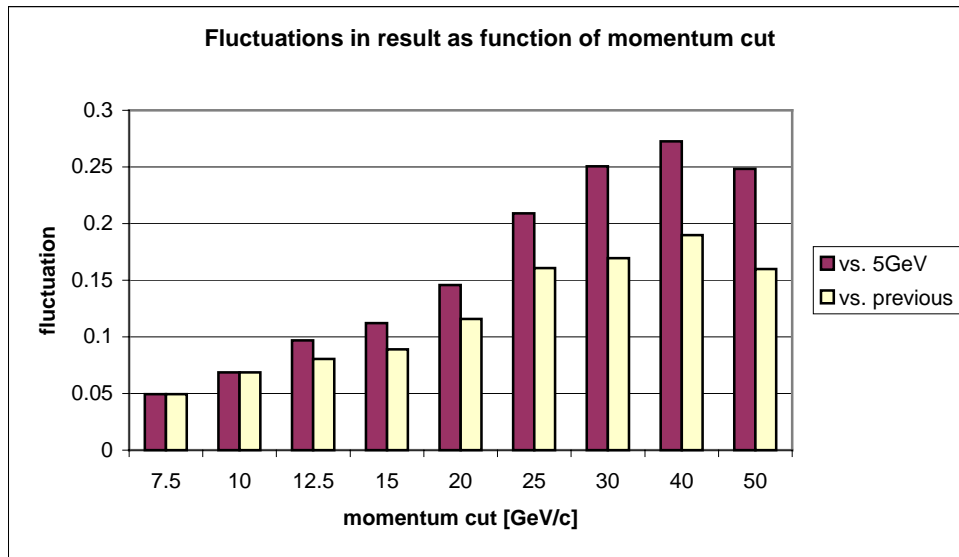
Figure 6-3: Expected fluctuation in result for prompt/total ratio as a function of the momentum cut. Dark bars: average difference to value corresponding with 5GeV/c momentum cut; light bars: average difference to next lower momentum cut.
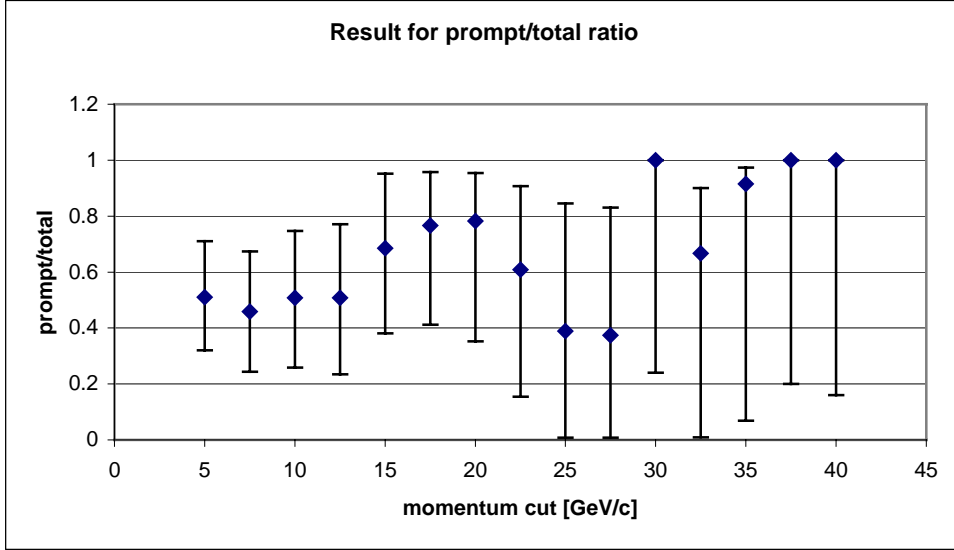
Figure 6-4: Variation of the prompt/total ratio as a function of the muon momentum cut.

6.2.4.2   Ratio μ^+ / μ^-

While not central to the investigation of the beam composition, the ratio of muons to antimuons is another way to look for systematic errors. The value for this ratio will be different from the raw value for the cross section ratio. The reason for this is the $(1-y)^2$ dependence of the $\overline{\nu}N$ interaction cross section. Antimuons are preferably produced with a higher longitudinal momentum, making identification of these events easier. The ratio between muons and antimuons, as calculated in a Monte Carlo simulation, is expected to be

$$R_{\pm,th} \equiv \frac{N_{\mu^+,ID}}{N_{\mu^-,ID}} = 0.56 \pm 0.01 \tag{6.15}$$

In the data sample, the type of interaction can be determined by the direction of the bend angle in the analysis magnet. The ratio of μ^+ to μ^- in the data was found to be 49:79, or, assuming the two numbers are independent,

$$R_{\pm,\exp} = 0.62 \pm 0.11 \tag{6.16}$$

The experimental value is therefore consistent with expectation. Figure 6-5 shows the momentum distribution for data and simulation. Negative momentum values correspond to muons, positive values to antimuons.

Muon Momentum by charge
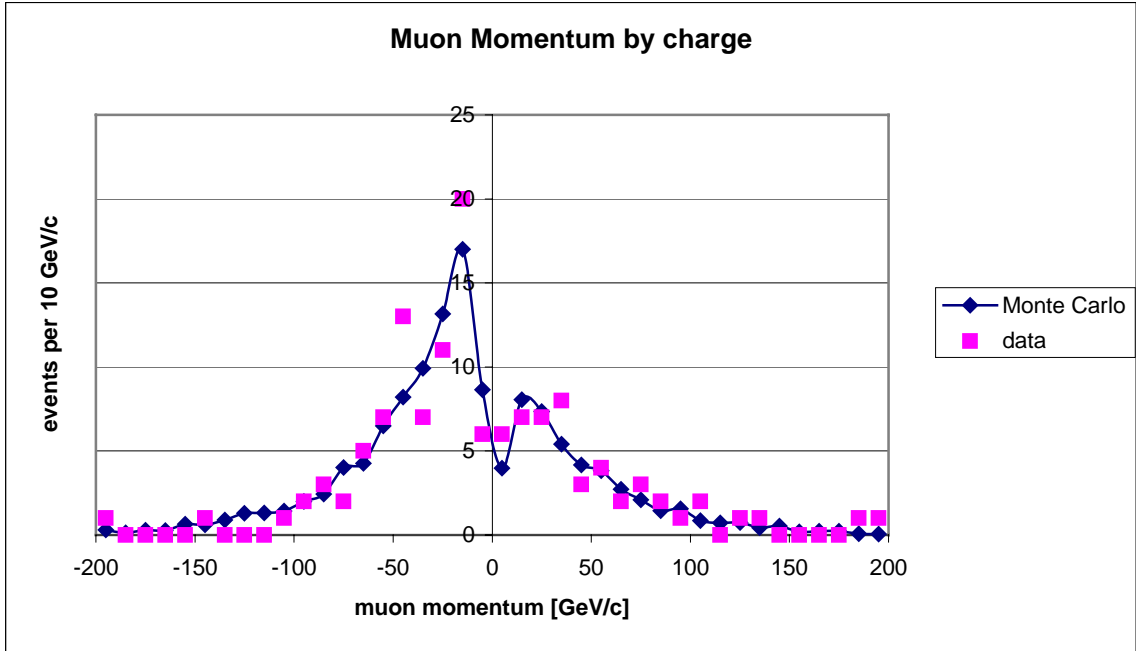
Figure 6-5: Momentum distribution of muons and antimuons. Negative values correspond to muons, positive values to antimuons. The spectrum was calculated using a prompt/total ratio of 0.49.

6.2.5 Systematic Errors

6.2.5.1 *Prompt Neutrino Beam Composition and Production Parameters*

As can be seen from Table 6-1, contributions from individual beam components are not well known. Also, the expected muon momentum spectrum depends on the differential charm production cross-section parameters *b* and *n*. By varying all parameters within their margins of error, one can estimate the size of the systematic error from these sources. Table 6-4 shows the results. The major source of error is the uncertainty in the parameter *n*, since neutrinos that interact come predominantly from the high energy side of the production distribution, dominated by the value of n.

Parameter	Value and error	Error in $f_{\mu CC, prompt}$
Secondary charm	7.5±3.3%	±0.01
Λ_c	2.2±1.1%	±0.005
B	0.83±0.09	<±0.005
N	7.7±1.4	±0.08
Result:		±0.08

Table 6-4: Systematic error from beam composition and charm production cross section uncertainties. The final result is obtained by adding the individual contributions in quadrature.

6.2.5.2 Electronic vs. Emulsion Events

The muon event sample selection did not require a located vertex in the emulsion, which creates an uncertainty in weighting the simulated events. As previously mentioned, there is an efficiency factor for located events depending on the number of emulsion tracks. For the events used in the momentum fit, this factor is not well known, since the number of emulsion tracks can only be determined for events with emulsion information.

In order to determine the systematic error introduced by this uncertainty, an additional fit was done using the momentum distribution expected for non-located events, i.e. without the weight depending on the number of emulsion tracks. The results for both fits are almost identical, although the latter has a slightly smaller statistical error.

An additional check on the result was performed using only events with complete emulsion information. Values are consistent, though the associated value for χ^2 / dof is higher. Table 6-5 shows results for the various fits.

Event sample/MC weight	Fit Result (prompt/total)	χ^2 / dof
All events/Emulsion track dependent weight	0.49±0.19	3.55/8
All events/No emulsion weight	0.49±0.17	3.52/8
Located events only	0.55±0.27	7.86/8

Table 6-5: Difference in fit result for different event weights, and result using only located events.

6.2.6 Result for Muon Momentum Spectrum Fit

The raw fit results have to be corrected for efficiencies to obtain a result for the prompt event fraction in the overall sample. Because of their lower average energy, nonprompt muons are more likely to miss the muon ID wall. Therefore the actual nonprompt contribution is higher than in the identified sample.

$$
f_{\mu CC,prompt,all} = \frac{\varepsilon_{ID,p}^{-1} \cdot f_{\mu CC,prompt,ID}}{\varepsilon_{ID,p}^{-1} \cdot f_{\mu CC,prompt,ID} + \varepsilon_{ID,np}^{-1} \cdot f_{\mu CC,nonprompt,ID}} = \frac{f_{\mu CC,prompt,ID}}{f_{\mu CC,prompt,ID} + \dfrac{\varepsilon_{ID,p}}{\varepsilon_{ID,np}}(1 - f_{\mu CC,prompt,ID})}
$$

(6.17)

where ε_{ID} stands for the muon identification efficiency, including the momentum cut. The result is slightly different depending on whether one uses the efficiency values for emulsion or electronic interactions. The raw value for the prompt fraction from Table 6-3 is 0.49±0.18(*stat.*)±0.01(*sys.*). Table 6-6 shows efficiency values generated in a Monte Carlo simulation and the final result.

Monte Carlo weight	$\varepsilon_{ID,p}$	$\varepsilon_{ID,np}$	Result (prompt/total)
Electronic vertex	71%	56%	0.41±0.19(*stat.*)±0.08(*sys.*)
Emulsion vertex	72%	53%	0.43±0.20(*stat.*)±0.08(*sys.*)
Combined:			0.42±0.19(*stat.*)±0.09(*sys.*)

Table 6-6: Final result for muon CC event ratio (all events) from muon momentum fit. Systematic error in final result takes into account difference between electronic and emulsion weighted value.

6.3 Electromagnetic Energy Spectrum

6.3.1 Fitting Procedure

The spectrum of energy deposited in the electromagnetic calorimeter provides an independent data set that also can be used to determine the beam composition. The difference in shape between the energy distributions of the electron charged-current events and other events is quite different, as shown in Figure 6-6. The reason for this difference is the presence of high-energy electrons in electron charged-current events.

The tagged muon sample can be used to verify the quality of the calorimeter data, since there are no uncertainties about the nature of the parent neutrino. Figure 6-7 shows the energy spectrum for all identified muon events. For all bins the data agrees with prediction within error bars, giving no indication for any unknown background that might distort the spectrum.

Other than for identifying electron CC events, the energy spectrum has very little discriminating power. For this reason, several constraints had to be imposed on the relative contributions from the different sources in the overall fit. Those were:

- The number of prompt muon and electron events was assumed to be equal except for detection efficiencies.
- The neutral current fraction was fixed at 0.21±0.03 since it is almost independent of beam composition.
- The number of tau events was expressed as a fraction of prompt muon events. Here standard values for cross sections were assumed.

Table 6-7 shows a summary of parameters constrained in the energy fit.

Parameter	Value
$f_{\mu,prompt} / f_e$	0.965±0.01
$f_\tau / f_{\mu,prompt}$	0.089±0.016
f_{NC}	0.21±0.03

Table 6-7: Constraints used in the EMCal energy spectrum fit.

Additionally, the information about the prompt/nonprompt ratio from the fit to the muon spectrum had to be incorporated. This was accomplished by modifying the χ^2-fit in a way that took into account the value for prompt/nonprompt ratio calculated in Section 6.2. The modified expression for χ^2 is:

$$\chi^2_{total} = \chi^2_{fit} + \frac{1}{\sigma^2_\mu}\left(r_{p,e} - r_{p,\mu}\right)^2 \tag{6.18}$$

In this equation $r_{p,x}$ indicates the prompt over total muon ratio for the EMCal (e) and the muon momentum (μ) fit, and σ_μ is the error on the ratio from the muon momentum fit.
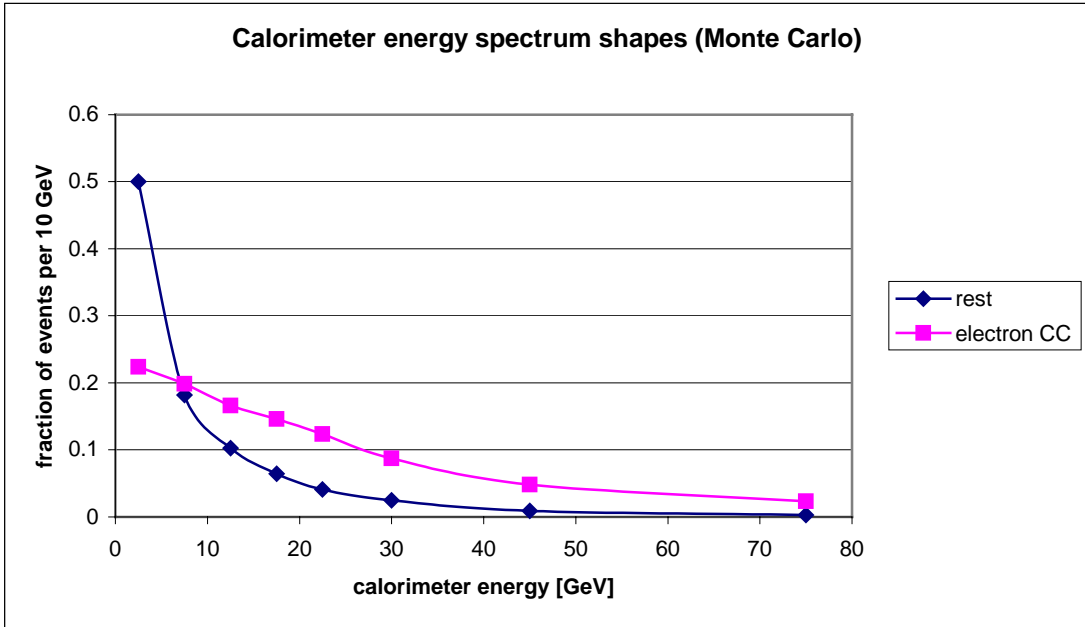
Figure 6-6: Expected distributions of calorimeter energy for electron charged-current events and others (NC, tau CC, muon CC). Both distributions are normalized to unit area
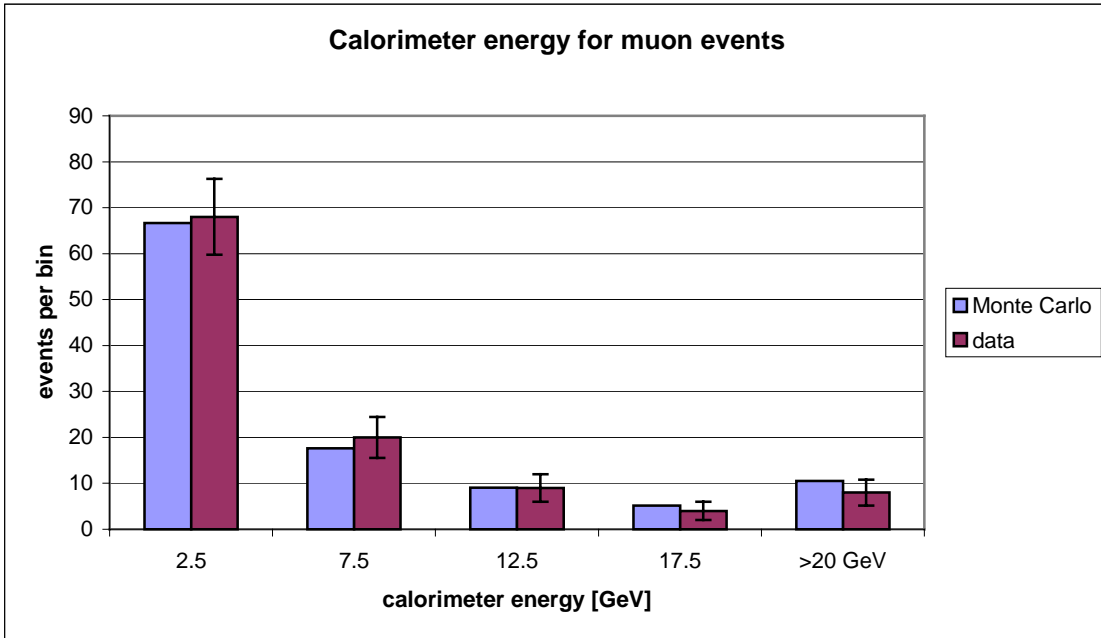
Figure 6-7: Visible energy in the calorimeter for identified muon events compared to Monte Carlo simulation.

6.3.2 Result

The result of the fit is shown in Figure 6-8. For the quality of the fit one gets a value of $\chi^2 / dof = 11.2 / 8$.

Table 6-8 shows the final result for the composition of the event sample as determined in the fit to the electromagnetic calorimeter energy spectrum. Note that the errors on the individual values are correlated. The sum of all fractions must always equal 100% and individual values are constrained as shown in Table 6-7.

Event type	Fraction of total	Comment
Prompt muon CC	28%±3% (*stat.*) ±1%(*sys.*)	Free parameter
Nonprompt muon CC	19%±6% (*stat.*) ±1%(*sys.*)	Given by $1 - \quad f_i$
Electron CC	29%±3% (*stat.*) ±1%(*sys.*)	See Table 6-7
Tau neutrino CC[1]	2.5%±0.3% (*stat.*) ±0.5%(*sys.*)	See Table 6-7
Neutral current	21%±3%(*sys.*)	Fixed value

Table 6-8: Composition of event sample according to electromagnetic calorimeter fit. Systematic errors result from uncertainties on constraints in Table 6-7 and systematic error in Table 6-6.

The fraction of charged-current events from charm in the total observed sample is:

$$f_{charmCC} \equiv \frac{N_{charmCC}}{N_{obs}} = 1 - f_{NC} - f_{\mu CC,nonpr} \qquad (6.19)$$

and, inserting numerical values from Table 6-8:

$$f_{charmCC} = 1 - 0.21 \pm 0.03(sys.) - 0.19 \pm 0.06(stat.) \pm 0.01(sys.) = 0.60 \pm 0.06(stat.) \pm 0.03(sys.)$$
(6.20)

One can compare this value from the energy spectrum fit for the fraction of prompt to all muons to the value from Table 6-3 and to the theoretical expectation. The general expression is:

$$\frac{N_{\mu CC,prompt}}{N_{all\mu}} = \frac{f_{\mu CC,prompt}}{f_{\mu CC,nonpr} + f_{\mu CC,prompt}} \qquad (6.20)$$

---

[1] Assuming standard cross section, the value shown here is calculated only for the purpose of generating the simulated energy spectrum

In order to take correlations and asymmetric shape of errors into account, the errors were calculated numerically. Increasing χ^2_{total} of equation 6.18 by one yields the result:

$$\frac{N_{\mu CC,prompt}}{N_{all\mu}} = 60\%\,^{+11\%}_{-10\%}(stat.) \pm 2\%(sys) \tag{6.21}$$

A theoretical expectation value can be calculated from Table 6-1 and Table 6-2 by

$$N_{ev,(non)prompt,th} \propto \sum_i f_i \cdot \overline{E}_{vi} \cdot \overline{\varepsilon}_i \cdot \frac{N_{vi}}{pot} \tag{6.22}$$

where the sum is over all individual contributions. The result is:

$$\frac{N_{ev,prompt,th}}{N_{ev,all\mu,th}} = 64.5\% \pm 9.6\% \tag{6.23}$$

All three results are summarized in Table 6-9. The two results from actual data are consistent within one sigma. The same is true for the results from the combined fit and from the first-principles calculation.

Method	Value	Source
Fit to muon momentum spectrum	$0.42\pm0.19(stat.)\pm0.09(sys.)$	Table 6-6
Momentum Spectrum + EMCal	$0.60^{+0.11}_{-0.10}(stat.)\pm0.02(sys.)$	Equation 6.23 (numerical calculation)
First-principles calculation	0.645 ± 0.096	Table 6-1, Table 6-2

Table 6-9: Summary of results for prompt fraction in muon charged current events.
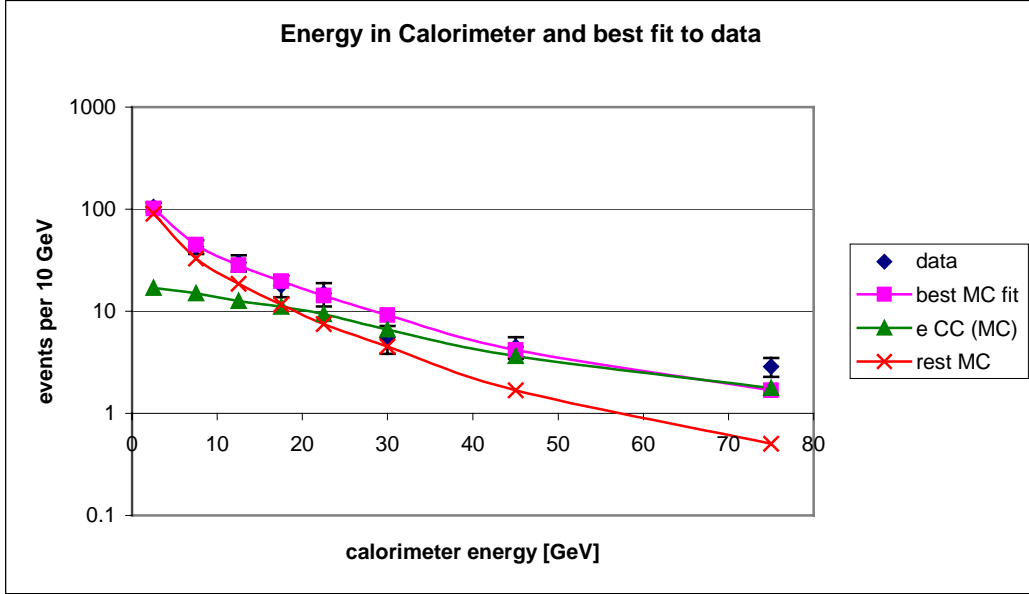
Figure 6-8: Best fit to electromagnetic calorimeter data.

6.4 Tau Neutrino Charged-current Interaction Cross Section

There are two separate methods to check whether the tau neutrino charged-current yield agrees with theory. If that is the case, tau neutrinos are consistent with being "standard particles", all of whose properties can be described in the framework of the Standard Model.

First, assuming equation 6.5 to be true, equation 6.3 can be rewritten as:

$$N_{ev,th}(\nu_\tau CC) = \left[\frac{1}{N_{ev,obs}(\nu_x CC)} \cdot \frac{\overline{\varepsilon}_{\nu_x CC}}{\overline{\varepsilon}_{\nu_\tau CC}} \cdot \frac{N_{\nu_x, on\_tgt}}{N_{\nu_\tau, on\_tgt}} \cdot \frac{n_{\nu_x}(E) \cdot EdE}{n_{\nu_\tau}(E) \cdot K_F(E) \cdot EdE} \right]^{-1} \quad (6.24)$$

where $N_{ev,th}(\nu_\tau CC)$ corresponds to the expected number of tau neutrino events. Adding the number of expected background events N_{bkgrnd} gives an estimate for the total number of events identified as tau interactions. Using Poisson statistics, one can compare theoretical and experimental values and check for consistency.

Second, one can use equation 6.3 to calculate the cross section directly.

The first step in both methods is to establish numerical values for all parameters in equation 6.3.

6.4.1 Calculation of Parameters

The number of observed charged-current events from charm has been calculated in the previous section as a fraction of the total event yield. The absolute value is therefore:

$$N_{ev,obs}(\nu_x CC, charm) = 203 \cdot 0.60 \pm 0.06(stat.) \pm 0.03(sys.) = 122 \pm 12(stat.) \pm 6(sys.)$$
(6.21)

Adding the statistical error caused by the finite number of events, $\sigma_{stat} = \sqrt{122}$, gives the final result:

$$\boxed{N_{ev,obs}(\nu_x CC, charm) = 122 \pm 16(stat.) \pm 6(sys.)}$$
(6.25)

Calculation of relative efficiencies and target acceptances is straightforward using Monte Carlo data.

It should be noted that the emulsion location efficiency for tau neutrino charged-current events contains an additional factor $f_{top} = 0.60 \pm 0.03$. Its origin is the dependence of tau CC identification efficiency on the event topology - length of the tau track and angle with respect to the charged daughter particle[101]. Another factor going into the efficiency is the fraction of tau leptons decaying with a single charged daughter, $f_{sng} = 0.86$. The overall value is therefore modified with respect to the selection and location efficiency $\bar{\varepsilon}_{\tau CC,sel;loc}$ from Table 5-8 as:

$$\bar{\varepsilon}_{\tau CC} = \bar{\varepsilon}_{\tau CC,sel;loc} \cdot f_{sng} \cdot f_{top}$$
(6.26)

Table 6-10 summarizes all relevant quantities. In the last row the product of all values is shown, corresponding to the number of located and identified tau charged-current events as a fraction of all neutrino charged-current events from charm assuming that the theory is correct.

Identifying $N_{\nu,on\_tgt} = N_{\nu,prod} \cdot \bar{\eta}_\nu$, equation 6.3 can be written as:

$$\sigma_{0\tau CC} = \frac{N_{ev,obs}(\nu_\tau CC)}{122 \pm 12(stat.) \pm 6(sys.)} \cdot (0.022 \pm 0.004(sys.))^{-1} \cdot \sigma_{0xCC}$$
$$= N_{ev,obs}(\nu_\tau CC) \cdot \sigma_{0xCC} \cdot 0.37 \pm 0.04(stat.) \pm 0.07(sys.)$$
(6.27)

Parameter	Source	Value
$N_{\nu_\tau,prod} / N_{prompt,prod}$	Table 5-2, Table 5-5	5.9±1.1%
$\overline{\eta}_\tau / \overline{\eta}_{prompt}$	Monte Carlo	1.01±0.02%
$\dfrac{n_{\nu_\tau}(E) \cdot K_F(E) \cdot EdE}{n_{\nu_x} \cdot (E) \cdot EdE}$	Monte Carlo	0.69±0.02
$\overline{\varepsilon}_{\tau CC} / \overline{\varepsilon}_{prompt}$	Table 5-7, Table 5-8, equation 6.26	0.52±0.03
Product:		2.2±0.4%

Table 6-10: Summary of parameters in equation 6.3.

6.4.2 Consistency with Theory

Using the result from the previous section and equation 6.24, one can calculate the expected number of observed tau neutrino events:

$$N_{ev,th}(\nu_\tau CC) = 2.7 \pm 0.3(stat.) \pm 0.5(sys.) \tag{6.28}$$

Adding the expected number of background events, $N_{bkgrnd} = 0.34 \pm 0.05$ [70], the expected signal is:

$$\boxed{N_{sig,th} = 3.0 \pm 0.3(stat.) \pm 0.5(sys.)} \tag{6.29}$$

In order to compare theory and observation, the probability of observing $N_{sig,obs}$ events or more has to be calculated. Using Poisson statistics, one gets:

$$P(n \geq N_{sig,obs} \mid N_{sig,th}) = \sum_{N_{sig,obs}}^{\infty} e^{-N_{sig,th}} \frac{N_{sig,th}^n}{n!} \tag{6.30}$$

The error on the theoretical value, assuming it is Gaussian, can be taken into account by changing equation 6.30 to:

$$P_{err}(n \geq N_{sig,obs} \mid N_{sig,th}) = \int_0^{\infty} \left[\frac{1}{\sqrt{2\pi}\sigma} e^{-\frac{1}{2}\frac{(x-N_{sig,th})}{\sigma^2}} \sum_{N_{sig,obs}}^{\infty} e^{-x} \frac{x^n}{n!} \right] dx \tag{6.31}$$

where σ is the error on $N_{sig,th}$. Adding systematic and statistical errors in quadrature, the probability can be calculated numerically. For $N_{sig,obs} = 4$ the result is:

$$P_{err}(n \geq 4 \mid 3.0 \pm 0.6) = 0.36 \tag{6.32}$$

One standard deviation corresponds to a probability of $\approx 16\%$, therefore theory and measurement are in agreement.

6.4.3 Calculation of Cross Section

To calculate the tau neutrino charged-current cross section directly, one has to know the proper expression for $N_{ev,obs}(\nu_\tau CC)$. While the mean value can simply be assumed as

$$N_{ev,obs}(\nu_\tau CC)_{mean} = N_{sig,obs} - N_{bkgrnd} = 3.7 \tag{6.33}$$

calculation of the spread is more involved.

Using Poisson statistics, the probability to observe $N_{sig,obs}$ events with an expected background of N_{bkgrnd} is

$$P(N_{sig,obs}) = e^{-(N_{sig,true} + N_{bkgrnd})} \frac{(N_{sig,true} + N_{bkgrnd})^{N_{sig,obs}}}{(N_{sig,obs})!} \tag{6.34}$$

where $N_{sig,true}$ is expected number of true signal events.

Under the *a priori* assumption that all values for $N_{sig,true}$ are equally likely, one can calculate the probability distribution for given $N_{sig,obs}$ and N_{bkgrnd} as:

$$P(N_{sig,true} + N_{bkgrnd} < \mu') = \frac{\int_{0.34 \pm 0.05}^{\mu'} \frac{\mu^{N_{sig,obs}}}{N_{sig,obs}!} e^{-\mu} d\mu}{\int_{0.34 \pm 0.05}^{\infty} \frac{\mu^{N_{sig,obs}}}{N_{sig,obs}!} e^{-\mu} d\mu} \tag{6.35}$$

with

$$\mu \equiv N_{sig,true} + N_{bkgrnd} \tag{6.36}$$

The result for the denominator is:

$$\int_{0.34 \pm 0.05}^{\infty} \frac{\mu^4}{4!} e^{-\mu} d\mu \cong 1 \tag{6.37}$$

and therefore

$$P(N_{sig,true} + N_{bkgrnd} < \mu') = \int_{0.34\pm0.05}^{\mu'} \frac{\mu^4}{4!} e^{-\mu} d\mu = 1 - e^{-\mu'} \left(\frac{\mu'^4}{24} + \frac{\mu'^3}{6} + \frac{\mu'^2}{2} + \mu' + 1 \right) \Bigg|_{\mu'}^{0.34\pm0.05}$$

(6.38)

A plot of the function in equation 6.38 is shown in Figure 6-9.

Probablility distribution for true signal

(y-axis: integrated probability, x-axis: true signal)
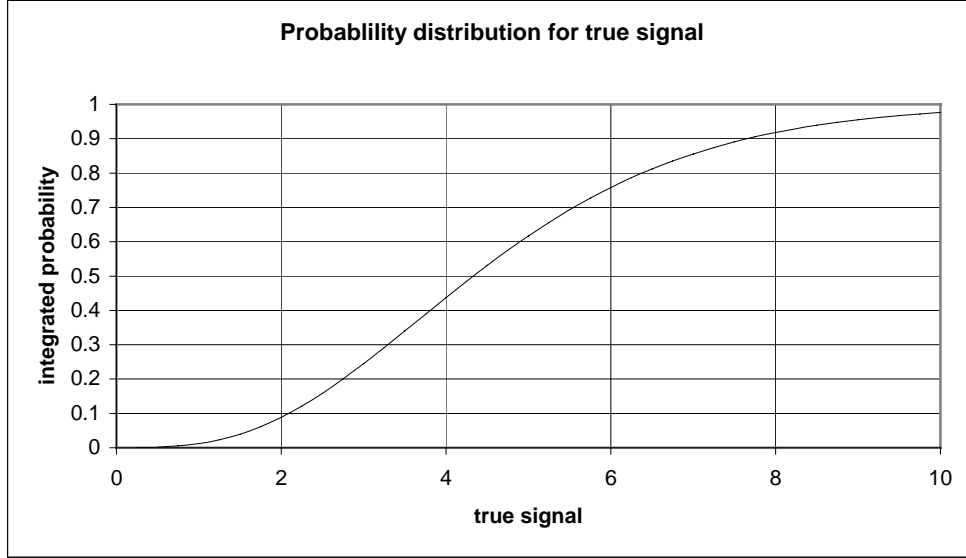
Figure 6-9: Integrated probability distribution assuming n(bkgrnd) = 0.34 +/- 0.05 and n(obs) = 4.

Knowing the probability distribution for $N_{sig,true}$, the calculation of its mean value and error bars is straightforward using numerical means. The respective conditions are: $P_{mean} = 0.5$, $P_{1\sigma} = 0.16, 0.84$ and $P_{90\%} = 0.05, 0.95$.

For the final result one gets:

$$N_{\nu_\tau CC,obs} = 3.7^{+3.1(+5.1)}_{-1.2(-2.1)}$$

(6.39)

with error bars corresponding to 1σ (90% C.L.).

Inserting equation 6.39 into equation 6.27, the cross section can be calculated:

$$\sigma_{0\tau CC} = \sigma_{0xCC} \cdot 3.7^{+3.1(+5.1)}_{-1.2(-2.1)}(stat.) \cdot 0.37 \pm 0.04(stat.) \pm 0.07(sys.)$$
$$= \sigma_{0xCC} \cdot 1.4^{+1.2(+1.9)}_{-0.5(-0.8)}(stat.) \pm 0.3(sys.)$$

(6.40)

With $\sigma_{0xCC} = 5.0 \times 10^{-43} \ m^2 GeV^{-1} = 5.0 \ fbarnGeV^{-1}$ [36] the absolute value is:

$$\boxed{\sigma_{0\tau CC} = 7.0^{+6.0}_{-2.5}(stat.) \pm 1.5(sys.) \ fbarnGeV^{-1}}$$

(6.41)

and for 90% C.L.:

$$\sigma_{0\tau CC} = 7.0^{+8.5}_{-4.0}(stat.) \pm 3.0(sys.) \ fbarnGeV^{-1}(90\% C.L.)$$

(6.42)

7 Conclusion

For the first time the tau neutrino charged-current cross section has been calculated using directly-observed interactions. Its value was found to be in agreement with the Standard Model prediction.

In this analysis, neutrino events of all types were used to determine the fraction of charged-current events in the sample that originated from charm decays in the beam dump. Two event samples with independent data sources were used to obtain the final result.

The first sample consisted of electronically reconstructed events containing an unambiguously identified muon track. The momentum spectrum of those tracks was used in a one-parameter fit in order to obtain the fraction of muon charged-current events from charm decays. The result corresponded to a fraction of muon charged-current events from charm in the overall event sample of $0.42 \pm 0.19(stat.) \pm 0.09(sys.)$. The shape of the data spectrum was in good agreement with the simulated distribution, indicating little or no background.

The second event sample contained only of events with a located emulsion vertex. In this case the spectrum of the energy deposited in the electromagnetic calorimeter was fitted to the simulated distribution. Here results from previous experiments for charged and neutral current neutrino interactions were used to impose constraints on the fitting parameters. The result of this part of the analysis led in combination with the previous part to a more refined value for the fraction of muon charged-current events not coming from charm decays of

$$\frac{N_{\mu CC,nonpr}}{N_{allCC}} = 0.18 \pm 0.06(stat.) \pm 0.01(sys.).$$

From this result, the number of neutrino charged-current events from charm was calculated as $N_{ev,obs}(\nu CC, charm) = 122 \pm 16(stat.) \pm 6(sys.)$. This number was used to normalize the number of tau neutrino charged-current interactions.

After correcting for efficiencies and background, the ratio of the experimental to the theoretical value for the tau neutrino charged-current interaction cross section was

determined to be $\dfrac{\sigma_{\nu_\tau CC}(\exp.)}{\sigma_{\nu_\tau CC}(th.)} = 1.4^{+1.2(+1.9)}_{-0.5(-0.8)}(stat.) \pm 0.3(0.6)(sys.)$ for one sigma

(90%C.L.).

Expressing the cross section as constant factor in the general form $\sigma_{\nu_\tau CC}(E) = \sigma_{0\tau CC} \cdot E \cdot K_F(E)$ leads to the numerical value:

$$\sigma_{0\tau CC} = 7.0^{+6.0(+8.5)}_{-2.5(-4.0)}(stat.) \pm 1.5(3.0)(sys.) \; fbarnGeV^{-1}.$$

The result is in qualitative agreement with the Standard Model, $5.0\,fbarnGeV^{-1}$, confirming the assumption that tau neutrinos are standard particles. While with the currently available sample an imposition of constraints on new physics is difficult, further analysis of the data collected in the DONUT experiment might well improve statistics to a point where more stringent limits can be put on the relevant parameters.

Bibliography

[1] See, e.g., D. Griffiths, *Introduction to elementary particles* (New York, 1987).

[2] F. Reines and C. Cowan Phys Rev. 92, 830 (1953).

[3] G. Danby et al. Phys. Rev. Lett. 9, 36 (1962).

[4] C. Gerthsen, H. Vogel, *Physik* (Berlin, 1993).

[5] G.J. Feldman and M.L. Perl Phys. Rep. 19, 233 (1975).

[6] M.L. Perl, Ann. Rev. Nuc. Part. Sci. 30, 299 (1980).

[7] E531 collaboration (presented by T. Kondo), Fermilab-Conf-80/92-EXP 7550.531.

[8] A. Gauthier, PhD Thesis, Ohio State University (1987).

[9] E872 collaboration, Fermilab press release, July 21, 2000.

[10] W. Pauli, Zeitschrift fuer Physik 41, 81 (1927).

[11] S. Weinberg, *The Quantum Theory Of Fields* (Cambridge, 1995).

[12] P.A.M. Dirac, Proc. Roy. Soc. 133, 60 (1931).

[13] C.D. Anderson, Science 76, 238 (1932).

[14] D.H. Perkins, *Introduction to High Energy Physics* (London, 1982).

[15] M. Gell-Mann, Phys. Lett. 8, 214 (1964).

[16] CERN report No. 8182/TH 401.

[17] M.E. Peskin, D.V. Schroeder, *An Introduction to Quantum Field Theory* (Reading, 1996).

[18] W. Heisenberg and W. Pauli, Zeitschrift fuer Physik 56, 1 (1929); ibid., 59,168 (1930).

[19] S. Tomonaga, Phys. Rev. 74, 224 (1948).

[20] J. Schwinger, Phys. Rev. 73, 416 (1948).

[21] R. P. Feynman, Rev. Mod. Phys. 20, 367 (1948).

[22] C.N. Yang and R. Mills, Phys. Rev. 96, 191 (1954).

[23] S. Weinberg, Phys. Rev. Lett. 19, 1264 (1967).

[24] A. Salam, in *Elementary Particle Physics*, ed. N. Svartholm (Stockholm, 1968): p.367.

[25] W. Greiner B. Mueller, *Gauge Theory of Weak Interactions* (Berlin, 1996).

[26] T.D. Lee, C.N. Yang: Phys. Rev. 104, 254 (1956).

[27] C.S. Wu, E. Ambler, R.W. Hayward, D.D. Hoppes, R.P. Hudson: Phys. Rev. 105, 1413 (1957).

[28] M. Goldhaber, L. Grodzins, A.W. Sunyar: Phys. Rev. 109, 1015 (1958).

[29] G. 't Hooft, Nucl. Phys. B35, 167 (1971).

[30] G. Arnison et al. Phys. Lett. 122B, 103 (1983).

[31] M. Czakon and M. Zralek Acta Phys.Polon B30, 3121 (1999).

[32] M. Hirsch, H.V. Klapdor-Kleingrothaus, S.G. Kovalenko, Phys. Lett. B298, 311 (1997).

[33] H.V. Klapdor-Kleingrothaus et al., e-Print archive hep-ph/0103062.

[34] V.M. Lobashev et al. Phys. Lett. B460, 227 (1999).

[35] Ch. Weinheimer et al. Phys. Lett. B460, 219 (1999).

[36] Particle Data Group, http:/pdg.lbl.gov.

[37] Phys. Rev. D54, 280 (1996).

[38] C. Daum et al. Phys. Rev. D47, 11 (1993).

[39] J.E. Duboscq Nucl.Phys.Proc.Suppl. 98, 48 (2001).

[40] S. Khalil and E. Torrente-Lujan, to appear in Journal of the Egyptian Mathematical Society. e-Print Archive: hep-ph/0012203.

[41] Reinhard Schwienhorst, PhD Thesis, University of Minnesota (2000).

[42] DONUT Collaboration (R. Schwienhorst et al.) Feb 2001. e-Print Archive: hep-ex/0102026.

[43] S. Hannestad Phys.Rev. D57, 2213 (1998).

[44] X.Y. Pham,e-Print archive: hep-ph/9903356.

[45] A. Bandyopadhyay, S. Choubey and S. Goswami,e-Print archive: hep-ph/0101273.

[46] N. Ushida *et al.*, Nucl.Instrum.Meth.A224:50-64,1984.

[47] K. Kodama *et al.*, Phys.Lett.B309:483-491,1993.

[48] CHORUS Collaboration (E. Eskut *et al.*), Nucl.Instrum.Meth.A401:7-44,1997.

[49] COSMOS Collaboration (A. Asratian *et al.*), ITEP-30-98, Aug 1998.

[50] C.Erickson, PhD Thesis, University of Minnesota (2001, in preparation).

[51] B. Lundberg, *E-872 Prompt Neutrino Beam*, http://fn872.fnal.gov/tn/tn-005.ps.

[52] K. Arisaka *et al.*, FERMILAB-FN-580, Jan 1992.

[53] L. Antoniazzi *et al.*, Nucl.Instrum.Meth.A315:92-94,1992.

[54] E872 technical note, http://fn872.fnal.gov/tn/tn-017.ps.

[55] E872 technical note, http://fn872.fnal.gov/tn/tn-016.ps.

[56] E665 Collaboration (M.R. Adams *et al.*), Nucl.Instrum.Meth.A291:533-551,1990.

[57] C. Stewart *et al.*, Phys.Rev.D42:1385-1395,1990.

[58] N. Saoulidou, PhD Thesis, University of Athens (2001, in preparation).

[59] M. Skender, Masters Thesis, Tufts University (1997).

[60] DART Data Acquisition Project, www.dart.fnal.gov and FERMILAB-Conf-94-103 (1994).

[61] E872 2nd run proposal (1997).

[62] J. Trammell, E872 internal communication, 08/10/99.

[63] C. Erickson, PhD Thesis, University of Minnesota (2001, in preparation).

[64] R. Schwienhorst, E872 internal communication, 07/20/99.

[65] M. Nakamura for the DONUT collaboration, Nucl.Phys.Proc.Suppl. 77,259 (1999).

[66] M. Komatsu, private communication.

[67] N. Nonaka, presentation for E872 collaboration meeting, 03/23/01.

[68] V. Paolone, presentation for E872 collaboration meeting, 07/07/00.

[69] H. Jikou and M.Komatsu, *DONUT LS, 2RY and Vee search* (04/19/00), H. Jikou and K. Kodama, *Summary of Long Large Decay Search in E872* (05/24/00).

[70] DONUT Collaboration (K. Kodama et al.) Phys.Lett.B504, 218 (2001).

[71] J. Sielaff, PhD Thesis, University of Minnesota (2001, in preparation).

[72] G. Ingelman, J. Rathsman, A. Edin, *LEPTO – The Lund Monte Carlo for Deep Inelastic Lepton-Nucleon Scattering,* Comp. Phys. Comm. 101, 108 (1997).

[73] Application Software Group, Computing and Networks Division, *GEANT – Detector Description and Simulation Tool*, CERN Geneva (1998).

[74] D.S. Barton et al. Phys. Rev. D27, 2580 (1983).

[75] S. Fredriksson et al., Phys. Rep. 144, 187 (1987).

[76] M. Adamovich et al. Nucl. Phys. B495, 3 (1997).

[77] M.J. Leitch et al. Phys. Rev. Lett. 72, 2542 (1994).

[78] G.A. Alves et al. Phys. Rev. Lett. 70, 722 (1993).

[79] M. Adamovich et al. Phys. Lett. B284, 453 (1992).

[80] Tim Bolton, e-print archive hep-ex/9708014.

[81] G.A. Alves et al. Phys. Rev. D56, 6003 (1996).

[82] K. Kodama et al. Phys. Lett. B263, 573 (1991).

[83] R. Ammar et al. Phys.Lett.B183, 110 (1987), Erratum-ibid.B192, 478 (1987).

[84] Fernanda G. Garcia et al., e-print archive hep-ex/9905003.

[85] M. Adamovich et al. Phys. Lett. B305, 402 (1993).

[86] G.A. Alves et al. Phys. Rev. Lett. 72, 812 (1994).

[87] E.M. Aitala et al. Phys.Lett.B37, 157 (1996).

[88] E.M. Aitala et al. Phys.Lett.B411, 230 (1997).

[89] R. Bonchiani, S. Catani, M.L. Mangano, P. Nason Nucl. Phys. B529, 424 (1998).

[90] S. Frixione et al., to be published in Heavy Flavours II, ed. by A.J. Buras and M. Lindner, World Scientific, e-Print Archive: hep-ph/9702287.

[91] M. Chada et al. Phys. Rev. D58, 1 (1998).

[92] S. Aoki et al. Prog. Theor. Phys. 89, 131 (1993).

[93] J.Z. Bai et al. Phys. Rev. Lett. 74, 4599 (1995).

[94] K. Kodama et al. Phys. Lett. B382, 299 (1996).

[95] M. Acciarri et al. Phys. Lett. B396, 327 (1997).

[96] F. Parodi et al. in HEP'97 Conference Jerusalem, 1997, paper 455.

[97] J.D. Richman and P.R. Burchat, Rev.Mod.Phys. 67, 893 (1995).

[98] C. Albright and C. Jarlskog Nucl. Phys. B40, 85 (1995).

[99] C. Arroyo et al. Phys.Rev.Lett. 72,3452 (1994).

[100] L. Lyons, *Statistics for nuclear and particle physicists*, Cambridge (1986).

[101] K. Okada, PhD Thesis, University of Nagoya (2001).

Appendices

A Momentum measurement and errors
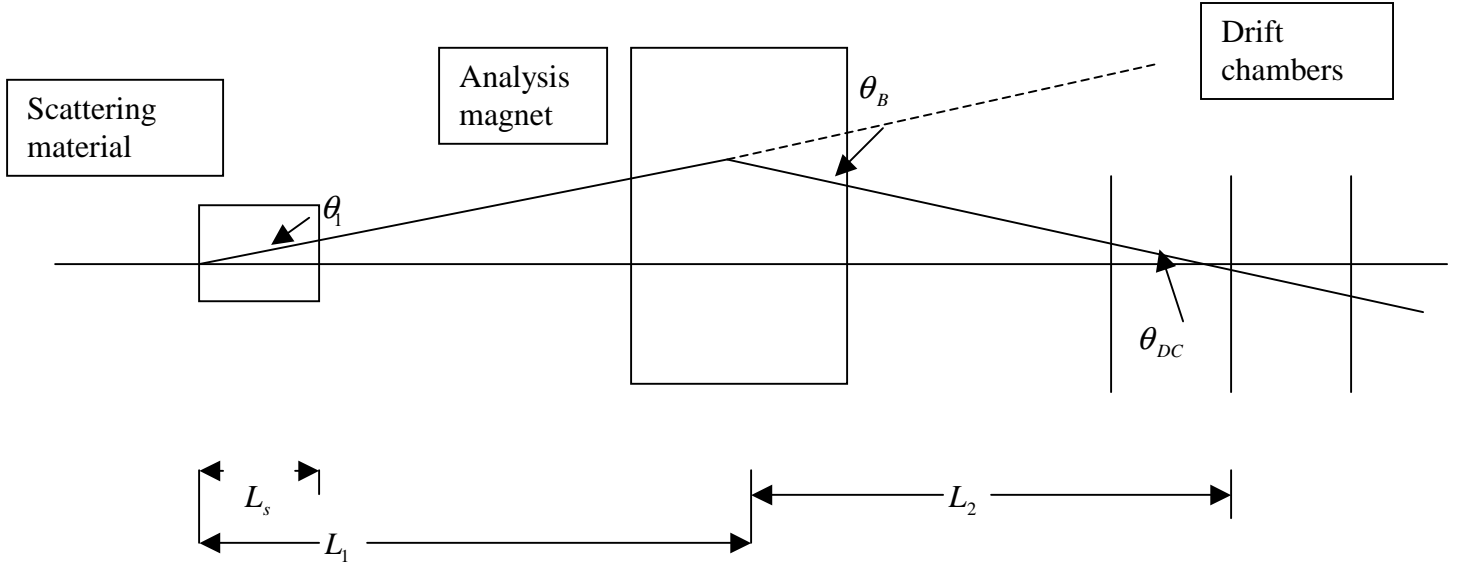
Figure A-1: The apparatus and the relevant quantities for the bend angle error

A.1 Motivation

As mentioned in Section 3, the quality of data from the upstream drift chambers and scintillating fiber planes was degraded by electromagnetic showers in the massive target. For this reason track momenta were calculated using only upstream drift chamber hits and vertex positions. Drift chamber tracks consistent with muon ID hits were extrapolated to the center of the analysis magnet, allowing reconstruction of bend angles using a thin lens approximation for the magnetic field. In this approach, momentum and bend angle are related by:

$$p = \frac{0.225\ GeVc^{-1}mrad^{-1}}{\theta_B} \tag{A.1}$$

and therefore

$$\frac{\delta p}{p} = \frac{\delta \theta_B}{\theta_B} \qquad\qquad\qquad\qquad (A.2)$$

As the equation A.2 shows, track momentum errors are directly related to bend angle errors. The two principal contributions to the latter are multiple scattering in the emulsion modules and the limited resolution of the downstream drift chambers. Figure A-1 shows a sketch of the apparatus with all relevant quantities.

It should be noted that many events had multiple track ambiguities, leading to substantial errors on final track momenta not derivable from first-principle considerations.

A.2 Error Estimate
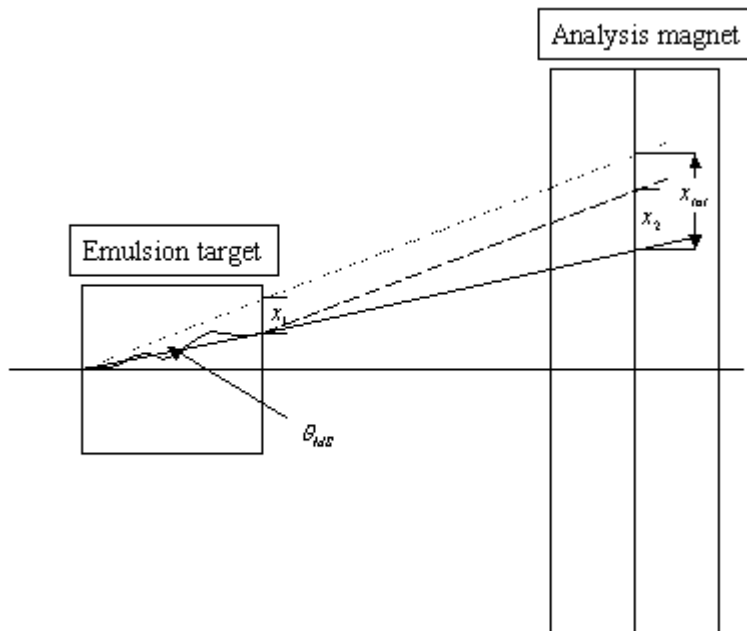
Figure A-2: Components of multiple scattering error. The picture corresponds to the left hand side of Figure A-1 and shows only the emulsion target and analysis magnet.

Figure A-2 shows a sketch of multiple scattering effects on a track. The total bend angle error is given by:

$$\delta_{B,MS} = \frac{x_{total}}{L_1} = \frac{x_1 + x_2}{L_1} \qquad\qquad\qquad (A.3)$$

with the individual components

$$x_1 = \frac{1}{\sqrt{3}} L_s \theta_{MS} \tag{A.4}$$

and

$$x_2 = (L_1 - L_s)\theta_{MS} \tag{A.5}$$

with L_1 and L_s as defined in Figure A-1 and the multiple scattering angle

$$\theta_{MS} = \frac{0.015 \, GeVc^{-1}}{p} \sqrt{\frac{X}{X_0}} \tag{A.6}$$

where X is the thickness and X_0 the radiation length for the scattering material. The measurement error on the upstream part of the track is therefore given by

$$\delta\theta_{B,MS} = (1 - \frac{1}{\sqrt{3}})\frac{L_S}{L_1}\theta_{MS} \tag{A.7}$$

The downstream measurement error is

$$\delta\theta_{B,DC} = \delta\theta_{DC}(1 + \frac{L_2}{L_1}) \tag{A.8}$$

where $\delta\theta_{DC}$ is the angular error resulting from limited drift chamber resolution. An upper limit on this error can be obtained by assuming single hits in one x-plane of the first and third drift chambers. The error on the angle is then determined by the spatial resolution of the drift chambers (350 μm) and their separation (1.6 m).

$$\delta\theta_{DC} \le \frac{350 \, \mu m}{1.6 \, m} \cdot \sqrt{2} = 0.31 \, mrad \tag{A.10}$$

Adding the two contributions in quadrature gives the total error on the bend angle:

$$(\delta\theta_B)^2 = ((1 - \frac{1}{\sqrt{3}})\frac{L_S}{L_1}\theta_{MS})^2 + (\delta\theta_{DC}(1 + \frac{L_2}{L_1}))^2 \tag{A.11}$$

To obtain an upper bound for the error, values as shown in Table A-1 were used.

$\sqrt{\dfrac{X}{X_0}}$	$\approx 3\,^*$
$\delta\theta_2$	0.31 mrad
L_1	3.0 m
L_2	2.6 m
L_s	1.0 m

Table A-1: Values used for estimate of bend angle error.

The error on the bend angle is therefore limited by:

$$\delta\theta_B \le \sqrt{\left((1-\frac{1}{\sqrt{3}})\frac{1.0\,m}{3.0\,m}\cdot 3\cdot\frac{0.015\,GeV}{p}\right)^2 + (0.31\,mrad\cdot 1.87)^2}$$
$$= \sqrt{(\frac{0.006\,GeV}{p})^2 + 0.33\times10^{-6}\;\;rad} \tag{A.12}$$

From equation A.2 then follows:

$$\frac{\delta p}{p} = \frac{\delta\theta_B}{\theta_B} \le \frac{p}{0.225\,GeVc^{-1}}\cdot\sqrt{\left(\frac{0.006\,GeVc^{-1}}{p}\right)^2 + 0.33\times10^{-6}} \tag{A.13}$$

An estimate for the momentum error using information from all electronic systems can be obtained from Figure 3-16. The value for one sigma, corresponding to $\delta p / p = 1$ in that case is $1/p = 4.23\times10^{-3}\,GeV^{-1}$, or $p = 236\,GeV$. One can therefore approximate the relative momentum error using a fit to hits in all spectrometer systems as:

$$\frac{\delta p}{p} = \frac{236\,GeV}{p} \tag{A.14}$$

Figure A-3 shows a plot of momentum errors using both methods. The method used in this analysis is clearly preferable. It should be noted that this estimate is based on calibration events that typically only contain one muon track. It does not take into account errors due to high multiplicity in the scintillating fiber and upstream drift chamber systems as encountered in actual neutrino interactions.

---

* Full thickness, corresponding to a vertex in emulsion station 1.

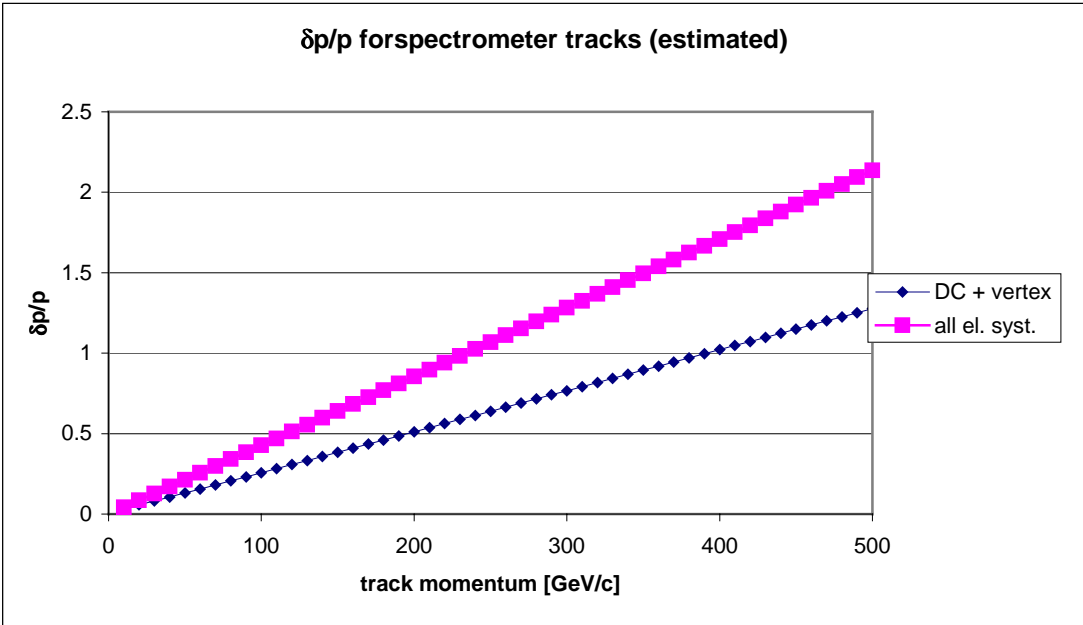**δp/p forspectrometer tracks (estimated)**

Figure A-3: Estimated values for momentum error using vertex position and downstream drift chambers only and using all electronic systems. The functional dependences are shown in equation A.13 and equation A.14

B   Muon Background Estimate

There were several sources of background muon events other than "nonprompt" muons. Those were background muons coincidentally passing through the target area at the same time as the interaction occurs, muon neutrinos from bottom decays in the beam dump, and three possibilities for particles being produced in the interaction itself and subsequently decaying into muons (light mesons, charm and tauons). The following is an estimate for the expected number of background events from these four sources.

B.1   Light Meson Decay (π,K)

Light mesons are produced in large numbers as part of the hadron jet in neutrino charged-current interactions. There is a finite possibility for them to decay in the spectrometer, producing a muon that can mimic a muon charged-current interaction. To obtain an estimate for the number of background events from this source, 20000 Monte Carlo electron neutrino charged-current events were generated. The light mesons produced in these interactions were tracked through the spectrometer and any muons originating in decays were recorded. The muon tracks were then subjected to the same cuts as the data. Table A-2 shows the effect of the cuts and the number of surviving events.

Cut	Fraction of events
Events containing secondary muons	8.95%
Track passing all 3 muon ID walls	1.79%
Muon momentum > 5GeV/c	1.14%
Track projection within 2.5cm of vertex (in y view)	0.20%

Table A-2: Background estimate for muons from light meson decays in spectrometer. Cuts are listed in the order they were applied.

The result suggests that 0.20% of these events contained a muon that was produced in the decay of a light meson and cannot be distinguished from a primary muon using electronic data only. For a total number of 511 events this translates into an expected background of

$$N_{bkgrnd,\pi K} = 2.0 \times 10^{-3} \cdot 511 = 1.0 \qquad\qquad (A.14)$$

B.2   Background Muons

In addition to muons produced in neutrino interactions, there is the possibility of background muons being mistakenly associated with the interaction vertex. The probability for this to occur can be estimated by calculating the probability of a muon passing through the spectrometer while the systems are being read out. Since the reconstruction of a track requires hits in several different systems, the relevant parameter will be the fastest readout time of the various systems. In this case, it is the drift chambers, with a readout time of $\approx 1 \mu sec$ that determines the size of the time window[102].

Assuming a muon flux rate of 500 Hz in the emulsion area during a spill and requiring the track to be within 2.5 cm of the reconstructed vertex in the y direction, the probability to have a misidentified background muon in the event is:

$$P_{\mu,bkgrnd} = \frac{5cm}{70cm} \cdot (1 - (1-10^{-6})^{500}) = 3.6 \times 10^{-5} \qquad\qquad (A.15)$$

Though this estimate is approximate, it is apparent that the background from this source is negligible.

B.3   Muons from Tau Decay in Detector Target

Tau leptons produced in ν_τ CC interactions can decay into final states containing a muon. If the tau neutrino interaction cross section is in fact as high as expected, this represents another type of background that has to be taken into consideration. One can estimate the ratio of muons from this source to muons from prompt neutrino charged-current interactions using a Monte Carlo simulation. The ratio is given by:

$$\frac{N_{\mu,\tau CC,ID}}{N_{\mu,prompt,ID}} = \frac{\varepsilon_{\mu,\tau CC}(E) \cdot n_\tau(E) \cdot \sigma_{\tau CC}(E)dE}{\varepsilon_{\mu,prompt}(E) \cdot n_{\mu,prompt}(E) \cdot \sigma_{\mu CC}(E)dE} \cdot BR(\tau \to \mu X) \qquad (A.16)$$

with the variables being the same as in equation 6.3.

The above equation can be rewritten in terms of variables that can be directly extracted from a simulation:

$$\frac{N_{\mu,\tau CC,ID}}{N_{\mu,prompt,ID}} = \frac{N_{\nu_\tau,prod}}{N_{\nu_{\mu,prompt},prod}} \cdot \frac{\overline{\eta}_\tau}{\overline{\eta}_{\mu,prompt}} \cdot \frac{\overline{\sigma}(\tau CC)}{\overline{\sigma}(\mu_{prompt}CC)} \cdot \frac{\overline{\varepsilon}_{\mu,\tau CC}}{\overline{\varepsilon}_{\mu,prompt}} \cdot BR(\tau \to \mu X) \text{ (A.17)}$$

The factor 2 in the equation reflects the fact the two tau neutrinos are produced for each D_s. A bar over a particular variable indicates an average over the entire energy range of the neutrino beam component in question.

Table A-3 shows the numerical values for each of the ratios and the result.

Parameter	Value
$N_{\nu_\tau,prod} / N_{\nu_{\mu,prompt},prod}$	12.2±2.2%
$\overline{\eta}_\tau / \overline{\eta}_{\mu,prompt}$	1.03±0.02%
$\overline{\sigma}(\tau CC) / \overline{\sigma}(\mu_{prompt}CC)$	0.69±0.02
$\overline{\varepsilon}_{\mu,\tau CC} / \overline{\varepsilon}_{\mu,prompt}$	0.91±0.02
$BR(\tau \to \mu X)$	17.37±0.07%
$N_{\mu,\tau CC,ID} / N_{\mu,prompt,ID}$:	1.35±0.25%

Table A-3: Parameters for the calculation of muon background from tau decay.

The fraction of prompt muon events in the event sample as calculated in Section 6.3.2 is 28±3%. Identification efficiency for prompt muon events is 71% (Table 6-6). The number of muon events from tau decays is therefore:

$$N_{\mu,\tau CC} = f_{\mu CC,prompt} \cdot \varepsilon_{ID,prompt} \cdot N_{ev} \cdot \frac{N_{\mu,\tau CC}}{N_{\mu,prompt}} =$$

$$(0.28 \pm 0.03) \cdot 0.71 \cdot 511 \cdot (0.0135 \pm 0.0025) = 1.4 \pm 0.3$$

(A.18)

B.4   Muons from Charm Decay in Detector Target

Neutrino interactions with matter also produce charm particles, which can in turn decay into muons. The number of identifiable muons from this source as fraction of the total charged-current interaction event yield is

$$\frac{N_{\mu,charm,ID}}{N_{ev}} = f_{CC} \frac{\overline{\varepsilon}_{\mu,charm,ID}}{\overline{\varepsilon}_{all}} \cdot \overline{BR}(charm \to \mu) \cdot \int \hat{n}_\nu(E) \frac{\sigma_{\nu N \to c\overline{c}X}(E)}{\sigma_{\nu N,total}(E)} dE \quad \text{(A.19)}$$

Here $\hat{n}_\nu(E)$ is the energy spectrum of the incident neutrinos normalized to 1. The integral appearing in this equation has been evaluated using the neutrino energy distribution generated in the Monte Carlo simulation and neutrino charm production

data from NuTeV[103]. Figure A-4 shows the expected number of charm events as function of the neutrino energy.

Values for individual terms and the background calculation result are shown in Table A-4. The number of muon events charmed particles produced in neutrino-nucleon interactions is:

$$N_{\mu,charm,ID} = 511 \cdot (0.0022 \pm 0.0005) = 1.1 \pm 0.3 \tag{A.20}$$

Parameter	Value
f_{CC}	0.79±0.03
$\bar{\varepsilon}_{\mu,charm} / \bar{\varepsilon}_{all,CC}$	30±3%
$\overline{BR}(charm \to \mu)$	11.5±2.0%
$n_\nu(E)\dfrac{\sigma_{\nu N \to c\bar{c}X}(E)}{\sigma_{\nu N,total}(E)}$	8.1±0.8%
$N_{\mu,charm,ID} / N_{ev}$:	0.22±0.05%

Table A-4: Calculation of ratio of identifiable muons from charm decay to total charged-current yield.
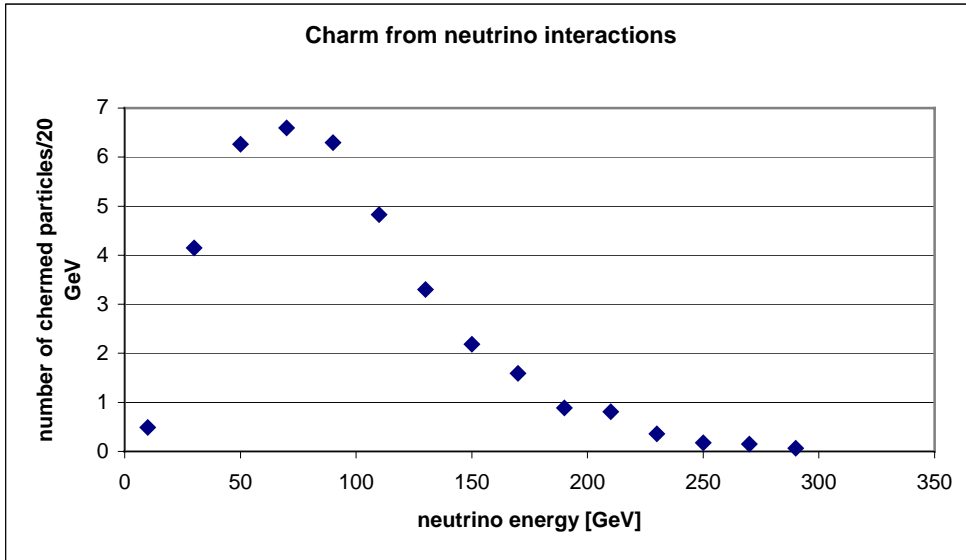
Figure A-4: Expected number of charmed particles from neutrino interactions in 511 event sample as function of the energy of the incident neutrino.

B.5 Bottom Production in Beam Dump

In addition to charmed particles, muon neutrinos can also be produced in bottom decays. The fraction of muons from B decays to muons from charm is:

$$\frac{N_{\mu CC,bottom,ID}}{N_{\mu CC,prompt,ID}} = \frac{\sigma(pN \to b\bar{b})}{\sigma(pN \to c\bar{c})} \cdot \frac{\overline{BR}(bottom \to \nu_\mu X)}{\overline{BR}(charm \to \nu_\mu X)} \cdot \frac{\overline{\eta}_{\nu_\mu bottom}}{\overline{\eta}_{\nu_\mu charm}} \cdot \frac{\overline{\sigma}_{\mu CC,bottom}}{\overline{\sigma}_{\mu CC,charm}} \cdot \frac{\overline{\varepsilon}_{\mu CC,bottom}}{\overline{\varepsilon}_{\mu CC,charm}}$$

(A.13)

Because of large uncertainties in the bottom cross section, the result can only be a rough estimate. Only one experiment, E653, has measured both bottom and charm production in a fixed target setup using the same beam (see Figure 5-2). Their cross section measurements using a 600 GeV pion beam are

$$\sigma_{c\bar{c}} = 24.6 \pm 4.3 \mu barn / nucleon \ ^{104} \tag{A.21}$$

and

$$\sigma_{b\bar{b}} = 33 \pm 11(st.) \pm 5(sys.)nbarn / nucleon \ ^{105} \tag{A.22}$$

The resulting ratio for the cross sections is:

$$\frac{\sigma_{b\bar{b}}}{\sigma_{c\bar{c}}}(\pi N, 600 GeV) = 1.34 \pm 0.54 \times 10^{-3} \tag{A.23}$$

In order to obtain the correspondent value for 800 GeV protons one has to correct for different rates of increase for the two cross sections. Theoretical calculations suggest a correction by a factor of approximately 1.5 in favor of bottom production (Figure 5-3), so the final result is

$$\frac{\sigma_{b\bar{b}}}{\sigma_{c\bar{c}}}(pN, 800 GeV) \cong 2.0 \pm 1.1 \times 10^{-3} \tag{A.24}$$

All other parameters can be calculated in a Monte Carlo simulation. The results are shown in Table A-5

For the number of identified muon events from bottom decays in the beam dump one gets, analogous to equation A.18:

$$N_{\mu,bottom,ID} = 511 \cdot (0.28 \pm 0.03) \cdot 0.71 \cdot (1.6 \pm 1.0) \times 10^{-3} = 0.16 \pm 0.10 \tag{A.25}$$

Parameter	Value
$\sigma_{b\bar{b}} / \sigma_{c\bar{c}}$ production	$2.0 \pm 1.1 \times 10^{-3}$
$BR(bottom \rightarrow \nu_\mu X) / BR(charm \rightarrow \nu_\mu X)$	0.95 ± 0.17
$\overline{\eta}_{bottom} / \overline{\eta}_{charm}$	0.5 ± 0.1
$\overline{\sigma}_{bottom} / \overline{\sigma}_{charm}$	2.2 ± 0.5
$\overline{\varepsilon}_{bottom} / \overline{\varepsilon}_{charm}$	0.75 ± 0.05
$N_{\mu CC,bottom,ID} / N_{\mu CC,prompt}$:	$1.6 \pm 1.0 \times 10^{-3}$

Table A-5: Calculation of fraction of identifiable muon events from bottom decay to prompt muon events

An overview of all background sources for muon events is shown in Table A-6. The overall number of events from background sources discussed in this appendix is 3.7 ± 0.4, or $\approx 3\%$ of all muon events, small enough to be neglected in the analysis

Background source	Number of events
π, K decay	1.0
Background muon	3.6×10^{-5}
Tau decay	1.4 ± 0.3
Charm decay	1.1 ± 0.3
ν_μ from bottom	0.16 ± 0.10
Sum:	3.7 ± 0.4

Table A-6: Summary of background sources for muon charged-current events.

C   Neutrino oscillations

C.1   Introduction

Neutrino oscillations could potentially alter the beam composition and lead to an increase or decrease of the tau neutrino interaction yield. Limits have therefore to be set on the size of any such effect using results from previous experiments. The following is a brief overview of oscillation theory, experimental results and consequences for E872.

C.2   Theory

The basic principle of neutrino oscillation theory is the postulate that there are separate weak flavor and mass eigenstates ν_w and ν_m. A mixing matrix U, analogous to the CKM matrix, connects them as follows:

$$(\nu_w)_i = U_{ij} (\nu_m)_j \tag{A.26}$$

This leads to a time evolution of the weak states:

$$\nu_w(t) = U \cdot \exp(-iHt) \cdot U^\perp \nu_w(0) \tag{A.27}$$

with the Hamiltonian

$$H = diag(...E_i...); E_i^2 = p^2 + m^2 \tag{A.28}$$

In the ultrarelativistic limit $E >> m$ and writing the Hamiltonian in the weak basis

$$H_w^{eff} \equiv \frac{M^2}{2E}, M \equiv U \cdot diag(...m_i^2...) \cdot U^\perp \tag{A.29}$$

the time evolution equation can be written as

$$\nu_w(t) = \exp(-iH_w^{eff} t)\nu_w(0) \tag{A.30}$$

For the oscillation between two neutrino types the matrix U corresponds to a rotation matrix. The probability for oscillation from one state to another can therefore be expressed in terms of the rotation angle θ and the flight length L.

$$P(\nu_1 \rightarrow \nu_2; L) = \sin^2 2\theta \sin^2 \left(\frac{L}{L_{osc}} \right) \tag{A.31}$$

where the oscillation length L_{osc} is defined by:

$$\frac{1}{L_{osc}} \equiv \frac{\Delta m_{12}^2}{4E_v \, c} = 1.27 km^{-1} \frac{\Delta m_{12}^2 [eV^2 c^{-4}]}{E_v [GeV]} \qquad (A.32)$$

with $\Delta m_{12}^2 \equiv (m_{v_1} - m_{v_2})^2$ being the square of the mass difference between two eigenstates.

The number of Standard Model neutrinos with masses lower than $m_Z / 2 \approx 45 GeV$ has been measured from the Z boson decay width as $N_{v,light} = 2.991 \pm 0.016$ [36]. However, this result does not apply to neutrinos that do not participate in the weak interaction, and there are several models that include non-interacting or "sterile" neutrinos. There also are models with a fourth generation neutrino v_s without a charged partner as well as models with 3 generation of weak singlet neutrinos (v_e', v_μ', v_τ') [106].

A limit for the total number of light ($m<<MeV$) neutrinos can be obtained from big bang nucleosynthesis (BBN) models. Most such calculations leave room for at least one additional neutrino generation [107].

An additional effect related to oscillations has been proposed by Mikheev, Smirnov[108] and Wolfenstein[109]. This so-called MSW effect regards matter-induced oscillations. Due to interactions of neutrinos with matter an additional term H_{int} arises in the Hamiltonian. This leads to an effective mixing angle

$$\sin^2 2\theta_m = \frac{\sin^2 2\theta_v}{(\eta - \cos 2\theta_v)^2 + \sin^2 2\theta_v} \qquad (A.33)$$

where θ_v is the mixing angle in vacuum. The parameter η depends on the oscillation length in vacuum, the type of interaction accounting for the effect and the density of the correspondent type of matter. Two cases can be distinguished:

- $v_e \rightarrow v_\mu, v_\tau$. In this case the effect comes from the charged-current interaction. Only electron neutrinos interact with electrons, so the electron density becomes important.

- $v_{e,\mu,\tau} \rightarrow v_s$. Here the difference is that all active neutrinos interact with matter while sterile neutrinos do not. Whether both charged and neutral or only neutral current interactions are relevant depends on the neutrino energy.

C.3 Experimental Results

There is strong evidence for neutrino oscillations from solar and from atmospheric neutrino observations. Experiments searching for solar neutrinos consistently find a deficit of about 50% of the expected value[110]. The best result was obtained by the Super-Kamiokande experiment[111] and corresponds to a ratio between observation and theory of $S_{data}/S_{SSM} = 0.474^{+0.010\ +0.017}_{-0.009\ -0.014}$. The allowed region for solar neutrino oscillation parameters is shown in Figure A-5.
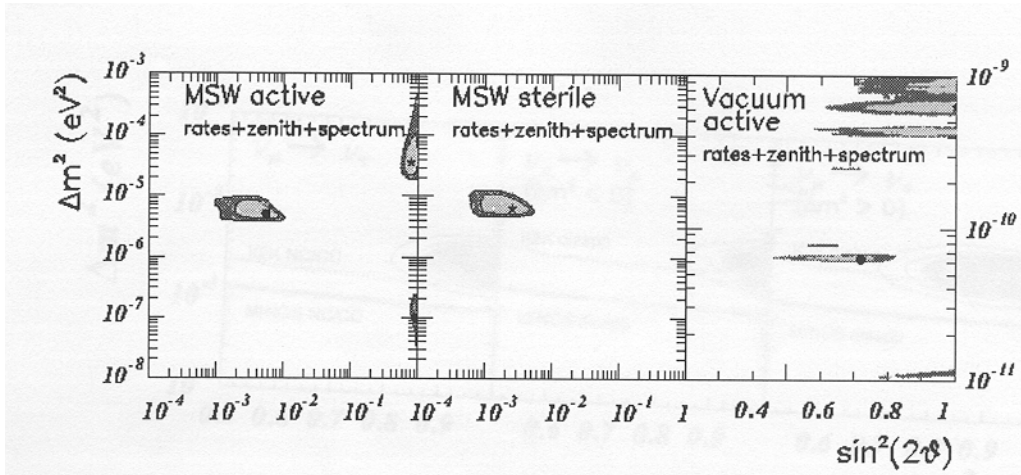
Figure A-5: Allowed solar neutrino parameters from electron neutrino disappearance dependent on model. lighter: 90%CL, darker: 99%CL ([112]).

The same experiment measured the angular and energy dependence of the atmospheric neutrino flux ratio $(v_\mu + \overline{v}_\mu)/(v_e + \overline{v}_e)$. The result is a clear deficit in the number of muon neutrinos whose magnitude depends on the zenith angle[113]. A plot of the allowed parameter region for atmospheric neutrinos is shown in Figure A-6.
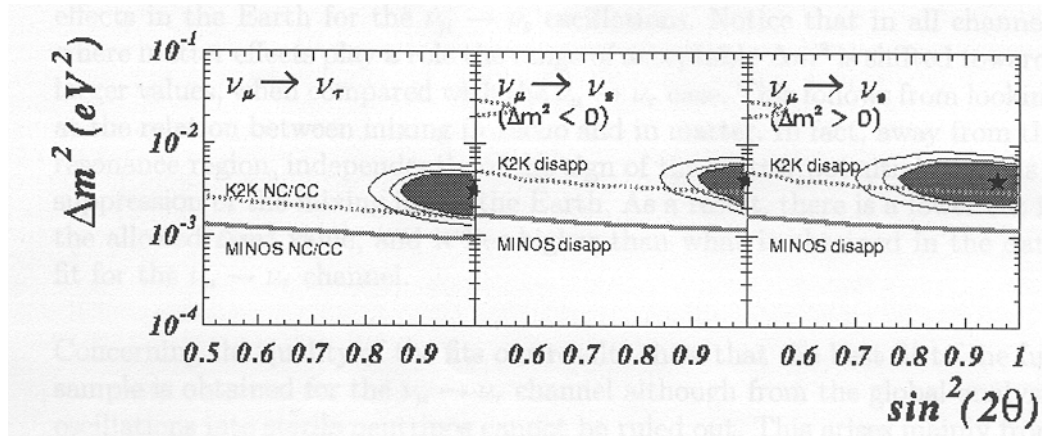
Figure A-6: Allowed atmospheric neutrino parameters from muon neutrino disappearance. solid: 90%CL, lines: 95% and 99% CL ([112]).

Several experiments have searched for evidence of neutrino oscillations using artificial sources. An overview of negative results is given in Table A-7.

Experiment	Channel	$\Delta m^2_{\min}[eV^2]$
CDHSW[114]	$\nu_\mu \to \nu_\mu$ survival	0.25
E776[115]	$\nu_\mu \to \nu_e$	0.075
KARMEN[116]	$\overline{\nu}_\mu \to \overline{\nu}_e$	0.048
E531[117]	$\nu_\mu \to \nu_\tau$	1
CHORUS/NOMAD[118]	$\nu_\mu \to \nu_\tau$	0.9
Bugey[119]	$\nu_e \to \nu_e$ survival	100
CHOOZ[120]	$\nu_e \to \nu_e$ survival	1000

Table A-7: Negative results for neutrino oscillation searches.

The notable exception to these negative searches is the LSND experiment that claims to have found evidence for the transition $\overline{\nu}_e \to \overline{\nu}_\mu$ [121].

Figure A-7, Figure A-8 and Figure A-9 show the excluded area in $\sin^2 2\theta - \Delta m^2$ parameter space for the three possible oscillations between active neutrino mass eigenstates along with the best fit to the LSND data.
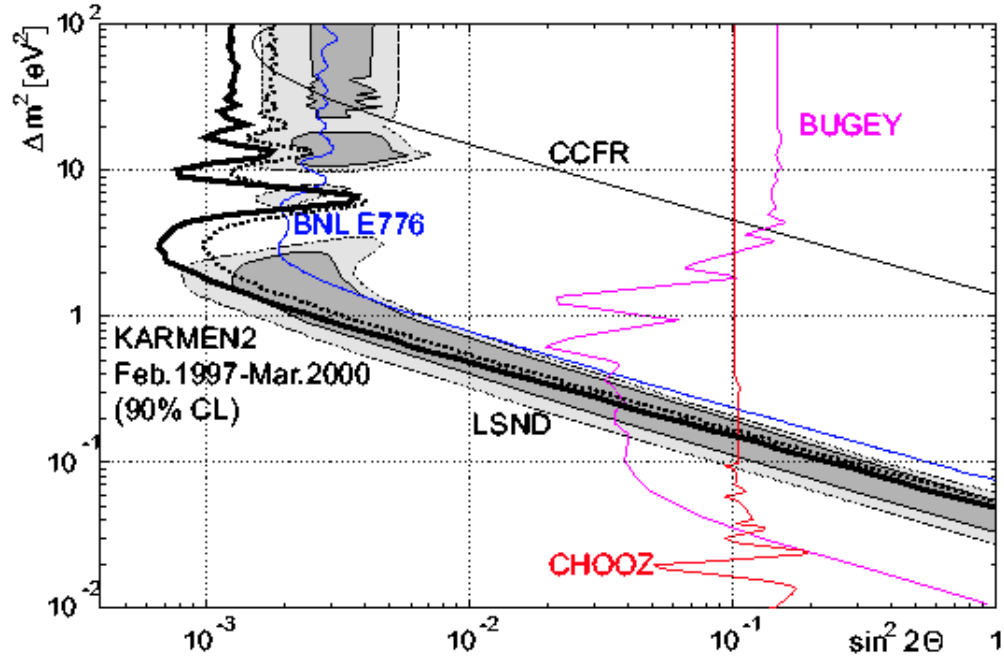
Figure A-7: Excluded region for electron-muon neutrino oscillations ([116]). The shaded region is favored by LSND result (dark: 90% C.L., light: 99% C.L.).
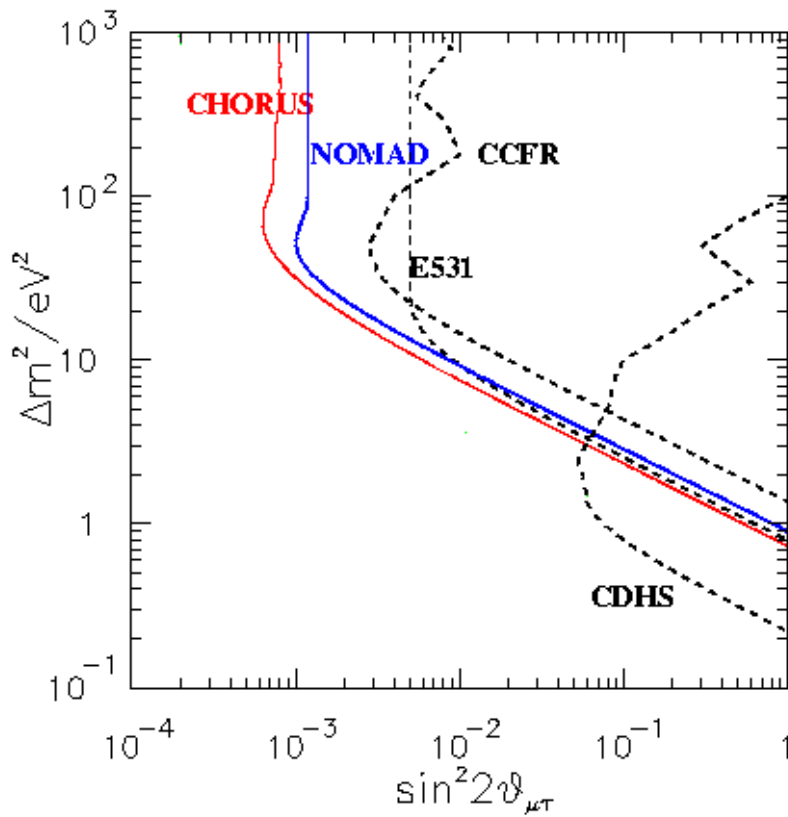

Figure A-8: Excluded region for muon-tau neutrino oscillations ([122]).
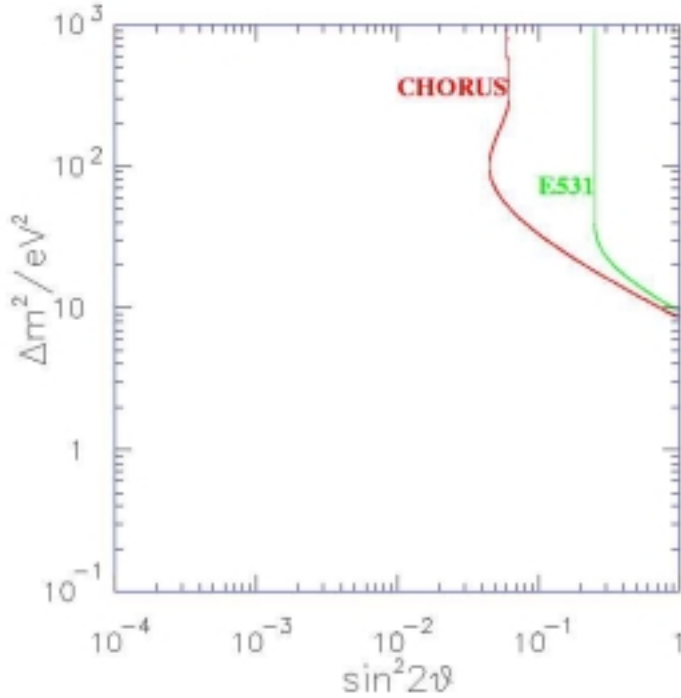
Figure A-9: Excluded region for electron-tau neutrino oscillations ([122]).

In summary, three results indicating the existence of neutrino oscillations have been observed. These are:

- The solar neutrino effect, pointing to a ratio of about 0.5 for expected to observed electron neutrinos. The difference between day and night neutrino flux has been measured as $\frac{2(f_{day} - f_{night})}{(f_{day} + f_{night})} = -0.034 \pm 0.022 \pm 0.013$ [123], being consistent with no MSW-related effects. The oscillation $\nu_e \rightarrow \nu_s$ is therefore disfavored because of the absence of measurable matter-induced effects. There also is some indication for an energy dependence from the Homestake ^{37}Cl experiment[124]. A variety of different models exist for the interpretation of the solar neutrino deficit[125]. All of them lead to a mass difference of $O(10^{-5} eV^2)$ or smaller, with a wide range of possible values for the mixing angle.

- The atmospheric neutrino data, consistent with $\nu_\mu \to \nu_\tau$ oscillations taking into account the amount of neutral current interactions and, again, the absence of clear matter-induced effects[126]. The best fit to the data points to a mass difference $\Delta m^2 \approx 5 \times 10^{-3}\ eV^2$ and close to maximal mixing ($\sin^2 2\theta \approx 1$).

- The LSND experiment, measuring $\nu_e \to \nu_\mu$ oscillations directly and coming up with a mass difference $\Delta m^2 \approx O(1\ eV^2)$ and a mixing angle $\sin^2 2\theta \approx 10^{-3} - 10^{-2}$.

If all three results are correct then there are three clearly distinct mass scales. They can only be reconciled by demanding the existence of at least one sterile neutrino. The preferred model is the "2+2", with two pairs of almost degenerate mass eigenstates separated by the LSND mass difference (see Figure A-10).
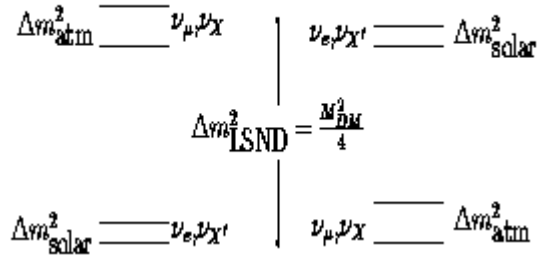

Figure A-10: 2+2 mass models permitted by experimental data.

Here the flavor and mass eigenstates are related by:

$$
\begin{pmatrix} \nu_s \\ \nu_e \\ \nu_\mu \\ \nu_\tau \end{pmatrix} \cong
\begin{pmatrix}
\frac{1}{\sqrt{2}} & \frac{1}{\sqrt{2}} & 0 & 0 \\
-\frac{1}{\sqrt{2}} & \frac{1}{\sqrt{2}} & \varepsilon & \varepsilon \\
\varepsilon & -\varepsilon & \frac{1}{\sqrt{2}} & \frac{1}{\sqrt{2}} \\
0 & 0 & -\frac{1}{\sqrt{2}} & \frac{1}{\sqrt{2}}
\end{pmatrix}
\begin{pmatrix} \nu_0 \\ \nu_1 \\ \nu_2 \\ \nu_3 \end{pmatrix}
\tag{A.26}
$$

where the ε are small[127]. It should be pointed out that recent results from the KARMEN experiment[116] (see Figure A-7) exclude most of the parameter space where

LSND claimed their discovery. If the LSND result is left out the remaining two can be explained by oscillations between three neutrinos only.

Independent of oscillation searches, investigations about the possible mixing between the tau neutrino and a generic heavy neutrino ν_h have been conducted. There are various results from laboratory experiments and astrophysical considerations. The excluded region in the $|U_{\tau h}| - m_{\nu_h}$ (tau-heavy mixing angle – heavy neutrino mass) plane is shown in Figure A-11[128].
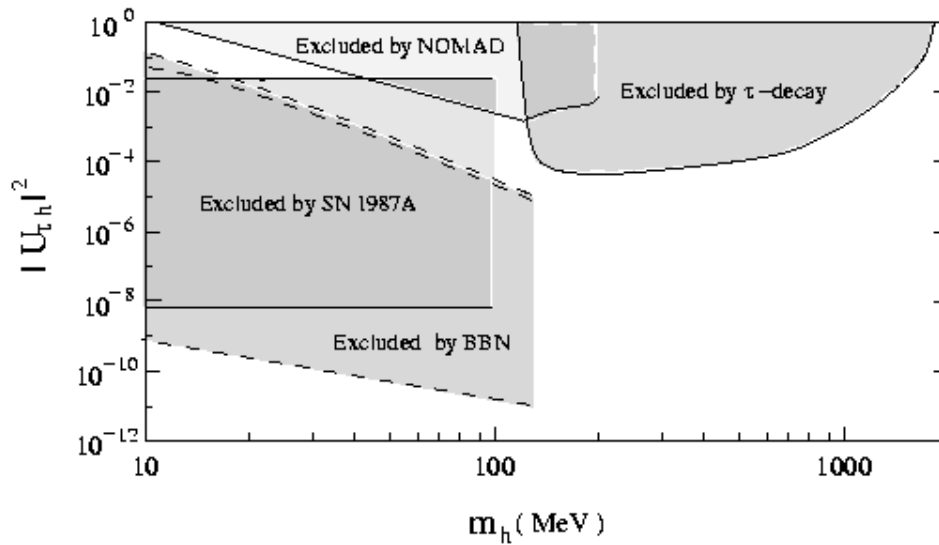

Figure A-11: Excluded region in tau-heavy mixing-matrix element / heavy neutrino mass parameter space (BBN: Big Bang Nucleosynthesis, SN: Supernova).

C.4 Applying existing limits to E872

One can estimate the influence of the processes $\nu_{e,\mu} \to \nu_\tau$ on this experiment by calculating the minimum Δm^2 that causes a measurable effect for a neutrino with given energy. Table A-8 shows the result of the calculation assuming maximal mixing ($\sin^2 2\theta = 1$). A neutrino with energy *5 GeV* has a 1% probability to oscillate into a different flavor in the E872 setup (35 m baseline) if the mass difference is *O(10 eV)*. Neutrinos with higher energies require a higher mass difference to cause the same effect. By looking at Figure A-8 and Figure A-9 one can see that the region in

parameter space that would cause a significant effect is already well excluded by other experiments. Therefore no enhancement of the tau neutrino yield by oscillations from other flavors can be expected. The same is true for transitions between electron and muon neutrinos.

		0.1	0.01	0.001	0.0001	Transition probability
	5	35.6	11.2	3.6	1.1	
	50	355.7	112.5	35.6	11.2	
	100	711.4	225.0	71.1	22.5	
Neutrino Energy [GeV]						

Table A-8: Minimum delta m² [GeV²c⁻⁴] for given transition probability and neutrino energy. Numbers in same row corrspond to same neutrino energy, numbers in same column corrspond to same transition probability.

Other than for oscillations between the three known neutrino flavors, no limits have been set on oscillations from tau to sterile neutrinos. One therefore has to take the possibility into account that there is a significant effect which has so far gone undetected.

Assuming the transition probability from tau to sterile neutrino is of the form

$$P(\nu_\tau \rightarrow \nu_s) = \sin^2\left(\frac{1.27 km^{-1} \delta m^2 L}{E_\nu}\right) \tag{6.32}$$

corresponding to maximum mixing, one can calculate the maximum effect in dependence of the squared mass difference δm^2. Figure A-12 shows a plot of expected tau neutrino yield versus δm^2. It was calculated using the expected tau neutrino energy distribution from the E872 Monte Carlo. The lowest possible value is $\frac{\nu_{\tau,obs}}{\nu_{\tau,prod}} = 0.32$. Figure A-13 shows the Monte Carlo energy distribution for observable tau neutrinos raw and with the strongest possible oscillation effect.

While this should only be considered a qualitative result, it still shows that a significant reduction of tau neutrino flux at the target position caused by oscillations to sterile neutrinos cannot be completely excluded. However, any such reduction would require a mass difference of several ten eV, a region not allowed by current cosmological models (see equation 2.16).
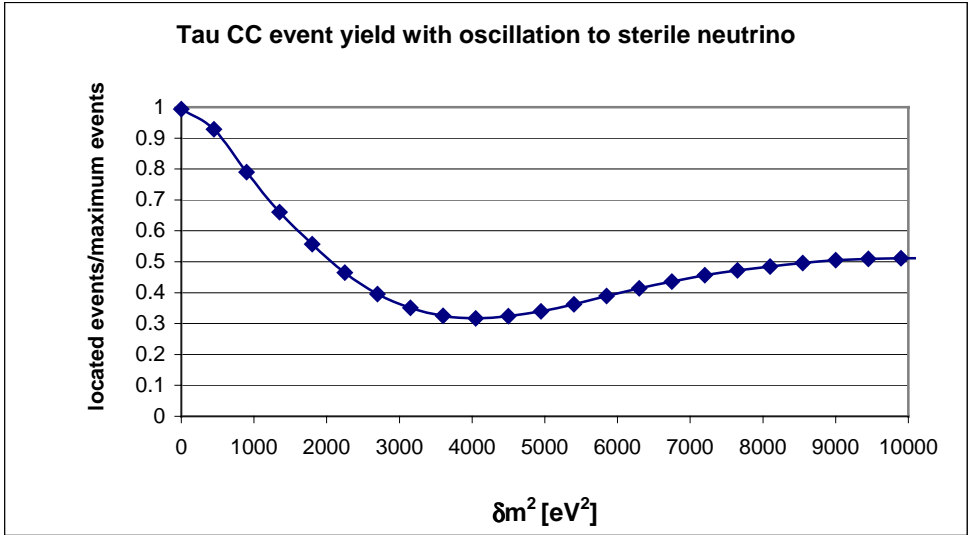
Figure A-12: Expected tau CC event yield in dependence of squared mass difference between tau and sterile neutrino.
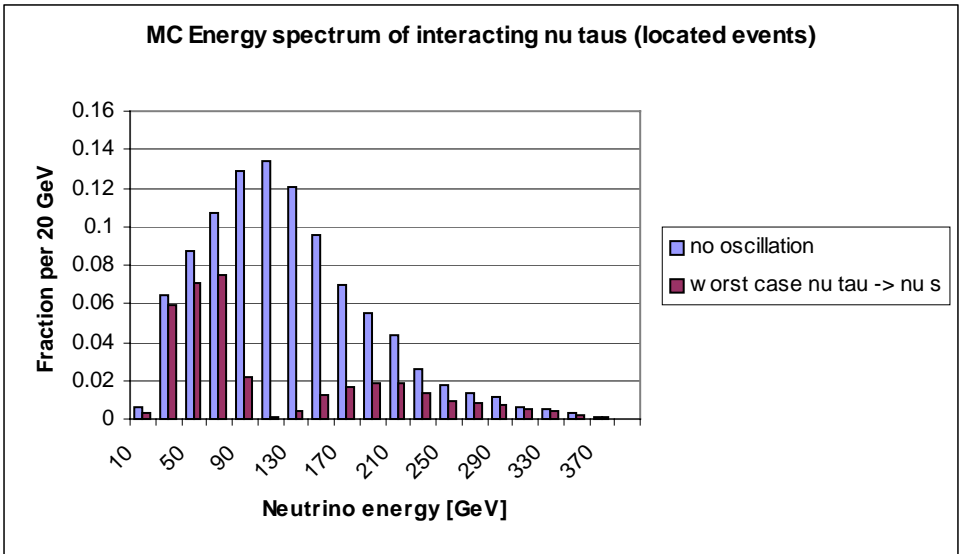

Figure A-13: Simulated energy spectrum of observed tau neutrinos for maximum reduction.

Bibliography (Appendices)

[102] B. Lundberg, *private communication*.

[103] I.I. Bigi et al. pre-print BNL-68106.

[104] Phys.Lett.B284:461-470,1992.

[105] Phys.Lett.B303:359-367,1993.

[106] T.L. Yoon, R.Foot Phys.Lett B491,291 (2000).

[107] C.J. Copi, D.N. Schramm, M.S. Turner Phys.Rev D55,3389 (1997).

[108] S.P. Mikheev, A.Yu. Smirnov Sov.Phys.Usp 30, 759 (1987).

[109] L. Wolfenstein Phys.Rev D17, 2369 (1978).

[110] J.N. Bahcall, P.I. Krastev and A.Y. Smirnov, Phys. Rev. D58, 096016 (1998).

[111] Y. Fukuda et al. Phys.Rev.Lett 82, 2644 (1999).

[112] M.C. Gonzalez-Garcia, C. Pena-Garay, Nucl.Instrum.Meth.A 451,157 (2000).

[113] Y. Fukuda et al. Phys.Lett.B467, 185 (1999).

[114] F. Didak et al. Phys. Lett. B134, 281 (1994).

[115] L. Borodovsky et al. Phys. Rev. Lett. 68, 274 (1992).

[116] K. Eitel for the collaboration, Nucl.Phys.Proc.Suppl 91, 191 (2000).

[117] E531 Collaboration, Phys. Rev. Lett. 57, 2898 (1986).

[118] G. Romano Jul 1999. Published in In *Tampere 1999, High energy physics* 907-909.

[119] B. Achkar et al. Nucl. Phys. B424, 503 (1995).

[120] A. Apollonio et al. Phys. Lett. B420, 397 (1998).

[121] C. Athanassopoulos Phys. Rev. Lett. 81, 1774 (1998).

[122] CHORUS Collaboration. Jul 1999, Contributed to 19th International Symposium on Lepton and Photon Interactions at High-Energies (LP 99), e-Print Archive: hep-ex/9907015.

[123] Y. Suzuki, Super-Kamiokande collaboration, talk at Neutrino 2000.

[124] B.T. Cleveland et al. Astrophys. J496, 505 (1998).

[125] J.N. Bahcall, P.I. Krastev, A.Yu. Smirnov e-Print archive: hep-ph/0103179.

[126] S. Fukuda et al. Phys. Rev. Lett. 85, 3999 (2000).

[127] V. Barger, B. Kayser, J. Learned, T. Weiler and K. Whisnant Phys.Lett. B489,345 (2000).

[128] V. Gribanov, S. Kovalenko, I. Schmidt e-Print Archive: hep-ph/0102155.